This is to certify that the
dissertation entitled

LOCAL STRUCTURE OF Ge_xSe_{1-x} GLASSES AROUND THE RIGIDITY PERCOLATION THRESHOLD USING ATOMIC PAIR DISTRIBUTION FUNCTION AND X-RAY ABSORPTION FINE STRUCTURE TECHNIQUES

presented by

MONEEB TAISEER SHATNAWI

has been accepted towards fulfillment
of the requirements for the

Doctoral degree in Physics

Major Professor's Signature

8/24/07

Date

LOCAL STRUCTURE OF Ge_xSe_{1-x} GLASSES AROUND THE RIGIDITY PERCOLATION THRESHOLD USING ATOMIC PAIR DISTRIBUTION FUNCTION AND X-RAY ABSORPTION FINE STRUCTURE TECHNIQUES

By

MONEEB TAISEER SHATNAWI

A DISSERTATION

Submitted to
Michigan State University
in partial fulfillment of the requirements
for the Degree of

DOCTOR OF PHILOSOPHY

Department of Physics and Astronomy

2007

ABSTRACT

LOCAL STRUCTURE OF Ge_xSe_{1-x} GLASSES AROUND THE RIGIDITY PERCOLATION THRESHOLD USING ATOMIC PAIR DISTRIBUTION FUNCTION AND X-RAY ABSORPTION FINE STRUCTURE TECHNIQUES

By

Moneeb Taiseer Shatnawi

A search for a structural response to a recently proposed self-organized and stress-free intermediate phase [1, 2] in semiconductor chalcogenide Ge_xSe_{1-x} glasses has been performed in this study. These glasses, according to the mean-field approach, undergo a structural phase transition from floppy to rigid network that occurs at a mean coordination number of 2.4. Based on thermodynamic and spectroscopic measurements, these glasses appear to exhibit two transitions instead of one [3]. The region between these transitions has been called the intermediate phase (IP) [3, 4]. The original theoretical work assumed that the network was generic and the connectivity random [5]. It was therefore suggested [1] that the IP phase is a region of finite width in composition where the network could self-organize in such a way that maintains a rigid but unstressed state. However, it has proved difficult to establish this result experimentally.

High-resolution atomic pair distribution functions (PDF), derived from high energy synchrotron radiation, coupled with high-resolution X-ray absorption fine structure (XAFS) measurements on 18 compositions of well-prepared Ge_xSe_{1-x} glasses that span the range of the IP have been performed to elucidate aspects of rigidity percolation and the IP. These data sets are the most complete and the highest resolution data set on this system to date.

Analysis of the structure functions (in reciprocal space) and the PDFs (in real space) as well as the XAFS data at both Ge and Se edges show no correlations with the IP. The network evolves smoothly without any break in slope or discontinuity

that might be linked due to the IP. The results obtained in this study contradict previously published work [6, 7] that claim experimental evidence for a structural origin of the IP.

The so-called first sharp diffraction peak (FSDP), which is a signature of the medium range order in these glasses, changes systematically with Ge content. It develops smoothly from a low background for low Ge-content to a well-defined, sharp peak at the stoichiometric composition ($GeSe_2$). Its position shifts towards lower Q-values when Ge content is increased. The height of this peak reaches its maximum at the stoichiometric composition ($x = 0.33$), after which it starts to decrease. This is interpreted as being due to the change of the role of Ge atoms in the network. For $x < 0.33$, the Ge atoms work as a network former, so adding Ge results in a progressive increase in the correlations contributing to this peak. On the contrary, for $x > 0.33$, Ge atoms work as network modifiers. This will weaken the ordering of the correlations responsible for the FSDP and hence decrease its intensity.

The basic building block in these glasses is the $Ge(Se_{1/2})_4$ tetrahedron. For low Ge content, the tetrahedra are immersed in a floppy Se-matrix. The first PDF peak is mainly due to Ge-Se correlations. Se-Se and Ge-Ge homopolar bonds were found only in the low-Ge and high-Ge regions, respectively, consistent with the chemically ordered network (CON) model, in which Ge-Se bonds are always favored over Se-Se and Ge-Ge bonds.

To my parents, family and friends

Acknowledgments

I would like to express my regards and thanks to my thesis supervisor, Professor Simon J. L. Billinge, for his continued support and unlimited patience. His kind treatment, intellectual thinking and his clever way in solving research problems stimulated me to join his research group, which I really enjoyed working with during my research study. His supervision, recommendations, patience and encouragements are highly appreciated and will never be forgotten.

I also thank my thesis committee, Prof. Phillip Duxbury, Prof. William Wedemeyer, Prof. Chong-Yu Ruan and Prof. Carl Schmidt, for their valuable suggestions and recommendations. They, for sure, directed my research towards better understanding, learning and improvements.

I will never forget my friends and colleagues in the Billinge group: Emil Bozin, Pavol Juhas, Wenduo Zhou, Xiangyun Que, Jacques Bloch, Gianluca Paglia, Asel Sartbaeva, Ahmad Masadeh, Mouath Shatnawi, HyunJeong Kim, Hasan Yavas, Richard Worhatch, Christopher Farrow and He Lin. I enjoyed working with them. They helped me in collecting and analyzing the data. Their help and friendship are highly appreciated.

I also express my thanks and respect to all of the faculty members in the Physics and Astronomy Department at Michigan State University (MSU). Special thanks to Prof. Wolfgang Bauer (the department chair) and to Prof. S. D. Mahanti (the graduate chair) for their continued supervision on my graduate study. I thank Debbie Simmons (the graduate secretary) and Cathy Cords (the CMP secretary) for their help and care of all the aspects of my graduate study and research.

I thank Prof. Punit Boolchand from the University of Cincinnati, and his graduate student Ping Chen for making up the studied samples. Special thanks are also due to Prof. David Drabold from the University of Ohio and to his graduate student F. Inam, for their collaboration in modeling the structure of the studied samples. I

thank Prof. M. F. Thorpe from Arizona Sate University for his collaborations and suggestions in this study. I would like to acknowledge help from Douglas S. Robinson at the 6-ID beamline of the APS and Qing Ma at the 5-BM beamline of the APS for help in setting up the experiments.

Many thanks to my family in Jordan for doing everything I asked for. Their continued encouragements and support will never be forgotten. I also thank my colleagues in the Physics Department at the University of Jordan. Their continued support and encouragements are highly appreciated. I thank all of my colleagues and friends at the MSU. Their friendship facilitated my life and made it possible for me to achieve my goals. I will never ever forget the years that I lived in East Lansing. This great place for study and friendship.

This work was supported in part by US Department of Energy grant DE-FG02-97ER45651. The XRD experiments were performed at the 6ID-D beamline in the Midwest Universities Collaborative Access Team (MUCAT) sector at the Advanced Photon Source (APS). Use of the APS is supported by the U.S. DOE, Office of Science, Office of Basic Energy Sciences, under Contract No. W-31-109-Eng-38. The MUCAT sector at the APS is supported by the U.S. DOE, Office of Science, Office of Basic Energy Sciences, through the Ames Laboratory under Contract No. W-7405-Eng-82. EXAFS experiments were performed at the DND-CAT at Sector 5 of the Advanced Photon Source at Argonne National Laboratory. DND-CAT is supported by the E.I. DuPont de Nemours & Co., the Dow Chemical Company, the U.S. National Science Foundation through Grant No. DMR- 9304725, and the State of Illinois through the Department of Commerce and the Board of Higher Education Grant No. IBHE HECA NWU 96.

Contents

1 Introduction **1**

1.1 Amorphous materials 1

1.1.1 Glass transition 2

1.1.2 Preparation of amorphous materials 4

1.2 Structure and topology of disordered materials 5

1.2.1 Local structural studies 6

1.2.2 Probes of local structure 7

1.3 Constraints and rigidity percolation in covalent network glasses . . . 9

1.4 Theoretical prediction of self-organization and the intermediate phase in glasses 12

1.5 Experimental evidences about self-organization and the intermediate phase in glasses 13

1.5.1 Raman scattering 14

1.5.2 Heat flow measurements 14

1.6 Ge_xSe_{1-x} glasses as a system for studying the intermediate phase . . 21

1.6.1 Introduction 21

1.6.2 Structural analogs 22

1.6.3 Structure of glassy $GeSe_2$ 26

1.6.4 Basic structural characteristics of Ge_xSe_{1-x} glasses 28

1.6.5 Doping dependence of g-Ge_xSe_{1-x} structure 30

1.6.6 Intermediate range order in g-Ge_xSe_{1-x} 33

1.6.7 Theoretical studies of short and intermediate range structure in g-Ge_xSe_{1-x} 34

1.7 The goal of the Study 35

1.8 Layout of the dissertation 36

2 The atomic pair distribution function and X-ray absorption fine structure techniques **37**

2.1 Introduction 37

2.2 Atomic pair distribution function (PDF) 38

2.2.1 High-resolution X-ray PDF measurements 43

2.2.2 Rapid acquisition PDF (RAPDF) measurements 44

2.3 Structural information obtained from PDF method 46

2.3.1 PDF real space refinement 47

2.4 X-ray absorption fine structure (XAFS) 50

2.4.1 The XAFS phenomenon 51
2.4.2 XANES versus EXAFS 52
2.4.3 Basic principles involved in XAFS 55
2.4.4 The EXAFS equation 56
2.4.5 EXAFS measurements 58
2.4.6 Structural information obtained from EXAFS experiments . . 60
2.4.7 Joint EXAFS and PDF refinement of complex materials . . . 63

3 Search for a structural response to the IP in Ge_xSe_{1-x} glasses 65
3.1 Introduction 65
3.2 Experimental procedures and data reduction 67
3.3 Results and discussion 75
3.4 Summary and conclusions 93

4 Structural modeling of Ge_xSe_{1-x} glasses around the IP 94
4.1 Introduction 94
4.2 Structural insight from crystalline analogs 95
4.3 First principles molecular dynamics simulations on Ge_xSe_{1-x} system . 102
4.3.1 Model generation 103
4.3.2 Assessment of the MD models 103
4.3.3 Models analysis: Coordination, rings and constraints 105
4.4 Conclusions 112

5 Summary and conclusions 113
5.1 Summary and conclusions 113
5.2 Future work 117

Bibliography 119

List of Tables

1.1 Atomic structural correlations in c-$GeSe_2$. 25
1.2 Bond lengths and bond angles in Ge-Se system 29

3.1 Single bond energy in the Ge_xSe_{1-x} system. 76
3.2 χ^2-values for the different fitting protocols to the Q-space data. . . . 87

4.1 Refined fit parameters for α and β phases of c-$GeSe_2$. 100

List of Figures

1.1 Schematic illustration of a random network model in 2-dim. 2
1.2 Schematic illustration of the change in volume with temperature as a supercooled liquid is cooled through the glass-transition temperature, T_g. 3
1.3 Phase diagram of a simple binary system A_xB_{1-x}. 5
1.4 Schematic showing the dihedral angle. 6
1.5 Illustration of Se floppy and SiO_2 rigid structures. 11
1.6 Theoretical prediction of the IP based on different models. 12
1.7 Variation of the $BSe_{4/2}$ (B = Ge, Si) corner-sharing mode frequency normalized to 1 in Raman spectroscopy with respect to the mean coordination number $\bar{r}$. 15
1.8 MDSC scan of $Ge_{0.28}Se_{0.72}$ glass. 16
1.9 The non-reversing heat flow for Ge_xSe_{1-x} and $Ge_xAs_xSe_{1-2x}$ systems. 17
1.10 The crystal structure of Ge. 22
1.11 The crystal structures of Se. 23
1.12 The crystal structure of $GeSe_2$. 25
1.13 The outrigger raft model 29

2.1 Illustration for the structural origin of features in the atomic pair distribution function, G(r), for an amorphous solid. 40
2.2 Reduced structure function and PDF of Ni. 41
2.3 Raw X-ray intensity data from a sample of Ni. 44
2.4 Schematic illustration of calculating the PDF function. 49
2.5 Schematic representation of the outgoing and backscattered X-rays. . 53
2.6 Schematics of the EXAFS process. 53
2.7 Typical XAFS spectrum showing the XANES and EXAFS regions . . 54
2.8 Schematics of the XAFS transmission and fluorescence experimental setups. 59
2.9 XAFS oscillations and their Fourier transform for crystalline-Ge. . . . 62

3.1 The measured non-reversing heat flow of Ge_xSe_{1-x} glasses. 68
3.2 The reduced structure functions of Ge_xSe_{1-x} glasses. 69
3.3 The reduced pair distribution functions of Ge_xSe_{1-x} glasses. 70
3.4 k^2-weighted XAFS signal ($k^2\chi(k)$) for Ge_xSe_{1-x} glasses at both Ge and Se K-edges. 73
3.5 Magnitude of the Fourier transform of k^2-weighted XAFS signals ($k^2\chi(k)$) for Ge_xSe_{1-x} glasses at both Ge and Se K-edges. 74

3.6 Bond counting statistics for the Ge_xSe_{1-x} networks based on the RCN and the CON models. 77
3.7 Representative plot of the fit quality for both experimental and simulated first PDF peak. 79
3.8 Position of the first PDF peak for experimental and simulated data. . 79
3.9 Width of the first PDF peak for experimental and simulated data. . . 80
3.10 Bond lengths and Debye-Waller factors as obtained from XAFS analysis. 82
3.11 Representative plot of the development of the second PDF peak in Ge_xSe_{1-x} glasses. 84
3.12 Representative plot of the low-Q region in S(Q) data for Ge_xSe_{1-x} glasses. 85
3.13 Representative plot of the fit quality to the S(Q) data using different fitting protocols. 86
3.14 FSDP parameters as obtained from different fitting protocols. 88
3.15 Glass transition temperature for Ge_xSe_{1-x} glasses. 92

4.1 The crystal structure of α-GeSe2. 96
4.2 The crystal structure of β-GeSe2. 97
4.3 Comparison between calculated PDFs of the LT and HT phases of crystalline $GeSe_2$. 98
4.4 Illustration of edge-sharing and corner-sharing of tetrahedra. 99
4.5 Fit quality to the PDF of g-$GeSe_2$ using the LT and HT phases of c-$GeSe_2$. 101
4.6 Representative plot of the structure of $Ge_{0.20}Se_{0.80}$ as obtained from the molecular dynamics simulation. 104
4.7 Comparison between calculated PDFs obtained from the MD structural models with the experimental data. 105
4.8 Difference curves between successive values of x in experimental data and MD models. 106
4.9 Mean coordination number as obtained from MD simulations. 107
4.10 Ge and Se coordination statistics in the MD models. 108
4.11 Bond angle distribution and variation of concentration of types of neighbors for 2-fold Se units. 109
4.12 Concentration of corner-sharing tetrahedra and total number of rings obtained from MD simulations to Ge_xSe_{1-x} glasses. 109
4.13 Comparison between the experimental PDF of g-$GeSe_2$ and the calculated PDFs from MD model and the crystalline analogues. 111

Chapter 1

Introduction

1.1 Amorphous materials

NOTE: Images in this dissertation are presented in color.

By definition, amorphous materials are those materials that do not possess the long-range order (periodicity) that is characteristic of a crystal. Under this definition, both amorphous and non-crystalline terms are synonymous. On the other hand, the term glass is more restricted and can be defined as an amorphous solid that exhibits a glass transition at which a material changes its behavior from being glassy to being rubbery.

Randomness can occur in several forms, of which topological, spin, substitutional, and vibrational disorder are the most important. However, this randomness is not a unique property, as it must be compared to some standard as the ideal crystal in which atoms (or group of atoms or 'motifs') are arranged in a pattern that repeats periodically in three dimensions to an infinite extent.

Topological (or geometrical) disorder is a form of randomness that lacks translational periodicity, extended symmetry and long-range order as illustrated schematically in two dimensions in Figure 1.1. This type of positional disorder forms the theme of this study.

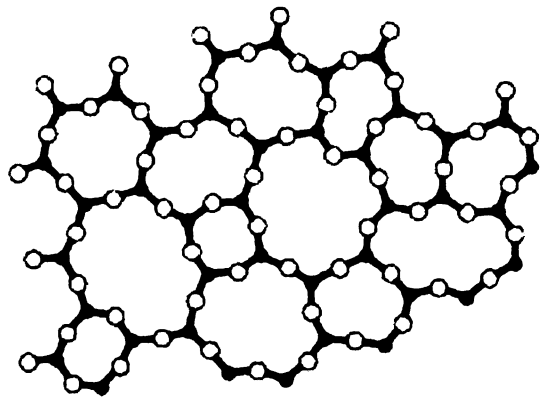

Figure 1.1: Schematic illustration of a random network model in 2 dimensions. In this model, the structural units are connected 'randomly' to give a structure which lacks periodicity [8]. Images in this figure are presented in color.

1.1.1 Glass transition

The glass transition is the phenomenon in which a solid amorphous phase exhibits a more or less abrupt change in derivative thermodynamic properties (e.g., heat capacity or thermal expansivity) from crystal-like to liquid-like values with change of temperature. This change makes the amorphous phase less thermodynamically stable than the corresponding crystalline form (i.e., possesses a greater free energy). When a material in the liquid state is cooled, one of two events may occur. Either crystallization may take place at the melting point T_m, or else, the liquid will become 'supercooled' for temperatures below T_m, becoming more viscous with decreasing temperature, and may ultimately form a glass.

The volume of the material is one of the most important parameters to monitor during the glass transition. An illustration of the change in volume with temperature is shown in Figure 1.2. As can be seen in Figure 1.2, the crystallization process is manifested by an abrupt change in specific volume at T_m, whereas glass formation is characterized by a gradual break in slope. The point over which the change of slope occurs is termed the 'glass-transition temperature' (T_g).

Certain thermodynamic variables (volume, entropy and enthalpy) are continuous

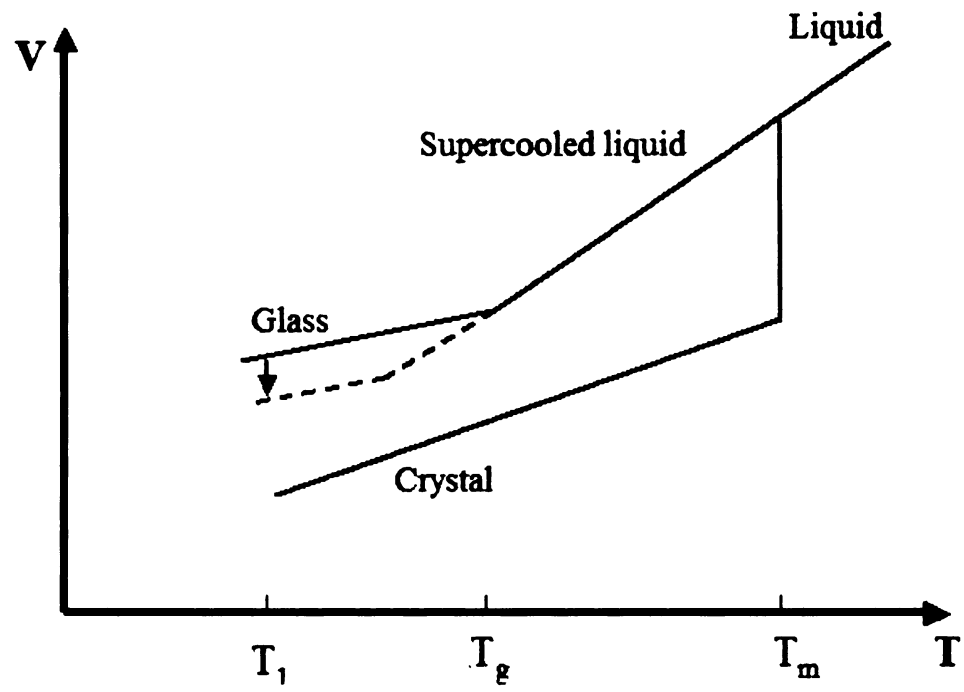

Figure 1.2: Schematic illustration of the change in volume with temperature as a supercooled liquid is cooled through the glass-transition temperature, T_g. The first order phase transition accompanying crystallization from the melt is also shown. The vertical arrow illustrates the volume change accompanying the structural relaxation or stabilization of the glass if held at temperature T_1 [9].

through the glass transition, but exhibit a change of slope there. This implies that at T_g, there should be a discontinuity in the derivative (or intensive) variables, such as the coefficient of thermal expansion ($\alpha_T = (\frac{\partial \ln V}{\partial T})_P$), the compressibility ($\kappa_T = -(\frac{\partial \ln V}{\partial P})_T$) and the heat capacity ($C_P = (\frac{\partial H}{\partial T})_P$).

A convenient way of monitoring glass-transition phenomena is by means of differential scanning calorimetry (DSC) or differential thermal analysis (DTA), which offer an excellent marker of the glass transition. In these experiments, the sample is heated at a constant rate and the changes in heat (DSC) or temperature (DTA) with respect to a reference are measured. The T_g of a particular material depends on its thermal history (heating and cooling rates), and it is not an intrinsic property of the material.

1.1.2 Preparation of amorphous materials

Preparation of amorphous materials can be regarded as the addition of excess free energy in some manner to the crystalline polymorph. This comes from the fact that the entropy of a crystal is less than that of a glass, and according to the third law of thermodynamics, a perfect crystal at absolute zero has zero entropy; this is true regardless of its size. On the other hand, a piece of disordered material, such as a glass, has some finite entropy, S_0 that is greater than zero at absolute zero.

This preparation varies widely depending on the material being prepared as well as the purpose of the preparation. Thermal evaporation [10], sputtering, glow-discharge decomposition [11], chemical vapor deposition [12], melt quenching [13, 14], gel desiccation, electrolytic deposition [15], chemical reaction, reaction amorphization, irradiation, shock-wave transformation [16], ball-milling [17] and shear amorphization are the most common methods for preparation of amorphous materials.

The glass-forming tendency (ability to form a glass) for a material depends primarily on its chemical composition. For example, in the case of a binary alloy with general formula A_xB_{1-x}, its glass-forming tendency is maximized at the so-called "eutectic" composition. At this composition, the melting (or liquidus) temperature is a minimum, as shown in the phase diagram for the A_xB_{1-x} alloy (Figure 1.3). This deep reduction in the melting point makes the liquid less supercooled at T_g, thereby reducing the possibility of crystallization.

Phillips [18] has proposed a connection between glass-forming ability and the mean coordination number. His proposal assumed that the glass-forming tendency is maximized when the number of mechanical constraints experienced by each atom (here refer to the interatomic forces acting on it) is equal to the number of degrees of freedom available to it. A system that has a number of constraints greater than the available degrees of freedom (overconstrained like Si and Ge) can not easily form a glass, although an amorphous structure may still be obtained by employing rapid

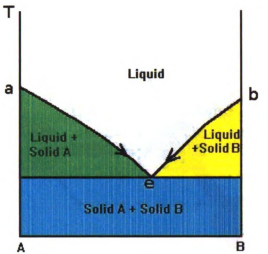

Figure 1.3: Phase diagram of a simple binary system A_xB_{1-x}. Temperatures a and b represent the melting points of A and B respectively. At A, $x = 1$. e represents the eutectic composition [9]. Images in this figure are presented in color.

cooling techniques (evaporation or sputtering).

It should be emphasized here that one should not expect glasses prepared in different ways, with different cooling rates, to exhibit a glass transition at the same temperature.

1.2 Structure and topology of disordered materials

A non-periodic arrangement of atoms could be attained solely as a result of the incorporation of variations in bond angles (for two dimensions) or bond angles and 'dihedral' angles for three dimensions in periodic arrangements. The dihedral angle is defined as the relative angle of twist between neighboring units as shown in Figure 1.4. These variations can result in a continuous random network (CRN) [19] which is considered as a metastable state, since for crystallization to occur, a substantial topological rearrangement of the structural units must occur to result in one, or at

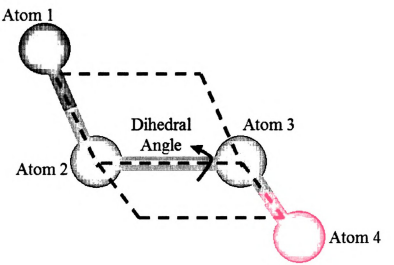

Figure 1.4: Schematic showing the dihedral angle. Images in this figure are presented in color.

most a small number of discrete values of both bond and torsion angles.

1.2.1 Local structural studies

The ultimate goal of structural studies of materials in general, and disordered materials in particular, is to enhance our understanding of the relationship between structure and properties as well as to help promote the design of new materials. The local structure of materials controls their properties as well as their functionality. Graphite (dark, soft, cheap) and diamond (transparent, hard, precious) are dramatically different materials. However, they are both made up of carbon atoms. The only difference between them is in their atomic structures. Order in a structure can itself be classified according to its spatial extent. Short-range order (SRO) describes the variation between first nearest neighbors, such as the bond length and bond angle distributions. Medium-range order (MRO) describes ordering just beyond SRO, typically the next two neighbor shells which extend to about 5 Å. This kind of order (MRO) represents the way in which the SRO configurations are brought together to

build up the network structure of the glass. Extended-range order (ERO) describes the longest spatial order observed in amorphous materials, typically up to 20 Å. Finally, long-range order (LRO) describes spatial order over macroscopic distances, where such ordering is only present in crystals and quasi-crystals [20].

It is not surprising that some degree of order (SRO and MRO) should exist in disordered solids, or even in the liquid state, because interatomic forces responsible for the crystallinity of a solid remain operative even after the solid melts and becomes a liquid. Heating the solid gives atoms thermal kinetic energy, which prevents atoms from holding to their regular positions, but the interatomic short range forces remain strong enough to impart a certain partial order to the disordered or liquid states.

On the other hand, it should be emphasized that in studying the local structure of glasses, departure from ordinary glass structure can occur in both directions, not only as a decrease in order, to give conventional defects, but also as an increase in order, leading to regions of greater perfection.

The typical method of investigating orders beyond short range order is via modeling studies in which an attempt is made to build a 'characteristic' region of the structure that can be used both to compare with experimental data and in the calculation of other properties.

1.2.2 Probes of local structure

One of the oldest experimental approaches for the study of microscopic structure is the diffraction experiment, where the use of Bragg's law proved to be very successful in determining the crystal structure. For normal ordered crystals, periodicity and symmetry of the crystal lattice are reflected in the diffraction data, and as a result, it is possible to use the signatures in the diffraction data to identify the size, shape, and symmetry of the unit cell.

Crystallographic techniques are generally not suited for structural studies of amor-

phous materials, as these materials lack long-range order and produce few, if any, diffraction peaks, and the diffraction patterns themselves are diffuse. These standard crystallographic approaches do not capture the aperiodic (disorder) information, as Bragg diffraction gives information about the "average" structure of a crystalline material, namely, the part of the structure that looks the same in each unit cell, whereas measurements of total scattering, which includes both Bragg peaks and diffuse scattering, can give information about the short-range structure.

A technique called the atomic pair distribution function (PDF) [21], that utilizes the total scattering data averaged isotropically, has proved to be successful in studying local structures of amorphous materials. Other methods that are suitable for local structural determination are: Raman spectroscopy, X-ray absorption fine structure (XAFS) and solid state nuclear magnetic resonance (NMR). As most of our work concerns the results of PDF and XAFS experiments, chapter 2 will provide an introductory account of the theory behind them.

The absence of a simple structural formalism, together with the fact that glasses are normally isotropic on a macroscopic scale, means that the maximum that can be obtained from a diffraction experiment is a one-dimensional correlation function from which the regeneration of the underlying three-dimensional structure can never be unique, and the best result that can be achieved is a structural model that is consistent with all the known data. However, even if perfect agreement were to be obtained between a model and experimental data, it is not guaranteed that other models could not be generated that would fit the data equally well.

1.3 Constraints and rigidity percolation in covalent network glasses

The notion of constraints and their application to classical macroscopic systems such as the stability of bridges have been introduced and first considered by Lagrange and Maxwell [22, 23]. On this basis, J. C. Phillips asserted [18, 24] that covalent networks can be mechanically constrained by interatomic valence forces such as bond-stretching and bond-bending and optimal glass formation is attained when the network sits at a mechanically critical point [18, 24]. This happens when the average number of constraints per atom estimated by Maxwell counting, n_c, equals the number of degrees of freedom per atom in three dimensions, i.e., $n_c = 3$.

Phillips [18, 24] considered the mechanical constraints experienced by an atom to result from the interatomic forces acting on an atom in the "valence-force-field" model, where the strain potential energy, U_s, can be expressed as a sum of contributions from bond-stretching and from bond-bending forces as given by Equation 1.1:

$$U_s = \frac{1}{2}\alpha\Delta r^2 + \frac{1}{2}\beta r_o^2\Delta\theta^2 \tag{1.1}$$

where α and β are the bond-stretching and bond-bending force constants, respectively, and Δr and $\Delta\theta$ represent small deviations in bond length and bond angle from the equilibrium values for the bond length, r_o, and the bond angle, θ_o, respectively.

In a covalently bonded network, the coordination number, N_c, for an atom which has all covalent bonds satisfied, obeys the so-called '8-N' rule (where N is the number of valence electrons, and N_c, is given by the number (8-N)).

The mean coordination number, $\bar{r}$, (which should be distinguished from N_c), plays an important role in determining connectivity and rigidity of a network. In the case of a covalently bonded binary alloy with general formula A_xB_{1-x}, the $\bar{r}$ is given by

Equation 1.2:

$$\bar{r} = xN_c(A) + (1-x)N_c(B) \tag{1.2}$$

In the mean-field approach, one considers a network of N atoms composed of n_r atoms that are r-fold coordinated. The enumeration of mechanical constraints in this system gives *r/2* bond-stretching constraints and *(2r-3)* bond-bending constraints for an r-fold coordinated atom.

M. F. Thorpe [5] examined such mechanical networks in terms of percolation theory and showed by a normal mode analysis that the number of zero frequency solutions (floppy modes (f)) of the dynamical matrix vanishes when the mean coordination number, $\bar{r}$, of the network reaches the critical value $\bar{r}_c = 2.4$. At $\bar{r}_c = 2.4$, the glassy network is stable and has a mechanical threshold or critical composition at which the network changes from an elastically floppy type to a rigid type.

The number of floppy modes, f, in a network of N atoms equals the difference between the total number of degrees of freedom ($3N$) and the total number of constraints present in the network, as given by Equation 1.3:

$$f = \{3N - \sum_r n_r(\frac{r}{2} + (2r-3))\}/3N \tag{1.3}$$

where n_r is the number of r-fold coordinated atoms. This reduces to:

$$f = 2 - \frac{5}{6}\bar{r} \tag{1.4}$$

This number of floppy modes, f, vanishes when $\bar{r} = 2.4$ [5].

According to constraint counting algorithms, a network is considered floppy if the average number of constraints per atom (n_c) is less than 3 (the number of degrees of freedom for an atom in 3 dimensions) as in the case of twofold coordinated single bond chain networks (shown in Figure 1.5(a)). On the other hand, the network is rigid if n_c is greater than 3 as in networks consisting only of tetrahedral units (such

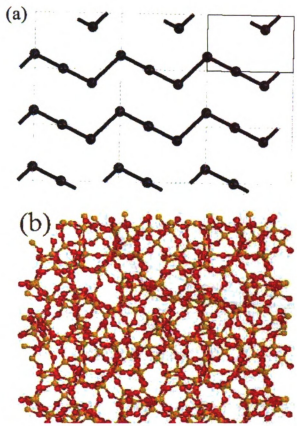

Figure 1.5: (a) Se chain structure (floppy) and (b) SiO_2 tetrahedral network structure (rigid) [25]. Images in this figure are presented in color.

as the SiO_2 network shown in Figure 1.5(b)). Thus progressive addition of cross linking elements (such as As or Ge) to a starting chain network (such as S or Se) will result in a progressive increase of its connectivity (mean coordination number). At $\bar{r} = 2.4$, the rigidity percolation occurs where the network changes from floppy to a rigid structure.

The floppy to rigid transition was first theoretically predicted and then numerous experiments [26, 27, 28] have confirmed it, especially in glass science were chalcogenide glasses have been used as a benchmark. Various examples about the occurrence of a rigidity percolation threshold and its application in granular matter, biology and computational sciences have been reported [27, 29, 30, 31, 32, 33].

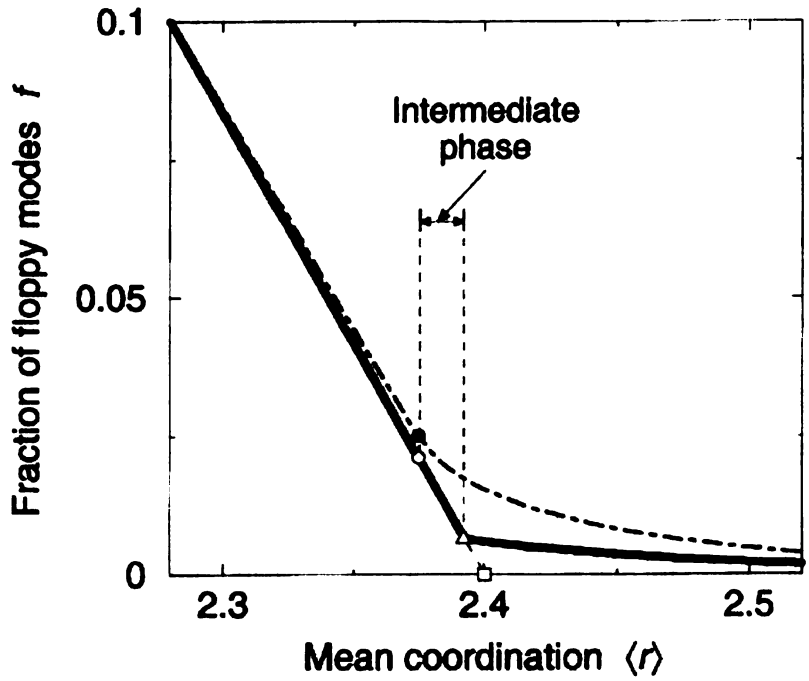

Figure 1.6: Showing the number of floppy modes plotted against the mean coordination for Maxwell counting (shown as a partly obscured dashed line) with the associated mean field transition shown by the open square at $< r > = 2.4$, and for a randomly diluted diamond lattice using a dot-dash line, where the second-order transition is indicated by the solid circle at $< r > = 2.375$. The self-organized model, where stressed regions are avoided, follows the Maxwell curve, and is shown by a solid line, and gives a second-order transition at $< r > = 2.375$, shown by an open circle, from a floppy to an unstressed rigid state and a first-order transition at $< r > = 2.392$, shown by an open triangle, to a stressed rigid state. The range of $< r >$ over which the intermediate phase exists is indicated [1].

1.4 Theoretical prediction of self-organization and the intermediate phase in glasses

In a mean-field theory, the variation of the number of floppy modes per atom, f, with the mean coordination number, $\bar{r}$, is linear as given by the Equation 1.4. This result is shown in Figure 1.6, where the transition (from floppy to rigid) at a mean coordination of 2.4 is indicated by an open square. In applying Maxwell's counting on

randomly diluted diamond lattices, where the network is decomposed into unstressed (isostatic) rigid regions, and stressed (overconstrained) rigid regions, with flexible joints, Thorpe *et al.* [1] found that the Maxwell's counting is a good guide, and the transition occurs at a mean coordination of 2.375, as shown in Figure 1.6.

Thorpe *et al.* [1] proposed that a network can self-organize at it's fictive temperature (the temperature at which the glass is formed). The term self-organization here refers to the subtle way by which the structure can incorporate non-random features to minimize the free energy at the temperature of formation. In studying a self-organized model of random network in which configurations that are stressed are avoided if possible, Thorpe *et al.* [1] found that this avoidance leads to two-phase transitions and an intermediate phase that is rigid but stress-free (unstressed) as can be seen in Figure 1.6. By unstressed we mean that each bond length (angle) can have its natural length (angle) without being forced to change by the surrounding environment. Otherwise, a bond is stressed.

The transition at $\bar{r}_{c1}$ is assumed to be due to the change of the network from *floppy* to an *isostatic (stress-free) rigid phase*, and the second transition at $\bar{r}_{c2}$ is assumed to be due to the change from an *iso-static* to a *stressed rigid phase.* These two transitions at $\bar{r}_{c1}$ and $\bar{r}_{c2}$ define an intermediate phase (IP) in which the connected structure continues to be stress-free (isostatically rigid) [1, 4]. $\bar{r}_{c1}$ and $\bar{r}_{c2}$ represent the lower and upper boundaries of the IP, respectively. The width ($\Delta\bar{r}$) of the IP is given by the difference $\bar{r}_{c2}$ - $\bar{r}_{c1}$.

1.5 Experimental evidences about self-organization and the intermediate phase in glasses

Some preliminary experimental evidence supports the picture of the IP. Chalcogenide glassy systems (materials containing a group VI atom) have been carefully studied

and the intermediate phase (IP) defined by two transitions has been discovered by Boolchand *et al.* [3, 4] in the context of self-organization. Following is a description of experimental findings that were interpreted as signatures of the intermediate phase.

1.5.1 Raman scattering

Boolchand *et al.* [3] suggested from Raman scattering and phase-dependent measurements of the kinetics of the glass transition that *two* transitions at $\bar{r}_{c1}$ and $\bar{r}_{c2}$ appear when the network stiffens. Their Raman scattering measurements on Ge_xSe_{1-x} or Si_xSe_{1-x} glasses [3, 34], that probe the elastic thresholds in these binary glasses, indicated that Ge or Si corner-sharing mode chain frequencies change with mean coordination number, $\bar{r}$, of the glass network. These frequencies exhibit not only a change in slope at the mean coordination number near $\bar{r}_{c1} = 2.4$, but also a first-order jump at the second transition $\bar{r}_{c2}$. In germanium systems, the second transition is located around the mean coordination number of 2.52, whereas it is 2.54 in Si-based systems. For both systems, a power-law behavior in $\bar{r} - \bar{r}_{c2}$ is detected for $\bar{r} > \bar{r}_{c2}$ (see Figure 1.7 [35]) and the corresponding measured exponent is very close to the one obtained in numerical simulations of stressed rigid networks [36].

1.5.2 Heat flow measurements

In conventional differential scanning calorimetry (DSC) measurement, the signature of softening of a glass is an endothermic (a process or reaction that absorbs energy in the form of heat) heat flow with respect to an inert reference sample as the temperature of the glass and reference sample is swept linearly in time at a controlled rate, usually 20 °C/min.

A more sensitive variant of DSC is the so-called temperature-modulated DSC or MDSC [37]. With MDSC, the endotherm, as one passes through T_g can be deconvoluted into two contributions; a reversing and a non-reversing heat flow [38]. The

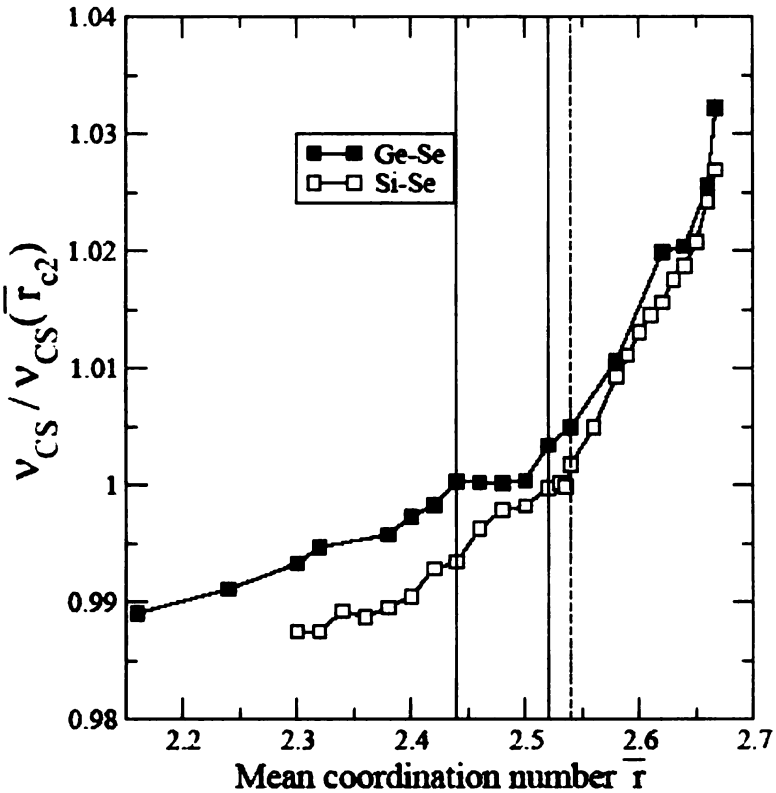

Figure 1.7: Variation of the $BSe_{4/2}$ (B = Ge, Si) corner-sharing mode frequency normalized to 1 in Raman spectroscopy with respect to the mean coordination number $\bar{r}$. The solid vertical lines define the intermediate phase in Ge-Se [3] while the lower solid line and the dashed line define it for Si-Se. The intermediate phase in case of Si_xSe_{1-x} is larger than the Ge_xSe_{1-x} one [35].

deconvolution is made possible by programming a sinusoidal temperature variation ($A \sin \omega t$) on the linear ramp ($\Delta T/t$) [37], and deducing the part of the heat flow that tracks the sinusoidal temperature variation using fast-Fourier transform. The part of the heat flow that tracks the temperature oscillations is called the reversing heat flow [37], and the remainder that does not track the periodic temperature variation and is thus called the non-reversing heat flow [37]. The difference signal between the total heat flow and the reversing heat flow, defines the non reversing heat flow. Figure 1.8 shows MDSC scans of a $Ge_{0.28}Se_{0.72}$ glass [39] illustrating the deconvolution of heat flow into the non-reversing and reversing components.

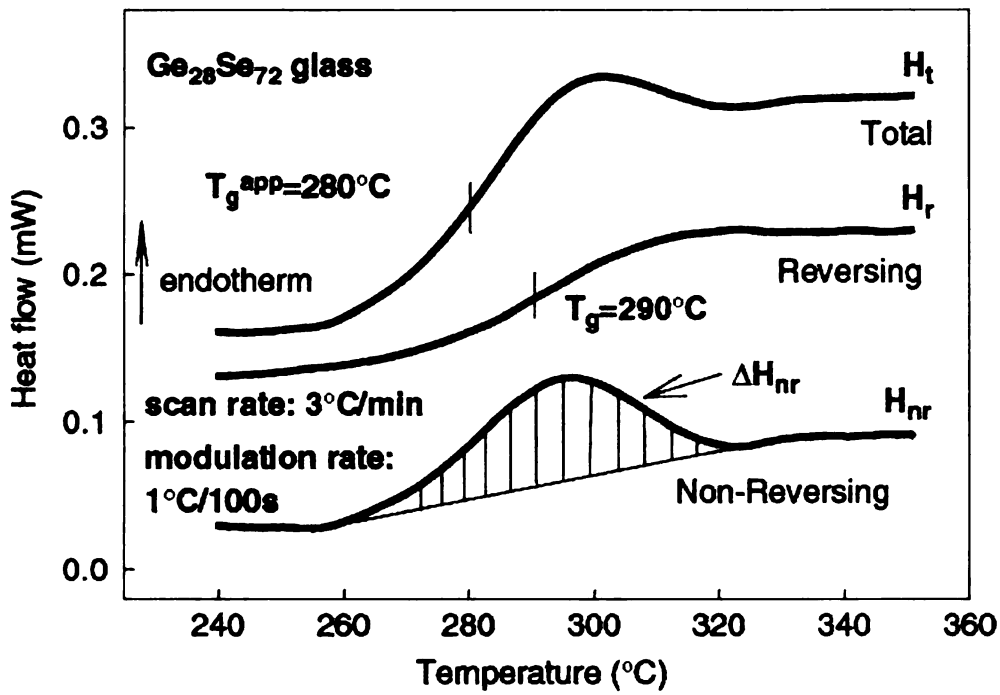

Figure 1.8: MDSC scan of $Ge_{0.28}Se_{0.72}$ glass displaying a $T_g = 290$ °C from inflexion point of the reversing heat flow, and a non-reversing enthalpy, ΔH_{nr}, illustrated by the hash-marked region. The large width ~ 60 °C of the non reversing heat flow signal is characteristic of networks that are stressed rigid [39].

MDSC experiments on a variety of glasses reveal, in general, a reversing heat flow with a step-like change, while the non reversing heat flow has a Gaussian-like profile shown in Figure 1.8 for the case of a $Ge_{0.28}Se_{0.72}$ glass [39]. The inflexion point of the reversing heat flow signal is taken to define the glass transition temperature, T_g, while the shaded area in Figure 1.8 yields the frequency uncorrected non-reversing enthalpy, ΔH_{nr} (while heating up), associated with the melting transition. In these experiments, it is usual to scan up in temperature followed by a scan down in temperature. Hence, the frequency-corrected non-reversing enthalpy, ΔH_{nr}, is obtained by taking the difference ΔH_{nr} (up) - ΔH_{nr} (down).

There is no rigorous theory for the decomposition shown in Figure 1.8, but it is eminently plausible to interpret the reversing component of heat flow as measuring

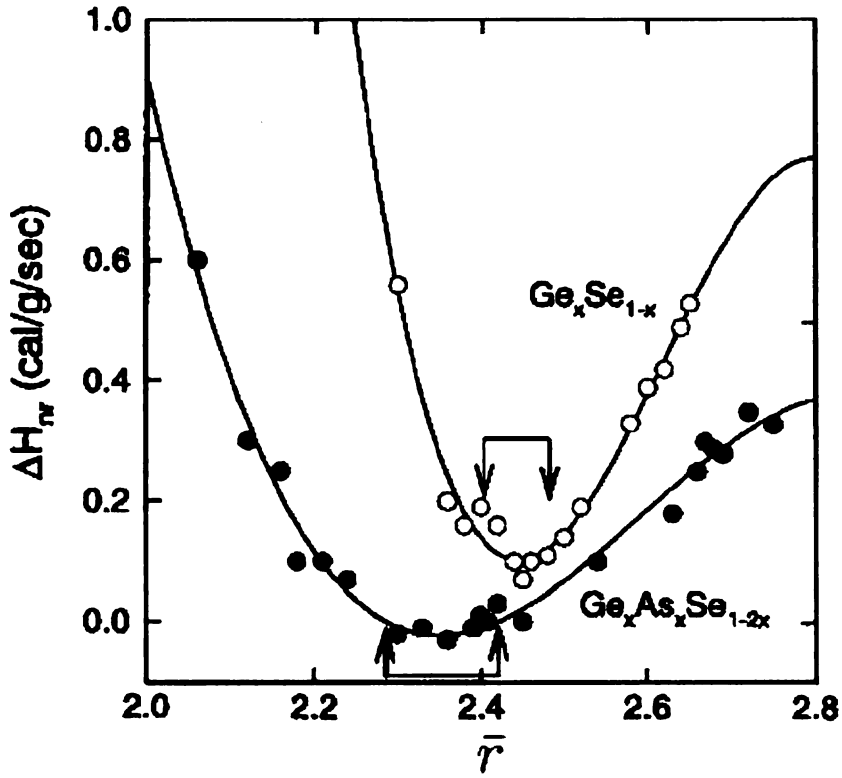

Figure 1.9: The non-reversing heat flow for Ge_xSe_{1-x} (open circles) and $Ge_xAs_xSe_{1-2x}$ (filled circles). Figure is taken from reference [45].

the quasi-equilibrium specific heat of the system as if it were halted at each structural stage of its transition from glass to melt (or the reverse). On the other hand, the non reversing heat flow measures the heat absorbed by the system as it passes through the stages of the transition. Aspects of structural arrest, aging and thermal history that characterize the non-ergodic character of T_g, are all manifested in the non-reversing enthalpy [38].

Boolchand *et al.* [4, 38, 40, 41, 42, 43, 44] carried out MDSC experiments on different glassy systems, performed as a function of network mean coordination number, $\bar{r}$. They showed regions near $\bar{r} \sim 2.4$, for which the ΔH_{nr} term nearly vanishes as can be seen in Figure 1.9 which provides the results of the non-reversing heat flows, ΔH_{nr}, for both Ge_xSe_{1-x} and $Ge_xAs_xSe_{1-2x}$ glasses. It is clear that in both cases the ΔH_{nr}

has a deep minimum centered near $x = 0.23$ in case of Ge_xSe_{1-x} glasses and around $x = 0.19$ in case of $Ge_xAs_xSe_{1-2x}$ glasses. For under-constrained and over-constrained glass, the ΔH_{nr} is sizable, on the other hand, it almost vanishes for an optimally coordinated glass (glass where the number of constraints per atom is equal to or close to the total number of degrees of freedom (3)) [46], so the non-reversing heat flow is considered as an indicator for the optimally coordinated glass sample. In subsequent studies, the behavior of almost zero non-reversing heat flow in a finite composition width was recognized as being a universal feature. They called the composition range for these thermally reversing transitions the intermediate phase (IP) or reversibility windows.

A more recently realized feature of glass compositions in the IP window is the absence of aging [47]. There is a purely thermodynamical connection between the near vanishing of the non reversing heat flow, ΔH_{nr}, and the absence of aging. Since $\Delta S = S_{melt} - S_{glass} = \int dH_{nr}/T$, where $\Delta T \ll T_g$ is the width of the melting transition, then $\Delta S \sim \Delta H_{nr}/T_g$ [39]. Note that the reversing heat flow H_r, or specific heat, is not included; thus the change in the vibrational entropy is not counted and S here is the configurational entropy only. Outside the window the values of ΔS are larger, so S_{glass} is smaller there if we assume that S_{melt} does not change dramatically in that range of composition. This means that the entropy of melting is small and that S_{glass} is a maximum for glasses in the window. Now, aging of a system requires it to diffuse over the energy landscape into configurations of higher entropy. These are absent in the window, so the intermediate phase should not age (at least not much). In the chalcogenides this means the networks, for compositions in the intermediate phase, are formed from molecular units, so called isostatic units, which link together without incurring energy increasing distortions (or stress). For example, in the Ge_xSe_{1-x} glass system, the backbone structures are formed from corner sharing (CS) $GeSe_4$ units and edge-sharing (ES) $GeSe_2$ units. The number of differently linked clusters of nearly the

same energy is large and is comparable with the configuration entropy of the liquid. So the large scale isostatic network samples a large number of energetically equivalent configurations over time. This has a direct bearing on the self-organization feature. In contrast, if the molecular units are made up of stressed units with redundant bonds, there are energy barriers between different configurations and entropy of the network decreases.

The connection between thermal properties of Ge_xSe_{1-x} glasses and their elastic behavior has emerged from Raman scattering measurements [42, 43, 44, 48]. The Raman determined optical elasticity shows different power laws for glass compositions in reversibility windows, and for those outside these windows, as discussed above. The observed power laws are consistent with available numerical simulations [36, 49].

The IP window in binary Ge_xSe_{1-x} glasses was found to occur in the $0.20 < x < 0.25$ range, and has been established by detailed compositional studies [47]. The correlation between thermal and optical behavior of the Ge_xSe_{1-x} glasses places glass compositions at $x < 0.20$ to be in the flexible elastic phase, those in the $0.20 < x < 0.25$ range to the intermediate phase, while those at $x \geq 0.26$ to the stressed-rigid elastic phase [47, 48].

The two properties, $\Delta H_{nr} \sim 0$ and non aging have been theoretically connected with the concept of self-organization of the disordered networks lying in the reversibility window [1]. Hence, from the above discussion, it is predicted that compositions in the IP region are stress-free and self-organized.

It should be emphasized that the experimental positions of the IP, as found by Boolchand *et al.* (from $< r > = 2.40$ to 2.45) do not coincide with the theoretical prediction (from $< r > = 2.375$ to 2.392), which is probably due to the simplicity of the theoretical models. On the other hand, the theory predicts that the IP is about three times narrower than the experimental finding of Boolchand's *et al.* These two discrepancies between theory and experiment about the IP casts some doubt on

making the equivalence between the two.

Despite the fact that covalent bonds are rather stiff and highly directional, it should be emphasized that there are other interactions in the structure that may act as constraints, for example, Van Der Waals interactions. These kinds of constraints are not counted in Maxwell's constraint counting algorithm, as it just counts bond stretching and bond-bending constraints. This leakage might be considered as a reason for the discrepancy between the predicted and experimental finding of the IP. A methodology that can suppress non-covalent interactions in the network is necessary to validate Maxwell's counting algorithm. On the other hand, a new algorithm that incorporates non-covalent constraints might narrow the gap between the predicted and the experimentally-found IP.

Micoulaut *et al.* [35], using size-increasing cluster combinatorics and constraint counting algorithms, showed that the second transition at $\bar{r} = \bar{r}_{c2}$ (the 'stress transition') is a first-order transition while the first transition at $\bar{r}_{c1}$ is weakly second order.

Self-organization of the network can be thought of as the creation of a stress free basic unit that agglomerates to generate new clusters of larger size provided that stressed rigid regions can be avoided. Upon increasing $\bar{r}$, isostatic rigid regions are accumulated. However, there will be a limit to this accumulation (which is the upper boundary of the IP ($\bar{r}_{c2}$)) at which stressed rigid regions can no longer be avoided, which results in the second "stress" transition.

1.6 Ge_xSe_{1-x} glasses as a system for studying the intermediate phase

1.6.1 Introduction

For studying the IP and rigidity percolation in glasses, a system where the mean coordination number can be systematically and smoothly changed in the region $2 < \bar{r} < 3$ to straddle the rigidity percolation threshold of $\bar{r}_c$=2.4 is needed. A floppy network consisting of chains of atoms (i.e., coordination number is 2) with varying doping ratios of cross linking element (i.e., coordination number is 4) will smoothly change the mean coordination number of the entire network.

The Ge_xSe_{1-x} system with $0.15 \leq x \leq 0.40$, offers an excellent candidate to test the concept of rigidity percolation and IP. In this system and according to the '8-N' rule (here N stands for the column number in the periodic table), Ge is 4-fold coordinated and Se is 2-fold coordinated, which results in a mean coordination number of $2 + 2x$. Increasing, the Ge content in the glass will smoothly increase the connectivity of the network and the rigidity percolation threshold will be reached at 20 atomic % Ge (i.e., x=0.20). Coupled with the extent of knowledge on this system, and the wide compositional range over which it can be made in the glassy state, Ge_xSe_{1-x} is an ideal model system for IP studies.

On the other hand, Ge_xSe_{1-x} glasses are of special interest, as they have a large range of transparency from 0.6 to 30 μm, and they have good mechanical properties, such as hardness, adhesion, low internal stress, and water resistance [50, 51, 52], which make them very useful in infrared optics, and memory cells. These materials have long been under development for use as passive optical components in the infrared and as active electronic device components for photocopying, ultramicrolithography and electronic switching.

Ge_xSe_{1-x} are canonical binary network glasses, that can be made as glasses over

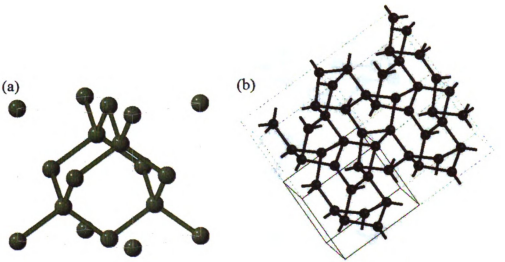

Figure 1.10: The crystal structure of Ge. (a) one unit cell, and (b) multiple unit cells [56]. Images in this figure are presented in color.

a wide composition range (x = 0.0 to 0.42 of germanium) [50, 51, 53, 52] allowing systematic composition dependence to be studied. These glasses, when heated above room temperature, exhibit a glass transition, (T_g) [8] with thermodynamic signatures including an abrupt change in specific heat, compressibility, and thermal expansion. They have a number of crystalline analogs that facilitate structural comparisons [54, 55] and make it possible to investigate short as well as medium range orders.

1.6.2 Structural analogs

Here we provide a brief summary of the structures of several relevant elements and compounds that will be used as a reference in this study.

Crystalline Ge

The crystalline Ge structure is described by cubic close-packed (ccp, diamond), with space group Fm-3m (space group number 225) and a cubic unit cell with dimension of 5.658 Å. A schematic of the crystal structure of Ge is shown in Figure 1.10.

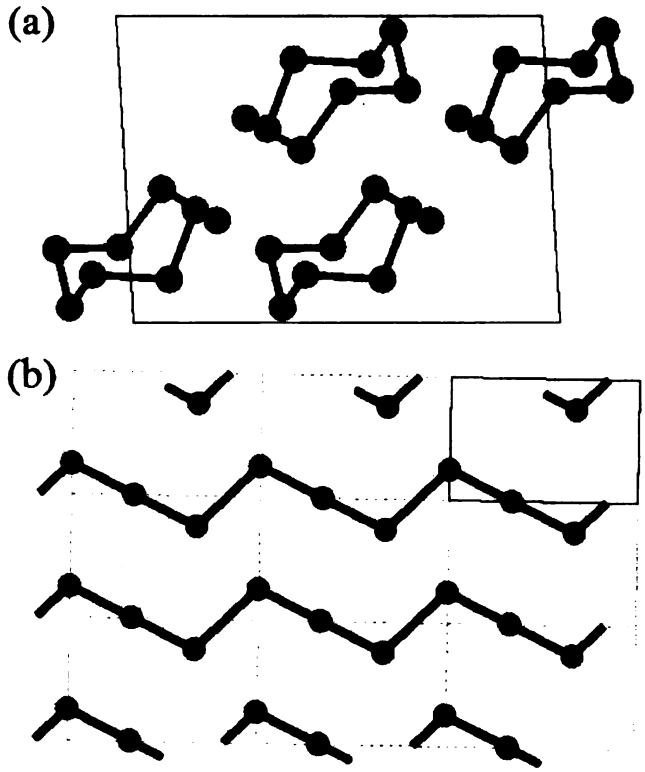

Figure 1.11: The crystal structures of Se. (a) α-Se ring structure [59] and (b) trigonal-Se chain structure [25].

Crystalline Se

Crystalline selenium has two allotropic forms; the trigonal structure (t-Se) [57], which is the most stable form, is made up of $[Se]_n$ chains, while the α-selenium structure [58] is built up from Se_8 rings as is the iso-structural type α-sulfur structure. A schematic of the structures of c-Se is shown in Figure 1.11.

The t-Se has a hexagonal Bravais lattice, with three atoms in the primitive cell. The atoms are arranged along helicoidal chains, which winds an angle of 120° between first neighbors. The atoms in a given chain are covalently bonded to a third atom (second neighbor) on a parallel chain. Each Se atom in t-Se has a strong covalent bond with first neighbor and weak bond with second neighbor.

Amorphous Ge

The strong preference of the Ge atoms for four-fold coordination gives rise to fully three-dimensional structures in both crystalline and amorphous forms. Early evidence for the amorphous phases being actually microcrystalline [60] has been shown to be inconclusive, so that the random network model is now widely accepted.

Amorphous Se

As might be expected for two-fold coordinated atoms, the SRO of the solid amorphous phase of Se is based on rings or chains of atoms in varying proportions. Diffraction studies on amorphous Se suggest that the bulk glass is comprised largely of bent helical chains, but that evaporated or sputtered thin films have varying proportions of rings and chains [61, 62, 63, 64].

Crystalline $GeSe_2$

The structure of crystalline $GeSe_2$ provides a starting point for discussing the structure of the glassy as well as for the liquidus phases. The short-range structures are clearly similar, since $Ge(Se_{1/2})_4$ tetrahedra form the structural basis of all three phases. The intermediate-range data are clearly different. Figure 1.12 shows the crystal structure of $GeSe_2$ which consists of $Ge(Se_{1/2})_4$ tetrahedra that are linked to each other by both corners and edges.

Atomic structural correlations in crystalline $GeSe_2$ at room temperature are shown in Table 1.1 [54, 66], where, for better comparison with the glassy data, the number of distances of each type of correlation were grouped into coordination shells.

For each shell s, the mean distance (r_s), variance (σ_s^2) and coordination number

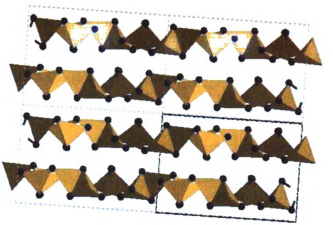

Figure 1.12: Polyhedral representation of the crystal structure of $GeSe_2$ [65]. Images in this figure are presented in color.

Table 1.1: Atomic structural correlations in c-$GeSe_2$.

Shell no. s	Type of correlation (dd')	Mean distance r_s(Å)	Variance σ_s^2(Å^2)	Coordination no. C_d(d')
1	(Ge-Se)	2.355	0.00009	4
2	(Ge-Ge) edge-sharing	3.049	0.0	0.5
3	(Ge-Ge) corner-sharing	3.551	0.00118	3
4	(Se-Se) within tetrahedra	3.826	0.02511	9.5
4(cont.)	(Se-Se) within layers			
4(cont.)	(Se-Se) between faces			

(C_d(d')) for the crystal are defined by:

$$r_s = \frac{1}{n_s} \sum_{i \in s} r_i \tag{1.5}$$

$$\sigma_s^2 = \frac{1}{n_s} \sum_{i \in s} (r_i - r_s)^2 \tag{1.6}$$

$$C_a(b) = \frac{n_s}{n_a} \tag{1.7}$$

for a coordination shell between atoms of types a and b, where n_s is the number of

atom pairs contributing to the shell s, and n_a is the number of atoms of type a in the unit cell.

1.6.3 Structure of glassy $GeSe_2$

$GeSe_2$ glass has received particular attention as a prototypical glass in order to understand the nature of the equilibrium network glass. As a prototypical glass, it works as a model and as a bench mark for many chalcogenide glasses. Consequently its structure and properties have been studied extensively.

Nemanich *et al.* [67] using Raman scattering and neutron scattering identified the A1 mode to be due to CS tetrahedra and the A1 companion mode to be due to n-fold rings (n = 4, 5 and 6). On the other hand, Bridenbaugh *et al.* [68] using Raman scattering identified the A1-companion mode as a mode of Se-Se cluster edge bonds, and proposed Ge-rich and Se-rich clusters for $GeSe_2$ glass. This agrees with the findings of Murase *et al.* [69] where the mode at 246 cm^{-1} was assigned to be due to bond-stretching and the mode at 145 cm^{-1} was assigned to be due to bond-bending. Sugai [70] using Raman scattering showed that A_1 and A_1 companion are identified with CS and ES tetrahedra and the glass structure is described as a stochastic network. This also agrees with the finding of Nemanich *et al.* [71] which identified the A1 companion mode as mode of ES tetrahedra and the glass structure is described as a COCRN. ^{129}I Mössbauer emission spectroscopy [72] and ^{119}Sn Mössbauer spectroscopy [73] found a finite concentration of Se-Se bonds and Ge-Ge bonds in $GeSe_2$ glass, respectively. Vashishta *et al.* [74] analyzed the structure factor of $GeSe_2$ glass and liquid, measured by Susman *et al.* [66] using two- and three-body forces for a 648-atom model of $GeSe_2$ and identified the origin of the first sharp diffraction peak to be due to Ge-Se and Ge-Ge correlations between 4 and 8 Å. Cobb and Drabold [75] and Cobb *et al.* [76] using *ab-initio* molecular dynamics for a 216-atom model calculated the vibrational and electronic densities of states, and showed that four- and

six-membered ring correlations contribute to the first sharp diffraction peak. In another *ab-initio* molecular dynamics study for a 120-atom model, Massabrio *et al.* [77] analyzed the structure factor and partial distribution functions of $GeSe_2$ liquid, and showed that the liquid structure is composed of regular $Ge(Se_{1/2})_4$ tetrahedra coexisting with homopolar bonds and threefold centers, but in their study, the origin of the first sharp diffraction peak is unclear.

Susman *et al.* [66] using the neutron structure factor of $GeSe_2$ glass and liquid showed that the glass structure is composed of CS and ES tetrahedra, similar to that of α-$GeSe_2$. Penfold and Salmon [78] using the neutron partial distribution function measured in $GeSe_2$ using isotopic substitution showed experimental evidence for a finite concentration of homopolar bonds in liquid $GeSe_2$. In a recent neutron partial distribution function measured in $GeSe_2$ glass using isotopic substitution, Pitri *et al.* [79] confirmed the existence of a finite concentration of Ge-Ge and Se-Se bonds in $GeSe_2$ glass with high concentration of distorted CS $Ge(Se_{1/2})_4$ tetrahedra. In a recent Raman scattering, ^{119}Sn Mössbauer spectra and MDSC on Sn-doped Ge_xSe_{1-x} glasses, Boolchand *et al.* [34] showed that T_g(x) variation is correlated to Ge-Ge bond concentration and the ethane units ($Ge_2(Se_{1/2})_6$) are not part of the tetrahedral backbone.

Raman spectroscopy suggests that the ratio of edge-shared to corner-shared tetrahedra is 0.5(3) in g-$GeSe_2$ and the proportion of Ge-Ge bonds is 2% [34]. Mössbauer data on lightly ^{119}Sn doped Ge_xSe_{1-x} samples also detect two sites for Ge; tetrahedral and non-tetrahedral, the latter being assigned to the ethane-like $Ge_2(Se_{1/2})_6$ clusters [34]. These results can be compared to isotope substitution partial PDF studies [80, 79] that find the proportion of edge-shared tetrahedra to be 50% and that of Ge-Ge bonds to be 3.7(2)% in rather good agreement with the spectroscopic results. The presence of a small concentration of Ge-Ge bonds in g-$GeSe_2$ implies some Se-Se bonds and there is experimental evidence that these exist from ^{129}I Mössbauer

emission spectroscopy measurements [72, 81] and Raman scattering [34].

A chemically ordered continuous Random network (COCRN) model was proposed for the structure of g-$GeSe_2$ [71]. However, measurements suggest that the intrinsic chemical order of the glass is, however, broken with a maximum of 25(5)% Ge and 20(5)% Se being involved in homopolar bonds at distances of 2.42(2) and 2.32(2) Å, respectively [79]. Therefore a defective COCRN model has been suggested [9]. A model for g-$GeSe_2$ assumes that its structure is made up of stacked chalcogenide-covered wafers, with an average diameter and stacking thickness of order 10-20 Å [68].

These results can be qualitatively reconciled with a model that implies some degree of chemical inhomogeneity, known as the outrigger raft model [68, 24, 82]. Se-rich regions of the structure resemble the layered structure of the high-temperature crystalline phase, with chains of corner-shared $Ge(Se_{1/2})_4$ bridged by edge-shared tetrahedra as shown in Figure 1.13. Stoichiometry is maintained by regions of the material with $Ge_2(Se_{1/2})_6$ type clusters [68].

1.6.4 Basic structural characteristics of Ge_xSe_{1-x} glasses

The basic structural units in the Ge_xSe_{1-x} network are the $Ge(Se_{1/2})_4$ tetrahedra [83, 79], and the Se_n chains [84]. The way in which these tetrahedra are linked together and the existence of long or short Se_n chains depend on the Ge content in the network.

The covalent bonding in the Ge_xSe_{1-x} network gives rise to well-defined bond lengths and bond angles as shown in Table 1.2 [85]. Ge is 4-fold and Se is 2-fold coordinated at all compositions.

Ge-Ge homopolar bonds are absent at small values of x. Careful structural study by determining partial structure factors from isotopic substitution neutron PDF analysis [80] tentatively suggested their existence in g-$GeSe_2$. This seems to have been confirmed in a more careful recent determination of the PDF partials [79].

Evidence for edge-shared tetrahedra comes from the observation of a split peak

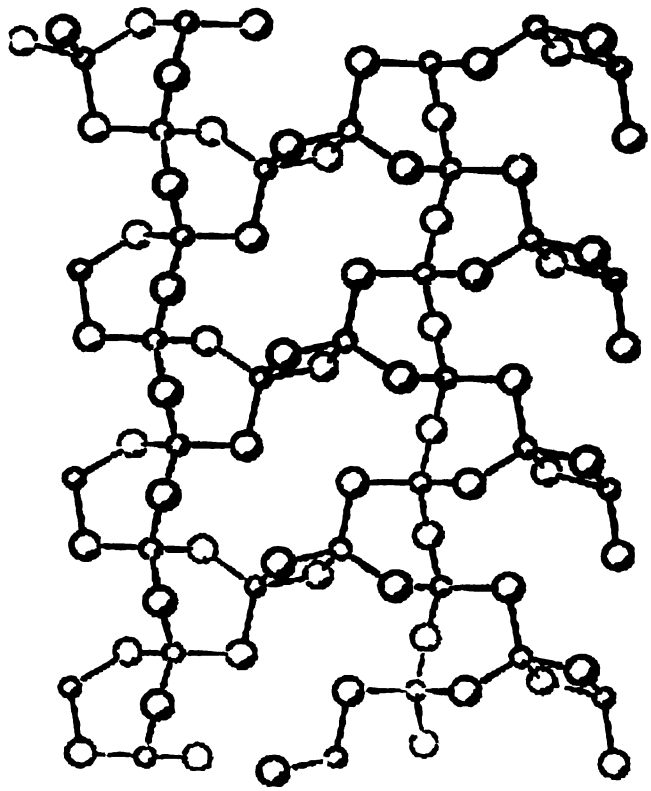

Figure 1.13: The outrigger raft model [68].

Table 1.2: Bond lengths and bond angles in Ge-Se system

Parameter	Value
Ge-Ge distance	2.44 Å
Ge-Se distance	2.38 Å
Se-Se distance	2.34 Å
Se-Se-Se bond angle	105^{o}
Se-Ge-Se, Ge-Ge-Se, Ge-Ge-Ge bond angles	$109^{o}28^{'}$
Ge-Se-Se, Ge-Se-Ge bond angle	102^{o}

around 210 - 220 cm^{-1} in Raman scattering [68, 71]. Bridenbaugh *et al.* [68] noticed the existence of a Raman peak at 219 cm^{-1} in the high-temperature β-structural phase, which includes edge-shared tetrahedra, similar to that seen in the $GeSe_2$ glass. The frequency of this anomalous mode can be rationalized from using the Sen-Thorpe lattice dynamics model [71, 54], applied to edge-shared tetrahedra, also thought of as "four atom rings" [71]. Also, the intensity of this Raman peak varies in the expected way with doping [71]. Evidence for the existence of edge-shared tetrahedra also comes from intensity in the PDF around $r = 3.05$ Å from Ge-Ge distances in neighboring tetrahedra [66].

Nemanich *et al.* [71] also demonstrate a surprisingly good agreement between the local structure in the crystalline β-phase and in $GeSe_2$ glass, as measured in a low resolution PDF from neutron scattering data. In β-$GeSe_2$ there exist equal numbers of edge- and corner-sharing $Ge(Se_{1/2})_4$ tetrahedra which gives two nearest-neighbor Ge-Ge distances at 3.05 and 3.55 Å, the shortest being the distance between the centers of edge sharing motifs [79].

1.6.5 Doping dependence of g-Ge_xSe_{1-x} structure

The structure of Ge_xSe_{1-x} glasses depends ultimately on the Ge content. At the low Ge content ($x < 0.31$), no Ge-Ge homopolar bonds are detected [34], but their number grows rapidly above $x = 0.33$ [34]. For the region $x > 0.33$, a phase separation into Ge-rich and Se-rich regions has been postulated [34].

Many structural models have been proposed to describe the structure of Ge_xSe_{1-x} glasses. Some of these models are consistent with some experimental data but fail to describe other features seen in other experimental data. Here we provide a description of these various models considered for the structure of the Ge_xSe_{1-x} system:

Random covalent network (RCN) model or Bett's model:

The structure of glass in this model [86] is essentially three dimensional, where the

distribution of bond types is purely statistical [9].

Chemically ordered network (CON) model [71]:

In this model, the glass structure is assumed to be composed of cross-linked structural units of the stable chemical compounds (of the system) and excess, if any, of the elements. According to this model, formation of heteropolar bonds is favored over the formation of homopolar bonds at all compositions. Consequently, Ge-Se bonds are favored such that Ge-Se and Se-Se bonds are allowed on the Se-rich side of the $GeSe_2$ composition ($x < 1/3$), while only Ge-Se and Ge-Ge bonds are allowed on the Ge-rich side ($x > 1/3$). A more complete description of this model will be provided in Chapter 3.

Both the RCN and the CON models give the same mean coordination number of $\bar{r} = 2 + 2x$ (a condition that must be satisfied if, in accordance with the '8-N' rule, Ge is fourfold coordinated and Se is twofold coordinated in Ge_xSe_{1-x} glasses). The difficulty in distinguishing these two models lies in the characterization of the intermediate-range atomic arrangements of materials which have no long range order.

Chain crossing model (CCM) [24]:

In this model, the Se chain structure is maintained, but the four-fold, tetrahedrally coordinated Ge atoms act as chain crossing sites, with Ge-Ge bonds not allowed for $x \leq 1/3$.

For chalcogen-rich glasses, this model (CCM) considers a homogenous glassy structure made up of short chalcogen chains $[Se]_n$ cross-linked by isolated $GeSe_4$ tetrahedra.

Phillips' outrigger-raft model:

This model was proposed by Phillips for the structure of $GeSe_2$, where the CCM has been used to interpret the layer structure in glasses. This model consists of an array of $GeSe_{4/2}$ tetrahedra, but these units are covalently bonded together in layers having atomic arrangements which are similar to the layers of crystalline $GeSe_2$. Each

layer consists of parallel chains of corner-sharing tetrahedra, cross-linked with pairs of edge-sharing tetrahedra as shown in Figure 1.13. These layers in the glass, as well as in the crystal, are held together by Van Der Waals forces, and these layers are terminated by Se-Se dimers parallel to the chain. Inherent in this model is that homopolar bonds are an intrinsic part of the structure.

Results from Raman and Mössbauer spectroscopy as well as pressure and optical measurements and laser recrystallization studies of α-$GeSe_2$ have been used to support and extend this model.

By contrast, neutron scattering and modeling have shown that layers are not necessary to describe the scattering and that features of the raft model, such as three-membered rings of tetrahedra, are not dominant configurations in glassy $GeSe_2$.

In this model, the similarity between the glass and the crystal is stressed, and the medium range order of the network structure is essentially two dimensional (layered) rather than three dimensional as in SiO_2.

Stochastic random network model (stochastic RNM):

A stochastic random network model was proposed for the structure of Ge_xSe_{1-x} glasses; $x \leq 0.33$. This model is based on the interpretation of Raman spectra from the view point of phonon localization. In this model, the glass structure is characterized by one parameter, P, that is related to the existing probability of the edge-sharing bonds between the tetrahedral $GeSe_4$ molecules relative to the corner-sharing bonds. An advantage of this model is that only one parameter, P, which depends only on the species of atoms forming the glass and not on x, can characterize the glass structure, and consistently explains the origin of the A_1 and the A_1^c peaks in the Raman spectra which have been a subject of controversy.

Topological model:

The topological model based on constraint theory is successful in accounting for the features observed in the property-composition dependence of several chalcogenide

glass systems.

In this model, the properties are discussed in terms of the mean coordination number, $\bar{r}$, which is indiscriminate to the species of the valence bond. Similarity of the molecular structure of the glass networks with that of the corresponding crystalline state is emphasized in this model, but however, reference to specific compositions or to individual families is not necessary.

1.6.6 Intermediate range order in g-Ge_xSe_{1-x}

Intermediate range order is evident in Ge_xSe_{1-x} glasses by the observation of a first sharp diffraction peak (FSDP) in the diffraction pattern at around 1 $Å^{-1}$. The FSDP's are commonly observed in glasses [87, 66, 6, 7]. They appear to have a universal property that they appear at a position Q_1 such that $Q_1 r_1 \sim 2.5$, where r_1 is the mean position of the nearest-neighbor peak in the PDF. The peaks are sharp (thus their name) with a full-width at half maximum, $\Delta Q_1 r_1 \sim 0.6$ [83]. These numbers indicate that a structural modulation exists in the glass with a wavelength of roughly $2\pi/Q_1 = 2.6 r_1$ and a correlation length of the order of $10 r_1$.

The structural origin of the FSDP's is still an active area of research. Theoretical suggestion by Phillips [24] for the FSDP in As_2Se_3 and $GeSe_2$ based on interconnected rafts of subunits of the crystalline analogs does not seem to be generic enough to explain the observation of FSDPs in a wide range of systems with different dimensionalities of the network [83]. On the other hand, random packing of rigid structural units with dimensions of the order of $2\pi/Q_1$ also gives rise a sharp peak at around the right position [60]. FSDP's also persist into the liquid phase as observed in $GeSe_2$ [83]. The FSDP is rapidly destroyed by the addition of silver impurities to Ge_xSe_{1-x} glasses; and it grows up out of a smooth background when tetrahedrally coordinated silicon [88], phosphorous [89] or germanium [85] is added to amorphous selenium. The presence of rigid tetrahedral units therefore appears to be important.

Taking a different track, a recent study by Elliott *et al.* [90, 91] on amorphous silicon and silica showed that the FSDP can be regarded as arising from scattering from atomic configurations equivalent to a single family of positionally-disordered local Bragg planes having the furthest separation. A more recent work on FSDP in Ge_xSe_{1-x} system [6, 7] claimed the observation of structural anomalies in FSDP parameters from which they characterized the existence of the intermediate phase.

Molecular dynamics (MD) [74, 92] studies suggest that the origin of the FSDP in $GeSe_2$ glass is principally due to the Ge-Ge correlations in the structure. This result is qualitatively supported by the partial-PDFs measured by Penfold and Salmon [80] where the FSDP was only significant in the Ge-Ge partial structure factor, $S_{Ge-Ge}(Q)$, though other predictions of the MD studies were less well borne out by the measured partials [80].

The FSDP is clearly an important indicator of intermediate range order in the glass structure. However, the lack of clear understanding of its structural origin limits its usefulness as a probe of structural changes that occur with doping, for example, associated with the IP.

1.6.7 Theoretical studies of short and intermediate range structure in g-Ge_xSe_{1-x}

Vashishta *et al.* [74, 92] using molecular dynamics simulations, investigated structural and dynamical correlations in molten and vitreous $GeSe_2$ with an effective interionic potential. They concluded that the short-range order is dominated by $Ge(Se_{1/2})_4$ tetrahedra and the Ge-Se, Se-Se, and Ge-Ge bond lengths are 2.35, 3.75, and 4.30 Å, respectively, with Ge-Ge and Ge-Se correlations between 4-8 Å being responsible for the FSDP observed in the static-structure factor. They explained the anomalous decrease in height of the FSDP on cooling by a frustration enhanced by increased number density.

An *ab initio* molecular-dynamics study of structural, vibrational, and electronic properties of glassy $GeSe_2$ [76] using a 216 atom model with normal mode analysis reveals a trend of localization in the band tails of the vibrational density of states (VDOS) as well as a significant change in the degree of localization for modes above approximately 15.5 meV. This analysis also shows that chemical disorder has a significant effect on the dynamics in g-$GeSe_2$.

Cobb *et al.* [75] using *ab initio* molecular dynamics study of liquid $GeSe_2$ showed many similarities between the topology of the liquid and the glass state, and suggested that the FSDPs of liquid and glassy $GeSe_2$ are results of the intermediate range order (IRO) imposed by fourfold and sixfold ring correlations. This study showed that an increase in Se bond length and bond-angle disorder significantly broadens the conduction band. The time-dependent behavior of the electronic eigenvalues is examined and transient events are observed in which an electronic state crosses the optical gap.

1.7 The goal of the Study

Based on the IP picture, two hypotheses can be inferred: Firstly, if the IP picture is correct, then samples in the IP region should have zero or minimum strain. Secondly, samples in the IP window should have maximum intermediate range order due to the proposed self-organization.

The goal of this study is to search for a structural response to the intermediate phase (IP) in the Ge_xSe_{1-x} glasses. In particular, our focuss is to examine the local structural changes in this system looking for evidence of the suggested IP region.

1.8 Layout of the dissertation

After the introduction describing the basics of glass networks as well as the onset of rigidity percolation and the discovery of IP, Chapter 2 describes the experimental probes used to test the hypotheses of the IP, the PDF and XAFS techniques. Chapter 3 describes the main results of a model-independent analysis of the composition dependence of the peaks in the PDF and of the FSDP. These should indicate underlying changes in structure that can be correlated with the intermediate phase. Chapter 4 presents a description of modeling of the data using crystalline analogs and results of molecular dynamics simulations on the Ge_xSe_{1-x} systems. Chapter 5 contains the summary and the main conclusions of the study.

Chapter 2

The atomic pair distribution function and X-ray absorption fine structure techniques

2.1 Introduction

One useful way of expressing the structural information is through the use of correlation functions that give information about local structural parameters such as inter-atomic correlations, coordination numbers and thermal displacements.

In this study we have used the atomic pair distribution function (PDF) and X-ray absorption fine structure (XAFS) experimental techniques to access structural information. These structural probes proved to be very successful in determining the local structure of materials. A brief account of these techniques, together with a mathematical description of the most relevant relations, will be given in this chapter.

2.2 Atomic pair distribution function (PDF)

Characterization of local structure of complex materials is important for a more complete understanding of their functionality. One of the most useful methods to do so is the atomic pair distribution function (PDF) technique, a total scattering technique that gives the local structural environment at the atomic scale.

The PDF analysis of powder diffraction data has been used for many years for studying materials with no long-range order, such as glasses and liquids. More recently, with the advent of high power X-ray and neutron sources and fast computing, it is making significant impact in the area of locally ordered and crystalline materials [21].

Traditionally, powerful crystallographic methods whereby Bragg-peaks are analyzed directly in reciprocal space provide extensive information about the underlying structure. However, as scientific interest shifts to more disordered crystals, and materials where the crystallinity is highly compromised, such as nanocrystals or crystallographically challenged materials, more of the important structural information is contained in the diffuse scattering component

The PDF technique, and closely related total-scattering methods, allow for both the Bragg and diffuse scattering to be analyzed together on equal terms, revealing the short and intermediate range order of the material.

The PDF function represents a Fourier transform of scattered X-ray or neutron total scattering patterns into direct space providing information related to the real-space arrangement of atom pairs [21]. In contrast to crystallographic methods, no presumption of periodicity is made, allowing non-periodic structures or aperiodic modifications to be studied. It is also a highly intuitive function since peaks in the PDF come directly from pairs of atoms in the solid and are positioned at r-values corresponding to inter-atomic distances. For example, a PDF peak that is shifted to lower-r values therefore directly implies that corresponding pair of atoms has a

shorter interatomic separation.

Below we briefly define various functions of interest and describe how they are measured. More details can be found in a recent published book on the subject, Underneath the Bragg Peaks: Structural Analysis of Complex Materials [21].

The experiments are typical X-ray and neutron powder diffraction measurements. They are usually carried out at synchrotron X-ray sources and pulsed neutron sources, rather than usual laboratory sources, since it is important to obtain the data over a wide range of momentum transfer, Q, for high accuracy and adequate real-space resolution of the PDF, and the laboratory sources can not meet this requirement. Since Q is given by, $Q = 4\pi \sin(\theta)/\lambda$ (for elastic scattering), and $Q > 30$ Å^{-1} is desirable, this implies that short-wavelength, high energy, X-rays or neutrons are required. X-rays of energy > 45 keV ($\lambda = 0.27$ Å) and up to 100 keV ($\lambda = 0.120$ Å) or more are typically used. Data from laboratory sources with Mo or Ag tubes can give acceptable results in some cases, but working at a synchrotron or spallation neutron source is preferred for the highest resolution measurements.

The atomic PDF, $G(r)$, is defined as:

$$G(r) = 4\pi r[\rho(r) - \rho_o] \tag{2.1}$$

where ρ_o is the average atomic number density, $\rho(r)$ is the atomic pair-density defined below, and r is a radial distance.

The function $G(r)$ is experimentally accessible and gives information about the number of atoms in a spherical shell of unit thickness at a distance r from a reference atom. It peaks at characteristic distances separating pairs of atoms, as shown schematically in Figure 2.1. It is related to the measured X-ray or neutron powder diffraction pattern through a Fourier transform:

$$G(r) = (2/\pi) \int_{Q=0}^{Q_{max}} Q[S(Q) - 1] \sin(Qr) dQ \tag{2.2}$$

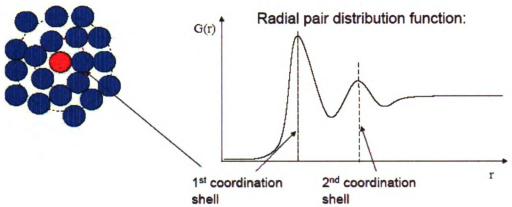

Figure 2.1: Illustration for the structural origin of features in the atomic pair distribution function, G(r), for an amorphous solid. Images in this figure are presented in color.

where $S(Q)$, the total scattering structure function, contains the measured intensities. An example of $S(Q)$ from fcc nickel, measured over a wide range of Q at beamline ID-1 of the Advanced Photon Source at Argonne National Laboratory, plotted as the reduced structure function, $Q[S(Q) - 1]$, and its Fourier transform, $G(r)$, are shown in Figure 2.2. The structure function is related to the coherent part of the total scattering intensity of the material, and is given by:

$$S(Q) = \frac{I^{coh}(Q) - \sum c_i |f_i(Q)|^2}{|\sum c_i f_i(Q)|^2} + 1 \tag{2.3}$$

where $I^{coh}(Q)$ is the measured scattering intensity from a powder sample that has been properly corrected for background and other experimental effects and normalized by the flux and the amount of the sample in the beam. Here, c_i and f_i are the atomic concentration and X-ray atomic form factor, respectively, for the atomic species of type i [93, 21].

In the case of neutron experiments the f_i's are replaced by Q-independent neutron scattering lengths, b, and the sums run over all isotopes and spin-states as well as over the atomic species. The choice between carrying out a neutron or X-ray experiment

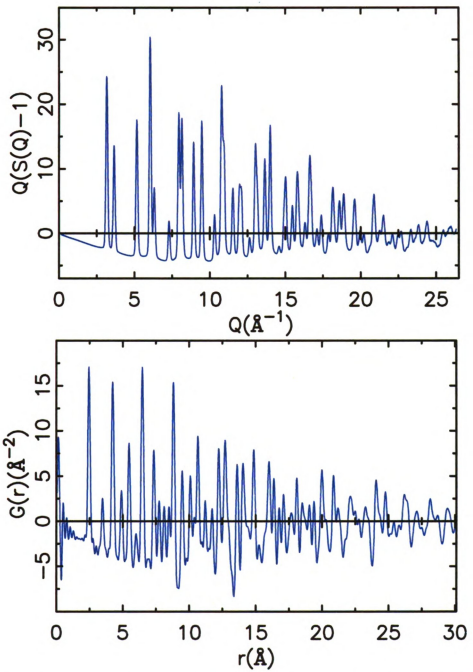

Figure 2.2: (a) The reduced structure function, $Q[S(Q) - 1]$, of crystalline Ni. (b) The PDF obtained by Fourier transforming the data shown in (a). Images in this figure are presented in color.

depends on the nature of the sample and nature of the information sought. The old paradigm that neutrons were intrinsically superior to X-rays for this type of measurement, as there is no neutron atomic form factor damping the intensity at high-Q, is no longer valid with the advent of extremely intense high energy X-ray synchrotron beams that can accurately account for the scattered intensity at very high Q values.

As can be seen from Equation 2.1 - 3.1, $G(r)$ is simply another representation of the diffraction data. However, exploring the diffraction data in real space has advantages especially in the case of materials with significant structural disorder.

The PDF reflects both the long-range atomic structure, manifested in the sharp Bragg peaks, and the local structural imperfections, manifested in the diffuse components of the diffraction pattern. This is because the total scattering, including Bragg peaks as well as diffuse scattering, contributes to the PDF. The modeling of the data also does not presume periodicity. Therefore, this technique is particularly useful for characterizing aperiodic distortions in crystals, analysis of nano structures and glasses.

The data are corrected for experimental effects such as sample absorption, multiple scattering, and normalized to get the structure function $S(Q)$. This process is described in detail elsewhere and various programs are available for carrying out these corrections. Improper corrections result in distortions to $S(Q)$ but these distortions vary much more slowly than the signal and are manifested as sharp peaks at very low-r in the PDF in a region (typically < 1.0 Å) where no structural information exists. A significant advantage of the PDF is that the useful structural data persist to very long r distances allowing models to be fitted over significant ranges. Providing they are not over-parameterized, these fits are highly resistant to random and systematic errors in the data and provide robust structural solutions.

Modeling the experimental PDF is straightforward because it can be calculated

directly from a structural model using the following equation:

$$G(r) + 4\pi r\rho_0 = \frac{1}{r}\sum_{\nu}\sum_{\mu}\frac{f(0)_\nu f(0)_\mu}{< f(0) >^2}\delta(r - r_{\nu\mu}) \tag{2.4}$$

Here the $f(0)$'s are the atomic form factors evaluated at $Q = 0$ that are, to a good approximation, given by the number of electrons for a given atomic species, Z. In the case of neutron diffraction the $f(0)$'s should be replaced by neutron scattering lengths, b_ν. In Equation 2.4, $r_{\nu\mu}$ is the distance separating the n^{th} and m^{th} atoms and the sums are over all the atoms in the sample.

For a material whose structure can be described by a small unit cell, which for the case of disordered crystals will be a supercell of the crystallographic cell, the first sum in Equation 2.4 runs over atoms in the cell and the second sum runs over all atoms up to whatever cutoff, r_{max}, may be of interest. This makes the problem computationally significantly more tractable. A number of regression programs are available. A program that uses least-squares in analogy with Rietveld refinement is PDFFIT2 [94].

Alternative methods include using a reverse Monte-Carlo type approach [95], where a residuals function is minimized using a simulated annealing algorithm, or using a potential based modeling scheme.

2.2.1 High-resolution X-ray PDF measurements

The technological advancements that allowed the PDF to be applied to crystalline materials was the development of spallation neutron sources. Unlike reactor sources, the spallation sources have high flux of epithermal neutrons with access to short wavelengths as well.

The real space resolution of the PDF is directly related to the range of Q over which data are measured; roughly speaking $\delta r = \pi/Q_{max}$ where Q_{max} is the maximum

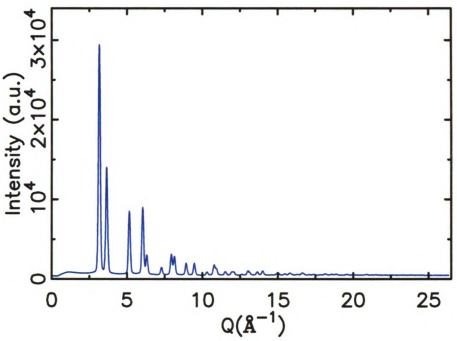

Figure 2.3: Raw intensity data from a sample of Ni measured using X-rays of $\lambda = 0.1235$ Å. The effect of the atomic form-factor in suppressing the intensity at high Q can be noticed. Images in this figure are presented in color.

Q-value. Since $Q = 4\pi \sin(\theta)/\lambda \leq 4\pi/\lambda$, to increase Q_{max} it is necessary to decrease λ.

Increasing the real-space resolution of X-ray measurements presents an additional challenge: the X-ray form-factor, $f(Q)$. The square of this is a measure of the structural-information containing coherent scattering from the material under study. The structure factor falls off sharply with increasing Q resulting in a weak signal at high diffracting angles. This is illustrated in Figure 2.3 that shows the raw scattered intensity from Ni. The overall drop-off in intensity follows $|f(Q)|^2$ with very little apparent structure in the scattering in the high-Q region.

2.2.2 Rapid acquisition PDF (RAPDF) measurements

The RAPDF data collection involves straightforward powder diffraction measurements. The main difficulties come from having to use high-energy X-rays, and having

a stable and low background setup allowing reliable quantitative measurement of weak diffuse intensities. This is described in detail in Egami and Billinge [21]. Neutron measurements are generally carried out at spallation sources that have desirable short-wavelength epithermal neutron fluxes. Data collection times vary, depending on the source, sample size and composition, from 20 minutes to 20 hours per data-set. Conventional X-ray measurement protocols use energy resolving solid-state detectors at a high-energy synchrotron where data collection typically takes 8 to 12 hours per data-set, depending on the sample properties, flux and required Q_{max}. Recently, a new approach to data collection making use of 2-D image plates as detectors and using very high energy X-rays ($\sim$ 100 keV) to compress the scattering data into a relatively narrow angular range.

RAPDF measurements are still under development and the data quality and range of applicability are being extended. However, there appears to be tremendous upside potential in using this approach, in part because of the fast data collection time, but also due to the fact that the measurement is static facilitating measurement on samples in confined geometries and special environments. Potential successful applications of RAPDF are time-resolved measurements of samples undergoing chemical reactions or under photo-excitation, for example, materials at high-temperatures and under pressure and extensive phase diagram studies.

Total scattering and PDF analysis of X-ray and neutron powder diffraction can be used to solve structural problems that cannot be addressed with traditional crystallographic methods. In this context the PDF analysis technique goes beyond crystallography and captures new structural information. In addition, this type of analysis can be applied in a complementary fashion to conventional crystallography to check the accuracy and validity of the crystallographically determined structure. Given that a crystallographic solution provides only an average structure, one cannot be absolutely sure whether the local structure is the same as the average one. If they are not, the

average structure is then an incorrect representation and does not capture the critical features that may be responsible for the physical properties of the material under study.

In summary, the PDF analysis represents an important tool for better understanding of structures at the atomic level, coupled with the wide accessibility of high energy X-ray synchrotrons and neutron sources as well as the short data collection time, using imaging plates, for example.

2.3 Structural information obtained from PDF method

Structural information obtained from PDF technique can be extracted through the analysis of the peaks in the PDF data. For well-defined crystals, the peaks are sharp and very well defined (series of delta functions). The difficulty arises when there are peaks that involve two or more mixed shells with very little separation between them as in glass where topological disorder exists.

Generally, extracting peak parameters (position, width and area) is obtained via fitting the peaks with Gaussian functions convoluted with Sinc functions to account for termination effects. Following is a description of these parameters:

PDF peak position:

Peak positions in the PDF data give the interatomic correlations in the structure. The position of the first PDF peak, if it is a single component, gives the bond length directly, which is very useful in understanding the local atomic structure [96]. The position of the first PDF peak is also sensitive to homogenous strain in the structure.

PDF peak width:

In real materials atoms are displaced from their perfect positions due to thermal motion and/or static displacements of the atoms. This gives rise to a distribution of

atom-atom distances, which causes the PDF peaks to be broadened. Generally, the width of a PDF peak gives information about thermal and/or static disorder. For the first PDF peak, if the number of nearest neighbors is constant, the integrated area under the peak is invariant, and so the peak height, extracted directly from the data, gives the inverse peak width. This often gives an accurate determination of the evolution of peak width with some experimental parameter such as temperature or composition. Three kinds of information may be obtained by studying the peak width:

- The width as a function of temperature yields information about the Debye temperature of a bond [97].
- The width as a function of atomic separation yields information about correlated atomic dynamics [98].
- The width as a function of doping gives information about doping-induced disorder.

PDF peak intensity

The integrated intensity under the PDF peak yields information about the number of atoms at a specific distance (the coordination number). This type of analysis is widely used in studies of glasses [99] and in partially crystalline samples [100].

2.3.1 PDF real space refinement

Conventional structure determination depends on the intensity and position of Bragg peaks. The most common method for such analysis is the Rietveld method [101]. A least-squares refinement between the calculated and observed intensities is performed until the best match with the measured profile is obtained. The calculated intensities

are obtained based on the crystal structure, thermal factors, diffraction optics, instrumental factors, lattice parameters and other specimen characteristics. The success of the method can be gauged by the publication of more than a thousand scientific papers yearly using it [102].

Considering only the Bragg peaks assumes perfect long range periodicity of the crystal. Such a presumption prevents the studying of non-periodic structures, or aperiodic modifications of crystalline materials. However many important materials are disordered and many of these materials owe their important properties to these deviations from the average structure. These deviations result in the occurrence of diffuse scattering, which contains information about two-body interactions and which is disregarded as a background in the Rietveld method. This shows the need for performing a similar refinement to the PDF data since it considers both kinds of scattering.

Full profile structural refinement of the PDF can be carried out using the program PDFfit2 [103]. In this method the model is defined in a small unit cell with atom positions specified in terms of fractional coordinates. The PDF is then calculated from the model structure and compared to the experimental PDF.

Following is a description of calculating the PDF data. Figure 2.4 illustrates successive shells of atoms that surround a given atom. (1) Assume that we have a sample that consists of N atoms at position r_n with respect to some origin. Place the origin of the space randomly at any atom. (2) Systematically find every other atom in the sample and measure its distance from the origin. (3) Each time we find an atom we place a unit of intensity at that position, r_m, on the axis of the radial distribution $R(r)$. When we have cycled over all of the atoms in the sample we move the origin to another atom and repeat the process, adding the intensity to the $R(r)$ function. The unit of intensity for each atom-pair is then multiplied by $b_m b_n / < b >^2$ where b_i is the scattering power of the i^{th} atom. Dividing by the number of atoms to

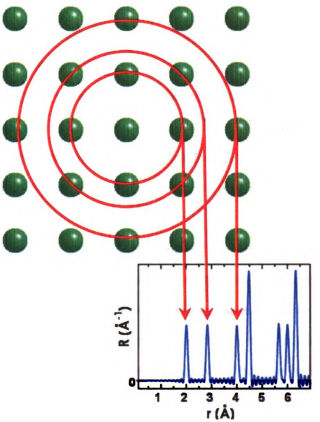

Figure 2.4: Schematic illustration of calculating the PDF function for a crystalline material. Images in this figure are presented in color.

keep $R(r)$ an intrinsic function. The $R(r)$ function is then given by Equation 2.5:

$$R(r) = \frac{1}{N} \sum_{mn} \frac{b_m b_n}{|b|^2} \delta(r - (r_n - r_m)) \tag{2.5}$$

the sum goes over all pairs of atoms m and n within the crystal, $\langle b \rangle$ is the average scattering power of the sample.

The calculated PDF is then fitted to the experimental one and the goodness of fit is determined by the parameter R_w which is computed according to the relation:

$$R_w = \sqrt{\frac{\sum_{i=1}^{N} w(r_i)[G_{obs}(r_i) - G_{calc}(r_i)]^2}{\sum_{i=1}^{N} w(r_i)[G_{obs}(r_i)]^2}} \tag{2.6}$$

Here w is the weighting factor, $w(r_i) = 1/\sigma_i^2$ where σ_i is the estimated standard deviation on the ith data-point at position r_i. The sum goes over all measured data points r_i in the experimental PDF.

Both PDF and Rietveld refinements use the same parameters. The main difference from Rietveld refinement is that PDF refinement allows for different r scaling, which enables one to study the local structure for different r-ranges [21]. The ability to refine the local structure yields information about disorder and short-range atomic correlations.

Because of the similarity between the Rietveld method and the PDF modeling a quantitative comparison between the resulting structures of both refinements may be made. This is an important first step in revealing the existence of local distortions beyond the average structure. It should be noted that the R_w factor used in PDF modeling is similar to that used in Rietveld analysis but the functions being fitted are significantly different. Hence, direct comparison of R_w from PDF and Rietveld analysis should not be made. R_w values are useful measures of the goodness-of-fit when comparing how different models fit to the same PDF data. For well-crystallized samples, PDF R_w values greater than 10%, are not uncommon. Obtaining an R_w value of less than 20%, for nano-crystalline structures is excellent.

2.4 X-ray absorption fine structure (XAFS)

X-ray Absorption Fine Structure (XAFS) spectroscopy has emerged as an incisive probe of the local structure around selected atomic species in solids, liquids, and molecular gases. The most important features of XAFS spectroscopy are its applicability to amorphous materials and its tunability (the ability to probe the environments of different elements in a sample by selecting the incident X-ray energy).

The importance of XAFS for the study of the structure of amorphous materials lies

in the fact that the theories describing it are equally valid for ordered or disordered structures, and perhaps more importantly that the local structure around a given atom may be ascertained simply by measuring the absorption near the edge of that particular atom.

There are three fundamental interactions of photons with matter. These are the photoelectric effect, the Compton scattering and the pair production. The characteristic energy for XAFS, due to the photoelectric process, ranges from 3 to 40 keV which is in the X-ray region. In this energy regime pair production is very energetically forbidden since it requires a photon energy of at least two times 511 keV to create both an electron and a positron. The probability for electron scattering is also very small since the X-ray wavelength is much larger than the effective electron cross section. A brief and simplified discussion of the basic ideas behind XAFS is presented below.

2.4.1 The XAFS phenomenon

The XAFS and the photoelectric processes involve the total absorption of an X-ray by an atom. The X-ray absorption coefficient of atoms is generally a decreasing function of energy (because of the increase in energy, high energy X-ray photons can easily pass through the sample), except at certain discrete energies (absorption edges) at which there are discontinuous dramatic increases in the absorption. In an atom, every atomic electron has an associated absorption edge.

When a photon of energy slightly higher than threshold is absorbed by an atom, a photo-electron is ejected. The photo-electron wave propagates outwards to infinity if the absorbing atom is isolated (e.g., an inert gas). In this case the absorption coefficient decreases smoothly from the absorption edge. However, if other atoms surround the absorbing atom, as in a gaseous molecule or in a condensed phase, the outgoing photo-electron wave will be back-scattered, and the back-scattered waves will inter-

fere with the outgoing waves as shown in Figure 2.5. The interference between the outgoing and scattered part of the photoelectron at the absorbing atom modifies the photoelectron. This interference changes the probability matrix elements for the absorption process itself, for the absorption of an X-ray and is responsible for the XAFS. Thus, as the X-ray photon energy is increased above threshold, the energy of the photo-electron also increases and consequently the electron wavelength decreases. Therefore, a maximum (minimum) in the absorption probability for the X-ray occurs when the wavelength of the photoelectron, determined by the X-ray energy, and the path of the photoelectron (the distance to and from the neighboring atoms) correspond to constructive (destructive) interference between the outgoing and scattered photoelectron waves at the absorbing atom, as shown in Figure 2.6. These periodic oscillations above the absorption edge are called "fine structure".

A precise measurement of absorption shows rich XAFS superposed onto the smooth energy dependence. This has been historically split into two regions. The first contains the fine structure from the absorbing edge to about 50 eV above the edge energy and is referred to as X-ray absorption near edge structure (XANES). The second region contains the fine structure from 50 eV to about 1000 eV above the edge energy and is referred to as extended X-ray absorption fine structure (EXAFS) as shown in Figure 2.7. which illustrates the two regions.

2.4.2 XANES versus EXAFS

The prevailing behavior of an X-ray absorption spectrum is the monotonic dependence of the X-ray absorption with the photon energy, interspersed with sharp edges. However, the detailed shape of the edge and of the X-ray absorption spectrum above it contains useful structural information.

The problem of calculating the outgoing waves in the strong field of adjacent atoms in a solid or liquid sample is notoriously difficult. It has to be tackled in full for slow

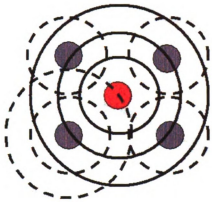

Figure 2.5: Photoelectron outgoing (solid circles) and backscattered (dashed circles) waves. The central red circle represents the X-ray absorbing atom. The dark gray circles represent neighboring atoms. Images in this figure are presented in color.

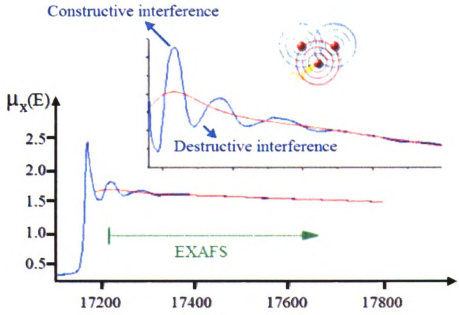

Figure 2.6: Schematics of the EXAFS process illustrating the origin of EXAFS oscillations due to the interference of outgoing and backscattered photoelectron wave. The red curve represents a smooth background spline. Images in this figure are presented in color.

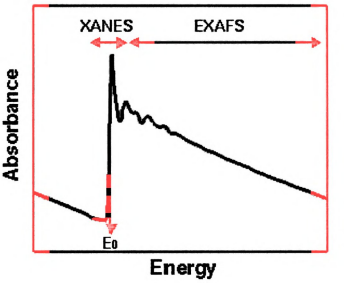

Figure 2.7: Typical XAFS spectrum showing the XANES and EXAFS regions. E_0 is the edge energy. Images in this figure are presented in color.

photoelectrons, i.e., when the incident photon energy is just above the threshold (the XANES). The XANES region contains valuable information on chemical bonds and the site symmetry. Further out from the absorption edge, the problem of the photoelectron wave is considerably simplified. With the shorter photoelectron wavelength, the adjacent atoms scatter the photoelectrons as point obstacles, each contributing a tiny wavelet. Each atom scatterer contributes a harmonic oscillatory mode; together they form a complex quasi-periodic EXAFS signal. Fourier analysis of this signal resolves the harmonic components into a probability versus distance diagram. Its peaks occur at rather accurate values of the neighbor atom distances. In addition, the coordination number and chemical species of the neighbor atoms, as well as the statistical spread of their distances due to thermal motion or static disorder can be, in principle, deduced from the size and shape of the peaks.

2.4.3 Basic principles involved in XAFS

XAFS happens due to the photoelectric effect, which is described quantum mechanically as the probability for the absorption of an X-ray by an atom. This probability, as contained in Fermi's golden rule, is proportional to the square of the matrix element between the initial and the final states. The initial state consists of the electron in an atomic core. The final state consists of a core hole and a photoelectron in the conduction band, free from the absorbing atom.

The initial state is well localized at the absorbing atom, so it is only necessary to determine the final state of the photoelectron at the absorbing atom. According to quantum theory this photoelectron can be visualized as a spherical wave centered at the excited atom and propagating away with wavelength given by the DeBroglie relation:

$$\lambda = \frac{h}{p} \tag{2.7}$$

where h is Plank's constant and p is the momentum of the photoelectron. This momentum is related to the photoelectron's kinetic energy which equals the difference between the X-ray energy (E) and the electron binding energy (E_o) and is written as:

$$p = \sqrt{2m_e(h\nu - E_0)} \tag{2.8}$$

where m_e is the mass of the photoelectron, and ν is the frequency of the X-ray photon.

In the dipole approximation, where the wavelength of the photon is large compared with the spatial extent of the excited core state, the absorption can be treated to first order in perturbation theory and Fermi's golden rule then yields for the absorption coefficient, μ_x:

$$\mu_x = 4N_o\pi^2e^2\frac{\omega}{c}|\langle f|z|i\rangle|^2\rho(E^F) \tag{2.9}$$

where $|i\rangle$ and $|f\rangle$ are the initial core state and the final photo-electron wave function,

respectively, ω is the X-ray angular frequency, $\rho(E^F)$ is the density of final states, N_o is the number of atoms of one type in the sample, e is the charge on the electron and c is the speed of light.

Since in the dipole approximation, the photon field can be regarded as being spatially uniform, it can be approximated by a scalar potential proportional to the distance (z) if the X-ray polarization is in the z-direction. Hence, only the matrix element of the density of states in Equation 2.9 could give rise to oscillatory behavior of μ_x. For photon energies well above threshold, $\rho(E^F)$ varies monotonically since it is well described by the free electron value. Therefore, the matrix element alone must be responsible for the oscillatory behavior, and this is because the final state wave function $|f\rangle$ is made up of contributions from both the outgoing wave and the back-scattered wave, and interference between the two modulates the matrix element and hence μ_x.

The phase of the interference is determined by the wavelength and the path of the photoelectron. The amplitude of the interference is determined, in part, by the type of neighboring atoms since they determine how strongly the photoelectron will be scattered. For the purpose of our study, emphasis is made on the EXAFS part of the XAFS spectrum, because it is the part that reveals information about bond lengths, coordination numbers and Debye-Waller factors.

2.4.4 The EXAFS equation

The EXAFS equation is the basis for theoretical models and the resulting fit parameters are used to extract structural information. The EXAFS equation for single and multiple scattering events can be generalized from the EXAFS equation for a photoelectron which has scattered from a single atom.

The oscillatory part of the measured absorption coefficient ($\mu_x(E)$) is normalized by the smooth atomic absorption background (μ_0), resulting in the EXAFS signal

($\chi(E)$), as shown in the following relation:

$$\chi(E) = \frac{\mu_x(E) - \mu_o(E)}{\mu_o(E_0)} \tag{2.10}$$

where E is the photo-electron energy which, however, is not known exactly since the threshold energy (i.e., the zero of energy E_o) can not be positioned precisely; instead it is left as an adjustable parameter. The background absorption μ_o is also difficult to measure, and it is usually fitted by means of a polynomial. Based on this model, the formula describing the EXAFS can be calculated and in atomic units is given by [104]:

$$\chi(k) = -\sum_j S_0^2 \frac{N_j}{R_j^2} \frac{|f_j(\pi)|}{k} \exp(-\frac{2R_j}{\lambda_e}) \exp(-2\sigma_j^2 k^2) \sin(2kR_j + 2\delta(k) + \eta_j(k)) \tag{2.11}$$

where a sum over all paths, j, is taken, each with degeneracy N_j. $2R_j$ is the length of the scattering path. The other parameters are identified in the discussion below.

The magnitude of the EXAFS is proportional to N_j, inversely proportional to R_j^2 (since both the outgoing and back-scattered waves are assumed to be spherical, decreasing in amplitude as $1/R$) and proportional to the back-scattered amplitude $|f_j(\pi)|$ from the atoms in the jth shell. The amplitude is attenuated because of the finite mean free path λ_e of the electrons in the material and by the Debye-Waller term involving root mean square (r.m.s.) displacements σ_j (static or thermal) about the equilibrium position.

The amplitude of the EXAFS is sinusoidally modulated by a function involving the phase shift of the electron; the additional phase shift $\delta(k)$ and $\eta(k)$ arise because the photo-electron is emitted and back-scattered, respectively from atomic potentials. The wavenumber of the photo-electron, k, is given by the relation:

$$k(\mathring{A}^{-1}) = \frac{2\pi}{\lambda} = \left(\frac{2m_e(E - E_o)}{\hbar^2}\right)^{\frac{1}{2}} \tag{2.12}$$

where m_e and E_o are the mass and threshold energy for the photoelectron respectively, and E is the energy of the X-ray photon. Note that k here is half the scattering wavevector Q in Equation 2.13.

$$Q(\mathring{A}^{-1}) = \frac{4\pi \sin(\theta)}{\lambda} \tag{2.13}$$

Thus, from Equation 2.11 we expect the EXAFS to be a complicated oscillatory function, each path contributing a sinusoidal of a different period which mix together.

An additional amplitude reduction factor (S_0^2) for $\chi(k)$ is introduced in the EXAFS equation to describe effects of multi-electron excitations accompanying the photo-effect in the inner shell. Note, however, that it is only the first few shells which contribute strongly because of the limited mean free path of the photo-electrons, and the large widths, σ, of higher-lying shells.

The radial structure function, $\chi(r)$, is then obtained via Fourier transformation of the k^n-weighted EXAFS spectra, $k^n\chi(k)$, and is given by Equation 2.14:

$$\chi(r) = \frac{1}{(2\pi)^{1/2}} \int_{k_{min}}^{k_{max}} \chi(k) M(k) k^n \exp(2ikr) dk \tag{2.14}$$

Here $M(k)$ is a window function, and n represents the k-weight used.

2.4.5 EXAFS measurements

In an EXAFS experiment, the energy of the incident X-ray is increased from approximately 200 eV below to 1000 eV above the absorption edge energy of interest. This changes the wavelength of the photoelectron (as given by Equation 2.12) and results in the oscillations in the measured absorption coefficient (μ_x).

Two sources of broad-band X-rays may be used. Either by the *Brehmstrahlung* spectrum from conventional X-ray tubes or the radiation emitted by electron synchrotrons. Synchrotron radiation offers the advantage of $\sim 10^4$ increase in photon

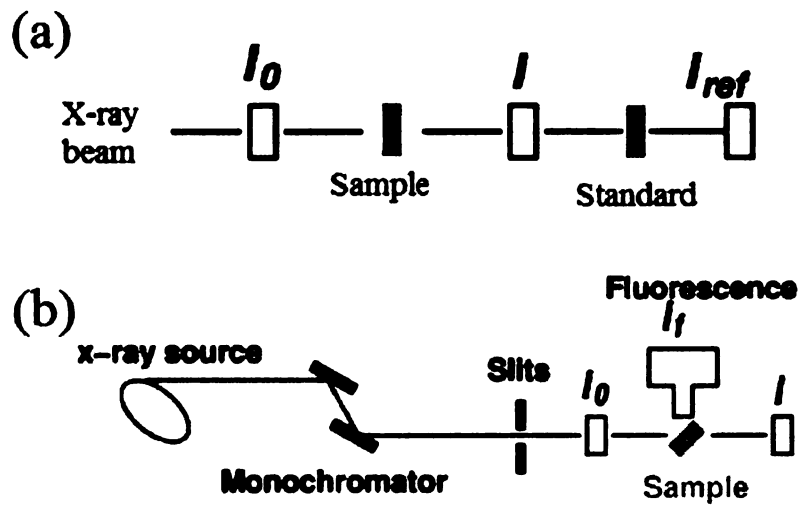

Figure 2.8: XAFS experiment setup. (a) Transmission mode and (b) fluorescence mode. Images in this figure are presented in color.

flux and concomitant reduction in counting time, in both cases the beam is monochromatized by a crystal.

EXAFS is conventionally measured using transmission and/or fluorescence geometry. Typical XAFS transmission and fluorescence modes are shown in Figure 2.8. For the transmission mode, the incident (I_o) and transmitted (I_t) X-ray intensities passing through a thin foil of the sample of thickness d are measured as a function of photon energy. The transmitted and incident intensities are related to the absorption coefficient, μ_x, by the relation:

$$I_t = I_o \exp(-\mu_x d) \tag{2.15}$$

For dilute samples, the desired EXAFS is swamped by background intensity in a transmission mode, and the more sensitive technique of fluorescence detection must be employed. In the fluorescence mode, the K-shell hole left by the photo-electron is filled by a p-electron from the L-shell, emitting an X-ray photon of characteristic energy less than that of the exciting X-rays. Thus by tuning to the fluorescent

wavelength, only those atoms which are excited are monitored, with a consequent dramatic increase in sensitivity.

With the availability of tunable, high flux, and high energy synchrotron radiation sources, monochromatic X-ray beams with energy resolution ($\Delta E/E$) of 10^{-4} are easily obtainable, allowing measurements of high quality absorption spectra in a short time. These developments made XAFS spectroscopy one of the most widely used methods for structural research of materials and make it the most unique probe for identifying the local structure around atoms of a selected type in the sample.

2.4.6 Structural information obtained from EXAFS experiments

In EXAFS, number and species of neighbor atoms, their distance from the selected atom and the thermal or structural disorder of their positions can be determined from the oscillatory part of the absorption coefficient above a major absorption edge. The analysis can be applied to crystalline, nano-structural or amorphous materials, liquids and molecular gases. EXAFS is often the only practical way to study the arrangement of atoms in materials without long range order, where traditional diffraction techniques cannot be used.

The structural information available from EXAFS experiments can be seen by reference to Equation 2.11. In principle, the coordination number, N_j, the interatomic spacing, R_j, and the mean square deviation, σ_j^2, for each shell, j, of atoms surrounding the absorbing atom is obtainable.

Two methods of extracting the structural information are commonly employed. One approach is to treat all the structural parameters in Equation 2.11 as adjustable variables and to vary these (perhaps with crystalline values as input parameters) until the best fit between the calculated EXAFS spectrum and the experimental data is achieved. The major difficulty in this, as in most analyses of EXAFS, is what

values to take for the phase shifts δ and η. There are two possible remedies to this problem: either values may be calculated theoretically by solving Schrodinger's equation taking account of the perturbations to be potential caused by neighboring atoms, or else comparison is made with a standard, usually a crystal, for which the structure is known and by fitting parameters to the EXAFS data of the standard, values of δ and η are thereby obtained.

The second method of analysis of EXAFS data is by taking the Fourier transform (FT) of the measured EXAFS structure as shown in Equation 2.16:

$$\phi(r) = \frac{1}{(2\pi)^{1/2}} \int_{k_{min}}^{k_{max}} \chi(k) M(k) k^n \exp(2ikr) dk \tag{2.16}$$

where $M(k)$ is a window function, and n can be 1, 2 or 3, the larger weighting the data more at high k-values.

Via Fourier transform, contributions of individual shells of atoms (first, second and perhaps higher shells) are separated visually in real space, as can be seen from Figure 2.9 which represents the EXAFS $\chi(k)$ for crystalline Ge together with its Fourier transform. The peaks in the magnitude of the FT spectra appear at the corresponding positions R_j. To obtain quantitative information on the local environment, such as number and species of neighboring atoms in a given shell, their distance from the absorbing atom and their thermal or structural disorder, the peak of interest is analyzed.

The theoretical basis of the EXAFS method is firmly established and the necessary electron scattering data known with sufficient accuracy so that *ab initio* modeling of the structure is possible.

Several computer programs have been developed for the quantitative analysis, which take into account single scattering as well as multiple scattering contributions to the EXAFS signal. In either method of getting structural information (fitting of the model function to the measured EXAFS spectra in k-space or by Fourier transform to

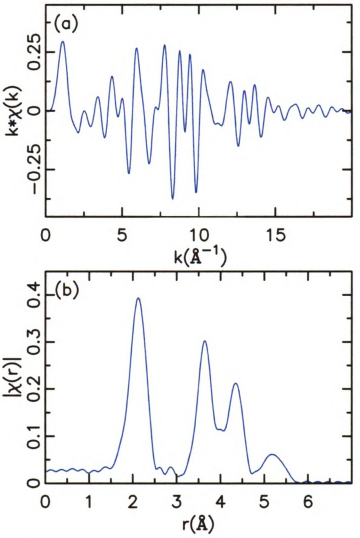

Figure 2.9: (a) The EXAFS $\chi(k)$ and (b) the magnitude of the Fourier transform of (a) for crystalline Ge. Images in this figure are presented in color.

R-space), interatomic distances can be determined with very high accuracy (typical uncertainties below 1%), while for the number of neighbors and the corresponding Debye-Waller factor lower precision ($\sim$ 10%) is only attainable, due to correlations between the two parameters.

2.4.7 Joint EXAFS and PDF refinement of complex materials

EXAFS and PDF are powerful experimental techniques for determining structural information about materials. Despite the fact that both of them can be applied to crystalline, nano-structural or amorphous materials, liquids and molecular gases, each has some strengths and weaknesses that are clearly differentiated one from the other.

On one hand, the PDF method has had some success in characterizing the local structure of challenging complex materials. PDF theory is conceptually easy to understand and to apply. PDF data covers a large spatial range, which makes a good tool for measuring physical effects that manifest in the medium-range order, such as charge density waves. However, in unfavorable cases the PDF method cannot distinguish unambiguously between different structural models.

On the other hand, the chemical specificity of EXAFS makes it an excellent tool for determining the immediate environment of the absorbing atom. However, due to the fast decay of the EXAFS signal, such an analysis can seldom be extended past the second or third coordination shells.

It is certain that there are many problems that are better solved by one technique over the other. One challenge in determining when to use EXAFS or PDF, or both in parallel, is comparing the results of an EXAFS and PDF analysis on an equal basis.

One way towards better understanding of the structure of materials is to combine local structural information from different local structural methods. Complex structural refinement using both XAFS and PDF is a promising approach to achieve this as two methods complement each other. On one hand, combination of these two complementary local structural methods in a quantitative and self-consistent manner holds the promise of getting much more accurate local structural information and is expected to result in better understanding of the local structure of materials. On the other hand, refining both XAFS and PDF data for challenging complex materials

will accurately distinguish between two or more structural models that can not be achieved by a single method.

Chapter 3

Search for a structural response to the IP in Ge_xSe_{1-x} glasses

3.1 Introduction

According to constraint counting theory [18, 24], a network is considered floppy if the average number of constraints per atom (n_c) is less than 3 (the number of degrees of freedom for an atom in 3 dimensions), as in the case of twofold coordinated single bond chain networks. On the other hand, the network is rigid if n_c is greater than 3 as in networks consisting only of tetrahedral units (such as SiO_2). Thus, a progressive addition of cross-linking elements (such as Si, As or Ge) to a starting chain network (such as S or Se) will result in a progressive increase of its connectivity (mean coordination number ($\bar{r}$)). At $\bar{r} = 2.4$, rigidity percolation occurs where the network changes from floppy to rigid structure [5]. A number of experiments [26, 28, 27] show responses consistent with a percolation transition.

Canonical systems for studying this phenomenon are the chalcogenide glasses. Surprisingly, based on thermodynamic and spectroscopic measurements, they appear to exhibit two transitions instead of one [3]. The region between these transitions has been called the intermediate phase (IP) [3, 4]. The original theoretical work assumed

that the network was generic and the connectivity random [5]. It was therefore suggested [1] that the IP phase is a region of finite width in composition where the network could self organize in such a way that maintains a rigid but unstressed state. However, it has proved very difficult to establish this result experimentally.

If the interpretation of IP is correct, one expects to see a direct structural response to the transitions. It should be apparent in structural parameters sensitive to strain, since it is a transition from unstressed to stressed. Self-organization in the IP may also be apparent by observing the appearance of intermediate range structural order, for example, changes in the first sharp diffraction peak (FSDP).

To test the hypothesis of the IP, a careful study has been made of a series of carefully prepared glasses in the Ge_xSe_{1-x} system. This system can be made as glasses over a wide composition range ($x = 0.0$ to 0.42 of germanium) [50, 51, 53, 52] allowing the systematic composition dependence to be studied. Here is described a detailed systematic composition-dependent study of structural parameters in Ge_xSe_{1-x} glasses covering a wide range of composition around the IP ($0.15 \leq x \leq 0.40$) with a narrow spacing between points. X-ray diffraction data were measured using advanced high energy synchrotron radiation with complementary X-ray absorption fine structure measurements.

The diffraction data have been processed to obtain the total scattering structure function, $S(Q)$, and the reduced pair distribution function (PDF). The width of the first peak in the PDF, which contains information about strain in the system, has been extracted as a function of composition, x. Information about intermediate range order (IRO) has also been extracted from the FSDP versus x. A study by Sharma *et al.* [7] indicates that the position and width of the FSDP in this system has an anomaly in the region of the IP, from which they ruled out the existence of three well-resolved phases consistent with the IP. This result was not reproduced in our work. In fact, there is no clear evidence for a structural responses from the PDF and XAFS data

that correlate with the expected appearance of the IP or the rigidity transition.

3.2 Experimental procedures and data reduction

Bulk glass samples of Ge_xSe_{1-x} where x = 0.15, 0.16, 0.18, 0.19, 0.20, 0.21, 0.22, 0.23, 0.24, 0.26, 0.28, 0.30, 0.33, 0.34, 0.35, 0.36, 0.38 and 0.40 were prepared by a conventional melt-quenching process. The starting ingredients (99.9999% Ge and Se) were vacuum-sealed (5 x 10^{-7} Torr) in quartz tubes, heated to 950 °C for 4 days or more, and thereafter melt temperatures were slowly lowered to 50 °C above the liquidus (the temperature above which a substance is completely liquid), where they equilibrated for 6 hours before quenching in cold water. Samples were allowed to age for 3 weeks before quartz tubes were opened, and glass transitions were examined in modulated differential scanning calorimetric measurements. A scan rate of 3 °C/minute and a modulation rate of 1 °C/100 seconds was used to record scans. The frequency corrected non-reversing enthalpies, $\Delta H_{nr}(x)$, for the samples were measured, and showed a square-well like global minimum as shown in Figure 3.1. As in earlier studies [48], there is a clear minimum in $\Delta H_{nr}(x)$ which is used as an indicator for the IP and showing the quality of the samples.

The glasses were gently crushed into fine powder, formed into discs 5 mm in diameter and 1 mm thick, sealed between thin Kapton foils and subjected to X-ray diffraction experiments. This approach ensured that the samples in the beam were of uniform geometry.

The X-ray diffraction measurements were carried out using the rapid acquisition PDF (RAPDF) technique [105] at the MUCAT 6-ID-D beam line at the Advanced Photon Source (APS), Argonne National Laboratory at room temperature. A bent double-Laue Si <111> crystal [106] was used to monochromatize the white beam and deliver an intense flux of X-ray photons of energy 87.005 keV (λ = 0.14250 Å). A large area image plate detector (Mar345) was placed 108 mm behind the sample.

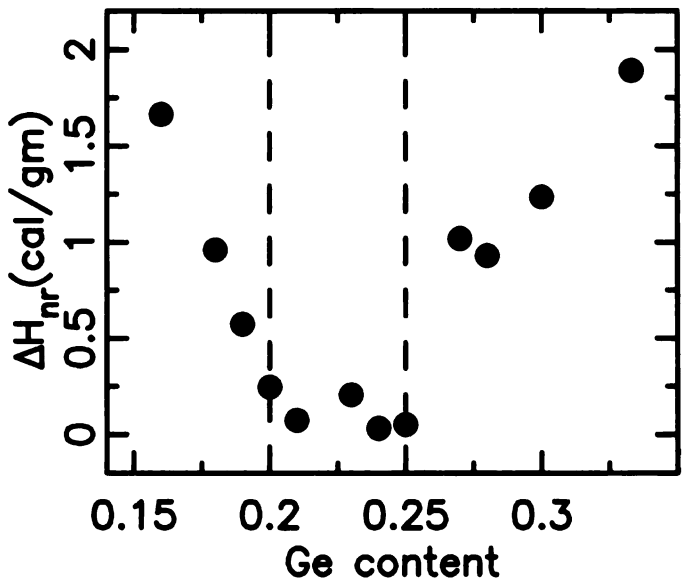

Figure 3.1: The non-reversing heat flow (ΔH_{nr}) versus composition for the samples used in this study. The results indicate that these samples exhibit the experimental signature associated with the presence of an IP [3], which can be located from this plot in the region between 0.20<x<0.25. The two vertical dashed lines are plotted at the boundaries of the predicted IP.

The sample-detector distance was calibrated using a silicon standard of known lattice parameter. The use of X-rays of such high energy allows the access of higher wave vectors and helps reduce several unwanted experimental effects such as absorption and multiple scattering. Five diffraction scans, with an irradiation time of 100 seconds each, were conducted for each sample and the diffracted intensities were averaged to improve the statistical accuracy and reduce any systematic effects due to instabilities in the experimental set up. Integration of the MAR images was performed using program Fit2D [107]. Data reduction to obtain the structure function, $S(Q)$, and the PDF, $G(r)$, were performed using program PDFgetX2 [108].

The structure function, $S(Q)$, is related to the coherent part of the total diffracted intensity of the material, and is given by:

$$S(Q) = \frac{I^{coh}(Q) - \sum c_i |f_i(Q)|^2}{|\sum c_i f_i(Q)|^2} + 1 \tag{3.1}$$

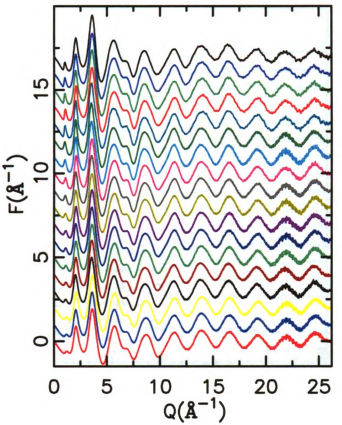

Figure 3.2: The measured structure functions, $S(Q)$'s, for the Ge_xSe_{1-x} glasses. Data are offset up for clarity. The compositions (x) are, from the bottom to the top curves, 0.15, 0.16, 0.18, 0.19, 0.20, 0.21, 0.22, 0.23, 0.24, 0.26, 0.28, 0.30, 0.33, 0.34, 0.35, 0.36, 0.38 and 0.40. Images in this figure are presented in color.

where $I^{coh}(Q)$ is the measured scattering intensity from a powder sample that has been properly corrected for background and other experimental effects and normalized by the flux and number of atoms in the sample. Here, c_i and f_i are the atomic concentration and X-ray atomic form factor, respectively, for the atomic species of type i [93, 21]. Figure 3.2 shows the measured reduced structure functions, $F(Q) = Q[S(Q) - 1]$, for all of the studied Ge_xSe_{1-x} glasses.

The overall similarity of the $F(Q)$ curves indicates that there is no appreciable unaccounted background, or systematic effects interfering with the signal from the sample. The overall shapes of the curves (including the oscillations about zero at high-Q) are remarkably similar suggesting that the data reduction and normalization

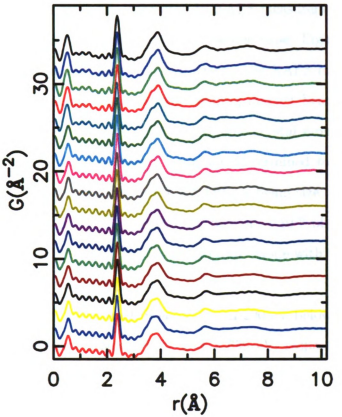

Figure 3.3: Experimental atomic PDF $G(r)$'s for Ge_xSe_{1-x} glasses. Data are offset up for clarity. The compositions (x) are, from the bottom to the top curves, 0.15, 0.16, 0.18, 0.19, 0.20, 0.21, 0.22, 0.23, 0.24, 0.26, 0.28, 0.30, 0.33, 0.34, 0.35, 0.36, 0.38 and 0.40. Images in this figure are presented in color.

procedures are effective. The curves have not been smoothed and the low level of noise, even at high-Q, is apparent.

The data were then Fourier transformed to obtain the reduced pair distribution function, $G(r)$, and these are shown in Figure 3.3. From the experimental PDF's shown in Figure 3.3, there are a relatively small number of well defined peaks which is a signature of such glassy materials since the stronger the disorder in a noncrystalline material the weaker the correlations between the positions of the atoms in it and, hence, the lower the number of well-defined peaks in the PDF. The peaks occurring at short distances (below the first PDF peak at 2.37 Å) are unphysical, and are due to imperfections in the data reduction.

The Ge_xSe_{1-x} glasses were also subjected to XAFS measurements. Finely powdered glasses were uniformly spread on adhesive scotch tape. Eight to twelve layers were stacked to get optimized signal-to-noise levels. The XAFS measurements were performed in the transmission mode at the bending magnet beamline, 5BM-D, at the Advanced Photon Source, using Si <111> double crystal monochromator. The energy resolution of the monochromatic beam was determined to be $\sim$ 1.5 eV for near-edge structure and about 3 eV for the EXAFS. A beam size of about 0.3 $\times$ 0.5 mm^2 was used resulting in an incident photon flux of $\sim 10^{10}$ photons per second. The synchrotron storage ring operated in the "top-up" mode with the electron beam current kept around 100 mA.

The monochromator was scanned in energy from 200 eV below to 800 eV above the Ge and Se K-absorption edges (11103 and 12659 eV, respectively). The incident, I_0, and the transmitted, I_t, X-ray intensities were measured simultaneously at room temperature using ion-chambers located before and after the sample. The ion-chambers were filled with a mixture of nitrogen and argon gases. Data were collected with a step size of 0.20 eV in the respective edge regions. The energy calibrations were performed using Ge and Se foils between the I_t and a third, I_{ref}, ion chambers, respectively.

The EXAFS data reduction was performed using standard procedures using the Athena software package [109, 110]. The measured absorption spectrum below the pre-edge region was fit to a straight line. The Autobk algorithm [111] implemented in Athena was used to determine the background and normalize the X-ray absorption, $\mu(E)$, data. This algorithm uses a cut off parameter (Rbkg) to define the Fourier frequency below which the signal is dominated by the background and above which the signal contains the data. Thus Autobk attempts to remove those Fourier components that are due to the background while leaving those that contain the data.

Edge-step normalization was also done by the Athena software where the difference

between the raw data, $\mu(E)$, and the background, $\mu_0(E)$, is divided by an estimation of the edge step value ($\mu_0(E_0)$) resulting in the EXAFS signal, $\chi(E)$, defined by the following relation:

$$\chi(E) = \frac{\mu(E) - \mu_0(E)}{\mu_0(E_0)} \tag{3.2}$$

The normalized $\chi(E)$ spectra were then converted to $\chi(k)$ in k-space, $k = (8\pi^2 m(E - E_0)/h^2)^{1/2}$. The resulting $\chi(k)$ functions were then weighted with k^2 to account for the damping of oscillations with increasing k. Based on this, the formula describing the EXAFS (Equation 2.11) was calculated.

Figure 3.4 shows the XAFS $k^2\chi(k)$ for all the studied samples at both Ge and Se edges. The pure oscillations in $k^2\chi(k)$ are consistent with such glassy material, in which they result in a single well-defined shell after being Fourier transformed.

The radial structure function, $\chi(r)$, was then obtained via Fourier transformation (Equation 2.14) of the normalized k^2-weighted EXAFS spectra, $k^2\chi(k)$, using a k range of 2.5 to 15.9 Å^{-1} for both Ge and Se edges. Here $M(k)$ is a window function, and n represents the k-weight used, which was 2. The Fourier transforms of the measured EXAFS signals at both Ge and Se edges are shown in Figure 3.5. The Fourier transforms at both Ge and Se k-edges clearly show a well-defined first shell, as expected, but the second and higher order shells appear to be observable at a level only slightly above the noise level. This decreased information in the higher shells reflects the fact that the considerable disorder (which manifests itself in large Debye-Waller factors) plays a dominant role in these glasses.

EXAFS data fitting was performed using the Artemis program [110]. A single scattering path was used to fit each bond type. For Ge-edge data, Ge-Se and Ge-Ge single scattering paths were used, and for the Se-edge data, Se-Ge and Se-Se single scattering paths were used.

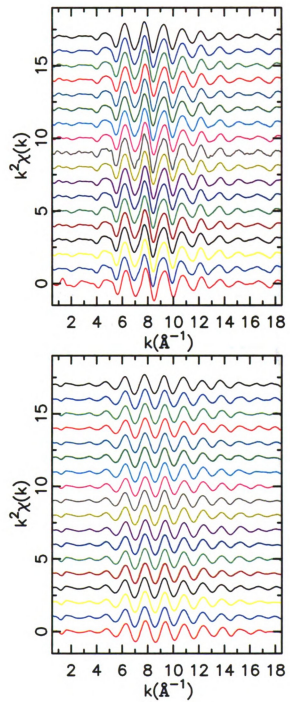

Figure 3.4: k^2 weighted XAFS signal ($k^2\chi(k)$) for Ge_xSe_{1-x} glasses at (a) Ge-edge and (b) Se-edge. Data are shifted up for clarity. The compositions (x) are, from the bottom to the top curves, 0.15, 0.16, 0.18, 0.19, 0.20, 0.21, 0.22, 0.23, 0.24, 0.26, 0.28, 0.30, 0.33, 0.34, 0.35, 0.36, 0.38 and 0.40. Images in this figure are presented in color.

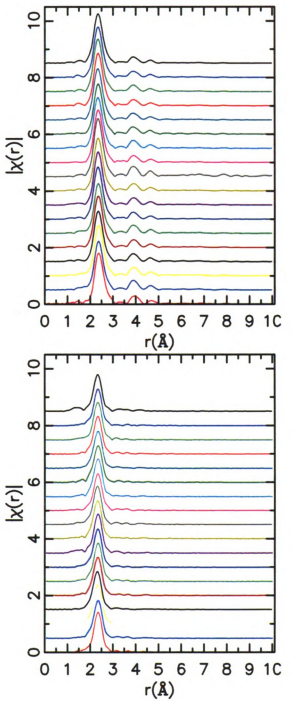

Figure 3.5: Magnitude of the Fourier transform of k^2 weighted XAFS signals ($k^2\chi(k)$) for Ge_xSe_{1-x} glasses at (a) Ge-edge and (b) Se-edge. Data are shifted up for clarity. The compositions (x) are, from the bottom to the top curves, 0.15, 0.16, 0.18, 0.19, 0.20, 0.21, 0.22, 0.23, 0.24, 0.26, 0.28, 0.30, 0.33, 0.34, 0.35, 0.36, 0.38 and 0.40. Images in this figure are presented in color.

3.3 Results and discussion

The transition from floppy to rigid in Ge_xSe_{1-x} glasses should be accompanied by the appearance of strain in the overconstrained region above the transition. One explanation for the appearance of the intermediate phase is that, due to self-organization of the network, there is a region of finite composition width that is rigid but unstrained [1]. A measurement of the residual strain-state of the glass could give direct support to this picture. In the PDF a homogeneous strain can be detected as a shift in bond-length (PDF peak position) and inhomogeneous strain as a broadening of the bond-length distribution. The first peak in the PDF yields direct information about bond-stretching in the nearest neighbor bonds. Changes in peak positions and widths of higher order peaks yield information about bond-bending relaxations in covalent systems [112, 113]. Things are complicated in the glass because of peak overlap between peaks of different structural origin. Nonetheless it is still interesting to look for evidence of strain in these glasses. Initially, the nearest neighbor PDF peak is considered.

The first PDF peak in Ge_xSe_{1-x} glasses is a multi-component peak. It has three unresolved contributions: $r_{Se-Se} = 2.32$ Å, $r_{Ge-Se} = 2.37$ Å, $r_{Ge-Ge} = 2.42$ Å. The relative intensities of these are determined by the Ge content of the glass. At the low Ge contents of interest, one expects the peak to be dominated by Se-Se and Ge-Se correlations. The contribution of each of these sub peaks can be estimated by using one of two distinctly different models that are consistent with the '8-N' coordination rule.

The first one is a random covalent network model (RCN) [19], in which the world random is used to indicate that the distribution of bond-types is statistical and hence completely determined by the respective local coordinations and the fractional concentrations of each atom type. This approach to the bonding neglects factors such as the relative bond energies. The random covalent bonding description includes Ge-Ge,

Table 3.1: Single bond energy in the Ge_xSe_{1-x} system.

Bond Type	Bond Energy (kcal/mole)
Ge-Ge	37.6
Se-Se	44.0
Ge-Se	49.1

Ge-Se and Se-Se bonds at all compositions other than $x = 0$ and $x = 1$.

The alternative model for bond statistics is called the chemically ordered network (CON) model [114]. This model emphasizes the relative bond energies and favored the hetro-polar (Ge-Se) bonds than the homo-polar (Se-Se or Ge-Ge) bonds. The single bond energies in the Ge_xSe_{1-x} system are given in Table 3.1. The CON model contains a chemically ordered compound phase at a composition $x_c = N_{Se}/(N_{Ge} + N_{Se})$, where N_i is the coordination number of atom of type i. This phase is the stoichiometric composition ($GeSe_2$), $x = 0.33$ in this case, which, according to this model, contains only Ge-Se bonds. For compositions below the stoichiometric composition, the alloys contain Se-Se and Ge-Se bonds; whereas for compositions defined above the stoichiometric composition, the alloys contain Ge-Se and Ge-Ge bonds.

Figure 3.6 shows the bond counting statistics for the Ge_xSe_{1-x} system based on the RCN and CON models.

Although neither model is perfectly correct, the existence of a compound phase at a-$GeSe_2$ suggests that chemical ordering is preferred in the Ge_xSe_{1-x} glasses at least over the range of bulk-glass formation (x = 0.0 to 0.42 of germanium). This is supported by other structural measurements, for example PDFs obtained by X-ray diffraction [115, 116] and by structural interpretations of IR and Raman vibrational spectroscopy [117, 114], where below x = 1/3, the fraction of Ge-Ge homopolar bonds is less than few percent [79]. We therefore chose to concentrate on the CON model.

In the region of interest, for compositions in the vicinity of the IP, the CON model predicts only Ge-Se and Se-Se bonds to be present. The width of the bond

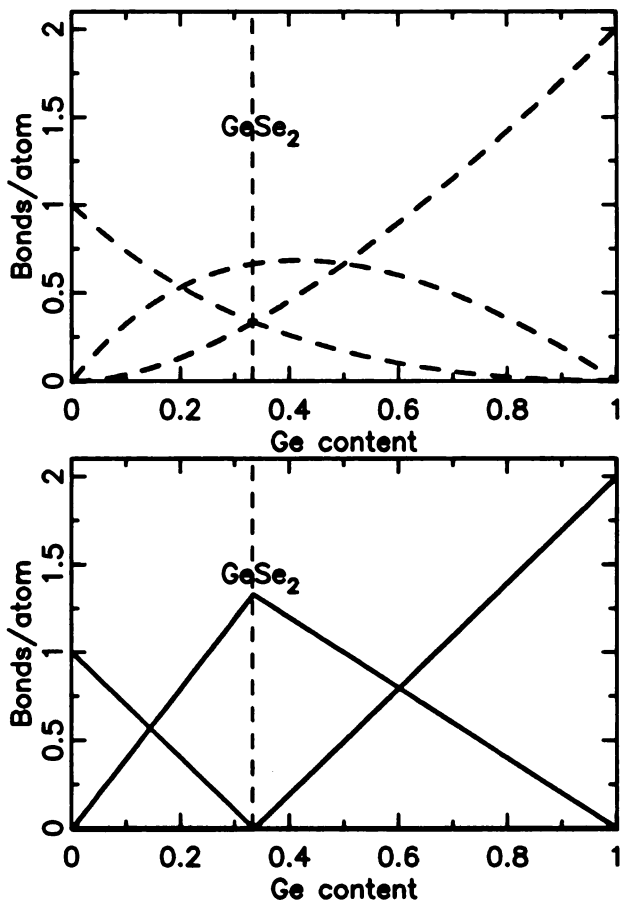

Figure 3.6: Bond counting statistics for the Ge_xSe_{1-x} networks based on the random covalent network (RCN) model (upper panel), and the chemically ordered network (CON) model (lower panel). Red, Blue and Green curves represent Se-Se, Ge-Se and Ge-Ge bonds, respectively. The dashed vertical line is plotted at the stoichiometric composition ($GeSe_2$). Images in this figure are presented in color.

distributions is expected to be ~ 0.1 Å at room temperature, whereas the separation of the centroids of the two peaks is expected to be $r_{Ge-Se} - r_{Se-Se} = 0.05$ Å. The intrinsic width of the peaks is greater than the separation of the peaks and the sub-components are not resolved. Indeed, the intrinsic width of the sub-components dominates the observed PDF peak width and results in a peak that is quite Gaussian in its intrinsic shape, convoluted with the Sinc function coming from the finite termination of the data in Q-space, as observed in Figure 3.3.

In analyzing the first PDF peak, the parameters have been extracted from both

experimental and simulated data. In particular, it has been fit with a single Gaussian convoluted with a Sinc function to simulate the finite Q_{max} of the measurement.

The width of the first PDF peak contains the desired information about peak broadening due to strain effects, but because it contains more than one unresolved bond, its position, width and intensity also evolve due to the changing composition of the network. To separate these effects, the first PDF peak is simulated taking into account the changing chemistry. The simulation was done in two ways. In the first way, the expected behavior of the average position and width was studied versus doping assuming that the peak consists of three components whose positions are fixed at the above values and where the widths of the three components are not changing with doping. In the second way, the simulation was repeated by changing the positions and widths of the sub-peaks as obtained from the XAFS results. In both ways, the intensity of each sub-peak is governed by the expected concentration from the CON model, scaled by the appropriate product of the scattering amplitudes of the components. A simulated PDF peak was produced from these models by summing together the three sub-components. Both ways are relevant, as the first way uses fixed positions and widths, it represents the unstrained model, while the second way considers the evolution of the experimental positions and width as obtained from EXAFS measurements, and hence tracks the changes in positions and widths due to both chemical and strain effects. Similar to the experimental data, the resulting simulated peak for each composition was then fit using one Gaussian convoluted with a Sinc function. Figure 3.7 shows a representative plot of the fits to the experimental and simulated first PDF peak.

The average positions of the first PDF peak, for both experimental and simulated data, for all the samples, are shown in Figure 3.8. The red circles give the expected behavior obtained from the simulated data. This shows the behavior with no change in intrinsic peak width due to strain, but only changes due to the composition of the

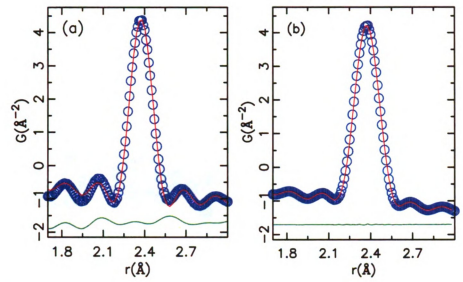

Figure 3.7: Representative plot showing the quality of the fit to the first PDF peak of the Gaussian peak (convoluted with a sinc function) in the $GeSe_2$ glass. (a) The fit to the experimental data and (b) the fit to the simulated data (see text for details). Experimental or simulated data (blue circles), the fit (red curves). Offset below are the differences (green curves). Images in this figure are presented in color.

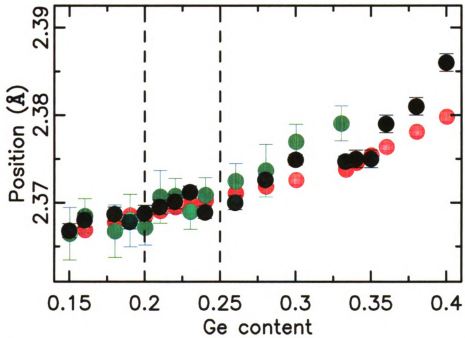

Figure 3.8: Position of the first PDF peak as obtained from fitting the experimental PDF data with a single Gaussian (black) and from fitting a simulated PDF peak based on the XAFS results (green) and CON model (red). The vertical dashed lines are plotted at the IP boundaries. See text for details. Images in this figure are presented in color.

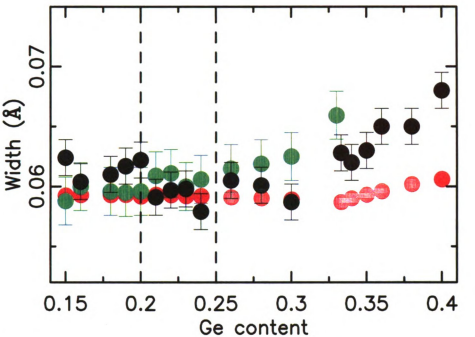

Figure 3.9: Width of the first PDF peak as obtained from fitting the experimental PDF data with a single Gaussian (black) and from fitting a simulated PDF peak based on the XAFS results (green) and CON model (red). The vertical dashed lines are plotted at the IP boundaries. See text for details. Images in this figure are presented in color.

peak based on the chemically ordered model and assuming that r_{Ge-Se} and r_{Se-Se} retain their nominal values.

Figure 3.8 shows that the average experimental position of the first PDF peak (black symbols) agrees well with the expected one from the CON model (red symbols), with positive deviation that starts to appear after the stoichiometric composition. No special features are seen in the position of the first PDF peak that may correlate with the IP.

Of greater interest is to look for evidence of inhomogeneous strain from a peak broadening. The experimental as well as the simulated width of the first PDF peak are plotted versus composition in Figure 3.9. There is no apparent change in width, or even in the slope of the width versus doping, associated with the IP. Any change in the bond-stretching strain of the sample on passing through the IP must be below

the sensitivity of the measurement. This is not surprising as covalent bonds are rather stiff, and the sensitivity of the measurement is limited because of the multi-component nature of the first PDF peak. The experimental width of the first PDF peak is consistent with the simulated one (based on the CON model, where the change is just due to change in composition of the sample), and shows no correlations with the IP.

The EXAFS data also contain information about the atomic pair distributions of the near-neighbor peaks. This information can be extracted by modeling the data. The relative advantage of EXAFS here is that it allows the positions and widths of the individual sub-components of the first PDF peak to be separated. The disadvantage is that parameter correlations arise because of the number of variable parameters in the fits, which can result in biased results. This was mitigated here because data from both the Se and Ge edges were collected. In the composition range below the stoichiometric composition, $GeSe_2$, the number of Ge-Ge homopolar bonds is no more than a few percent [79]. The analysis of the EXAFS data was concentrated to this region, neglecting the contribution coming from any Ge-Ge component. The nearest neighbor coordination shell of the Ge edge data therefore consists of only Ge-Se bonds, whereas that of the Se edge contains Se-Ge and Se-Se. These edges were fit together, as described below, which allowed us to extract parameters from these edges with greater reliability.

In the analysis of the XAFS data, a single scattering path was used for each bond type. At the Ge-edge, and according to the CON model, only Ge-Se bonds exist, for $x \leq 0.33$, and so, a single scattering path of Ge tetrahedrally coordinated with Se atoms was used. For the Se-edge data, two single scattering paths were used to account for Se-Se and Se-Ge bonds. Ge-Se and Se-Ge path parameters were set to satisfy the bond consistency relation and the '8-N' rule and sharing the path length and Debye-Waller factors.

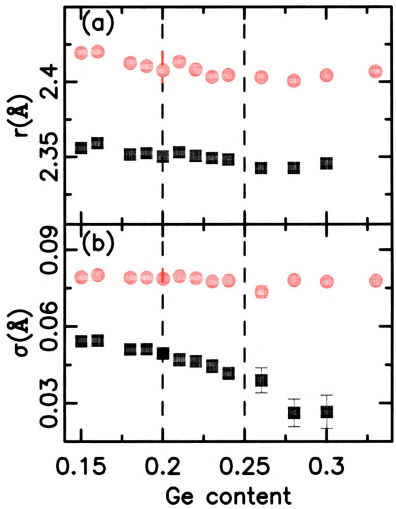

Figure 3.10: Refined bond lengths (a) and Debye-Waller factors (b) versus x (Ge content). Red circles represent Ge-Se bonds and blue squares represent Se-Se bonds. The vertical dashed lines are plotted at the lower and upper boundaries of the IP. Images in this figure are presented in color.

Figure 3.10 shows the refined bond lengths and Debye-Waller factors (σ) for both Ge-Se and Se-Se bonds as a function of Ge content. The bond lengths of the sub-peaks are close to their nominal values and almost fixed (within their uncertainties) with Ge content. On the other hand, the Debye-Waller factors for Ge-Se bond are also fixed (within their uncertainties) with Ge content, but the Se-Se Debye-Waller factors are decreasing with Ge content, probably due to the decreasing number of Se-Se bonds when Ge content is increased. No clear correlations exist with the IP,

such as a pronounced minimum in the IP compositions range (0.20 to 0.25 in Ge content).

It is desirable to compare the results of the EXAFS with those from the PDF to check for consistency. They cannot be compared directly because the PDF data represent total PDF, and hence information about the partial PDFs (Se-Se, Ge-Se and Ge-Ge) can not be extracted individually. EXAFS data at both Ge and Se edges contain structural information about the sub-components (positions and widths) and so it is therefore possible to simulate the first peak in the diffraction PDFs directly from the EXAFS data, by summing together the properly weighted sub-component peaks. This was done and the resulting curves were fit using the same protocol that was used to fit the PDF data and the simulated peak from the CON model. The results are shown as the green symbols in Figure 3.8. There is excellent quantitative agreement with both the diffraction PDF and the result simulated from the chemically ordered network (CON) model. It is interesting to note that the EXAFS results indicate that both the Se-Se and Ge-Se bonds are getting slightly shorter with increasing Ge content, but the position of the compound peak shifts to higher-r with doping. This is a result of the fact that the contribution of the longer Ge-Se bond is increasing with x.

Bond-bending forces in covalent materials are much weaker than bond-stretch [113] and so one would expect to see a larger response of second and higher neighbor peaks in the PDF due to a change in the stress state of the sample at the IP. Unfortunately the second neighbor peak has multiple contributions and interpretation of changes in peak width, shape and position is somewhat ambiguous. This peak does exhibit significant changes with composition that can be seen in Figure 3.11. These are thought to relate to an evolution of the underlying network connectivity, such as the appearance of edge-sharing $GeSe_4$ tetrahedra [118] as well as effects due to benign compositional changes. This peak is mainly composed of Se-Se correlations within

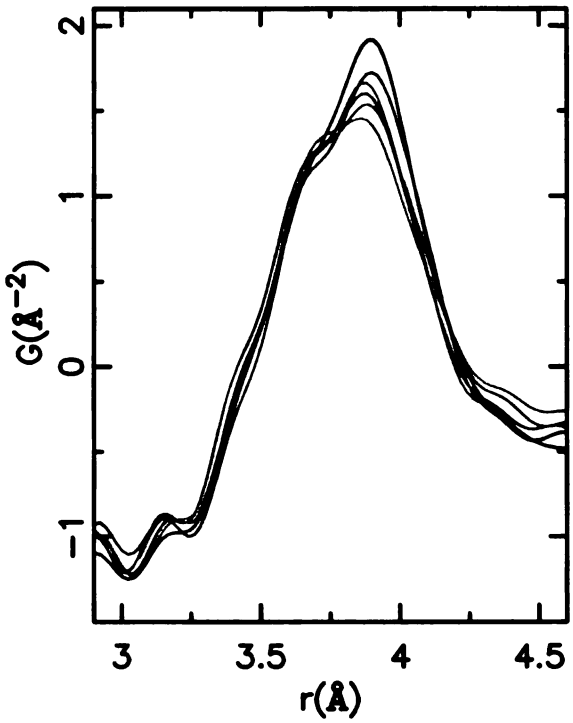

Figure 3.11: Second PDF peak plotted on an expanded scale for a selection of the samples ($x = 0.15$ (red), $x = 0.20$ (dark red), $x = 0.23$ (dark magenta), $x = 0.26$ (gray), $x = 0.33$ (dark green), $x = 0.40$ (black). The peak contains multiple contributions and so changes shape and position with changing composition. Images in this figure are presented in color.

each tetrahedron and a left-side shoulder that is due to Ge-Ge correlations among corner and edge shared tetrahedra.

Another important structural indicator that is sensitive to intermediate range order in a glass is the first sharp diffraction peak (FSDP) [87, 119]. A response of this peak to the IP may indicate an underlying structural ordering consistent with the idea that the finite width of the IP is a response of the system to remove strain by introducing structural ordering.

Figure 3.12 shows the $S(Q)$s for some selected samples in the FSDP region. A dramatic change in the height and position of the FSDP is clearly observed, in agreement with earlier studies [119]. As evident in Figure 3.12, the FSDP is a strongly varying function of composition, rising out of a smoothly varying background when

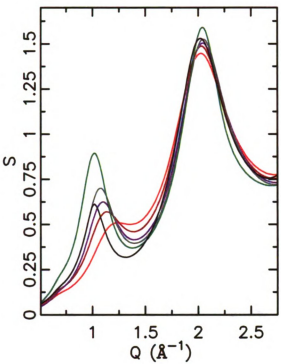

Figure 3.12: Low-Q part of the structure function ($S(Q)$) for selected samples ($x = 0.15$ (red), $x = 0.20$ (dark red), $x = 0.23$ (dark magenta), $x = 0.26$ (gray), $x = 0.33$ (dark green), and $x = 0.40$ (black)). With increasing Ge content the first sharp diffraction peak develops in height and shifts to the left until the stoichiometric composition ($x = 0.33$). At higher Ge content it decreases in height. Images in this figure are presented in color.

Ge is added to selenium glass.

Model independent peak fitting was performed on the $S(Q)$ spectra to extract the FSDP parameters (position, area, width and height). Due to the uncertainty of the FSDP profile shape, the $S(Q)$ spectra were analyzed using different fitting protocols. These include pure Gaussian, pure Lorentzian and pseudo-Voigt which is a linear combination of Gaussian and Lorentzian line-shapes.

The fits included the first three peaks in the $S(Q)$ curves, with the fitting range extending from 0.5 Å^{-1} to 4.5 Å^{-1}. All the fitting protocols used a zero background. Figure 3.13 shows the quality of the fits obtained using the above fitting protocols for two representative sample compositions. The fits of pure Gaussians to all three peaks were qualitatively worse than the others and so they are not considered further.

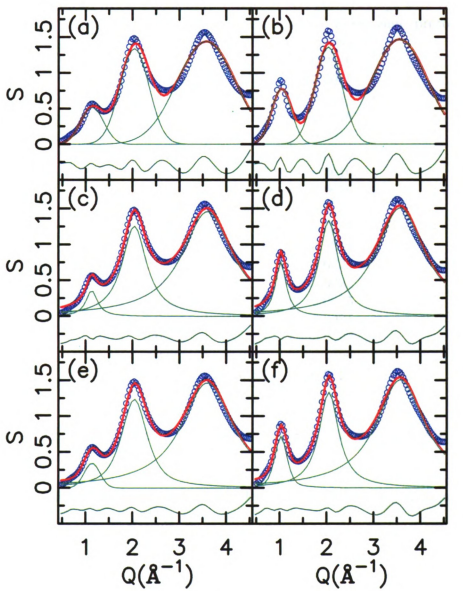

Figure 3.13: Plots indicating the quality of the fits to $S(Q)$ data for two representative samples ($Ge_{0.20}Se_{0.80}$ in the left panels and $GeSe_2$ in the right panels) using three different fitting protocols. (a)-(b) Pure Gaussians, (c)-(d) pure Lorentzians and (e)-(f) pseudo-Voigt type functions. Experimental data are shown as circles, red solid curves represent the fits with the difference curves offset below. Images in this figure are presented in color.

Table 3.2: χ^2 values for the different fitting protocols to the Q-space data. The different fitting protocols are: Pure Lorentzian (protocol 1), pseudo-Voigt but with the FSDP constrained to be Gaussian (protocol 2) and pseudo-Voigt with the FSDP line shape being allowed to change between Gaussian and Lorentzian (protocol 3).

x	Protocol 1	Protocol 2	Protocol 3
0.15	0.0019	0.0019	0.0016
0.16	0.0018	0.0018	0.0015
0.18	0.0018	0.0017	0.0015
0.19	0.0019	0.0016	0.0016
0.20	0.0020	0.0016	0.0017
0.21	0.0017	0.0016	0.0015
0.22	0.0019	0.0017	0.0016
0.23	0.0019	0.0016	0.0016
0.24	0.0018	0.0016	0.0015
0.26	0.0019	0.0016	0.0017
0.28	0.0022	0.0018	0.0019
0.30	0.0023	0.0018	0.0021
0.33	0.0023	0.0018	0.0022
0.34	0.0042	0.0025	0.0035
0.35	0.0038	0.0021	0.0031
0.36	0.0034	0.0027	0.0027
0.38	0.0032	0.0026	0.0026
0.40	0.0032	0.0027	0.0027

Table 3.2 lists the χ^2-values of the different fitting protocols to the $S(Q)$ data for all the Ge_xSe_{1-x} glasses:

Figure 3.14 shows the results of the FSDP parameters as obtained from the different fitting protocols. The results from more than one fitting protocol are included to assess the variability of the results. Greater confidence can be ascribed to results that are reproduced between the different fitting protocols. The results of the pure Gaussian fits were not included as these fits did not reproduce the FSDP profile shape.

In each plot in Figure 3.14 the green symbols are the results for Lorentzian line-shapes and the red and blue are the results of pseudo-Voigt fits. In the case of the red symbols the FSDP was constrained to be purely Gaussian but the mixing coefficients in the pseudo-Voigt function were allowed to float for the other peaks, allowing the peak to have a line-shape intermediate between Gaussian and Lorentzian. In the

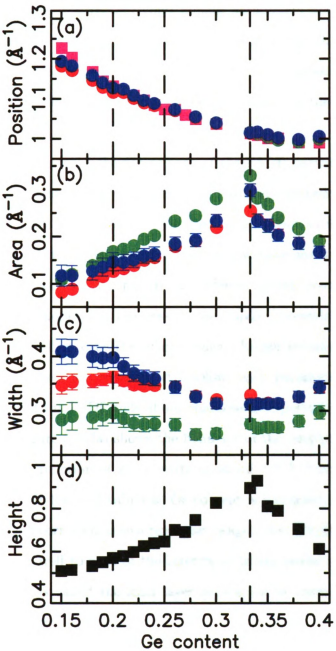

Figure 3.14: Fit parameters for the FSDP in binary Ge_xSe_{1-x} glasses as a function of x: (a) position, (b) area, (c) width and (d) height. The different colors represent the different fitting protocols. (green) Pure Lorentzian fits, (red) pseudo-Voigt but with the FSDP constrained to be Gaussian, and (blue) pseudo-Voigt with the FSDP line shape being allowed to change between Gaussian and Lorentzian as part of the fit. Square symbols in (a) and (d) represent the position and height of the FSDP, respectively, obtained directly from the experimental data. The dashed vertical lines are plotted at the proposed boundary of the IP as well as at the stoichiometric composition ($GeSe_2$). Images in this figure are presented in color.

case of the blue symbols, the pseudo-Voigt mixing parameters were allowed to vary for all three peaks that were fit. The square symbols in Figure 3.14(a) and (d) are fitting independent parameters for the (a) position and (d) peak height that were obtained directly from the data as the x and y coordinates of the maximum of the FSDP feature. They track the fits rather well.

Qualitatively, the general behavior of each of the FSDP parameters are well reproduced by the different fitting protocols. The positions obtained by the different protocols are within the estimated uncertainties. This is not so for the width and integrated areas. The differences are largest in the low Ge-content region where the FSDP is quite indistinct. In this region the different fitting protocols give results with slightly different slopes. In the case of the purely Lorentzian line-shapes the widths and areas are offset over the whole range, though detailed x-dependencies on the refined parameters are reproduced. Below, each parameter is described in detail. The position of the FSDP tells about characteristic periodicities in the structure in real space. Figure 3.14(a) shows the behavior of the position of the FSDP in Ge_xSe_{1-x} glasses as a function of x. It starts at about 1.2 $Å^{-1}$ for low Ge content, and then shifts towards lower-Q values as Ge content is increased, reaching 1.0 Å at $x = 0.4$. This position corresponds to a real space length, $d = (2\pi/Q_{FSDP}) = 5.2$ - 6.3 Å, which corresponds well to that of the inter-layer Bragg peaks seen in crystalline $GeSe_2$ [120], where d is called the inter-layer separation or cluster radius [9, 120]. This is in agreement with more elaborate wavelet analysis of the FSDP by Elliot *et al.* [121].

No anomalies in the FSDP position were detected for samples in the vicinity of the IP or at its upper boundary ($x = 0.25$).

The area of the FSDP shows a maximum at the stoichiometric composition ($x = 0.33$) as shown in Figure 3.14(b). This is also apparent in the height of the FSDP maximum obtained directly from the data without fitting. These two parameters track

each other because the width of the FSDP is nearly constant (Figure 3.14(c)). This suggests that the proportion of the intermediate range order contributing to this periodicity in the structure is increasing with Ge content up to the stoichiometric composition, and then it decreases.

Molecular dynamics [74, 92] calculations indicate the importance of Ge-Ge correlations to this feature in the scattering. It is therefore not a surprise that the peak intensity scales with the concentration of Ge in the sample being studied.

The dramatic change of the FSDP height as well as area at $x = 0.33$, even though the Ge content is still increasing, is attributed to the change in the role of Ge atoms in the network. Below $x = 0.33$, Ge atoms work as network formers [119], so adding Ge will result in a progressive increase in the correlations contributing to this peak, which are thought to come from well-defined separations of $GeSe_4$ tetrahedra. On the contrary, above $x = 0.33$, Ge atoms work as network modifiers (entities that do not participate in forming the network structure) [119]. This will weaken the ordering of the $GeSe_4$ tetrahedra and hence decrease the intensity of this peak. This effect is also seen when silver ions are added to g-$GeSe_2$ [83], where they modify the $GeSe_2$ covalent network by bonding to the Se atoms, with the effect of breaking up the larger ring structure and hence reducing the intensity of the FSDP. The addition of silver also leads to a softening of the vibrational spectrum.

The IP is thought to be rigid but unstrained where the stress-free state was proposed to be due to self-organization in the network. If this is correct, then one might expect that the range of the intermediate range order (IRO) is maximal in the IP window. This would be characterized by a minimum in the FSDP peak width. Actually the FSDP width is quite composition independent from the fits. There is a broad, weak minimum that has a global minimum at the $GeSe_2$ composition. This suggests that the correlation length of the intermediate range order coming from the stacking of $GeSe_4$ tetrahedra is greatest for the stoichiometric composition and then decreases

at higher compositions. There is a suggestion of a change in the slope of FSDP width versus x associated with the rigid to floppy transition at $x = 0.20$. This is certainly a suggestion that the range of the IRO starts to increase only after the rigidity of the network percolates. Apart from offsets due to parameter correlations, this kink in the curve is reproduced in all the fitting protocols, which builds confidence in its correctness. However, the FSDP-width continues to decrease (the range of the IRO continues to increase) with increasing Ge content above the upper limit of the IP, so there is no convincing evidence that this is a signature for the IP.

The study of the FSDP as an observable for the IP has been pursued in two earlier studies [6, 7]. The study by Sharma *et al.* [7] of the FSDP in Ge_xSe_{1-x} suggested that there were three well resolved structural phases consistent with the IP. They found a plateau-like behavior of the inverse of the FSDP position in the region of the IP. This is not reproduced in the current work. Wang *et al.* [6] concluded that around the stiffness threshold, the area of the FSDP has a plateau-like gradual decrease with x followed by a rapid decrease at $x \leq 0.18$. There is also no evidence for this behavior in the present study.

Despite that our results of the FSDP parameters reproduced the general trends in Sharma's and Wang's results, as the FSDP position shifts to lower Q-values as Ge content is increased and its area is increased till $x = 0.33$. However, our results show a smooth and monotonic behavior of the different FSDP parameters when crossing the IP region. No special features (as constancy of the FSDP area in the IP region (as in Wang's paper) and constancy of the FSDP position (as in Sharma's paper) happen in FSDP parameters due to the predicted IP, which makes it impossible to rule out three well-resolved phases from the FSDP.

We think that this discrepancy is due to the fact that the FSDP at the low-Ge content is a relatively week shoulder that rises out just above the background level, which makes it difficult to predict its profile shape for certainty. Hence, fitting it

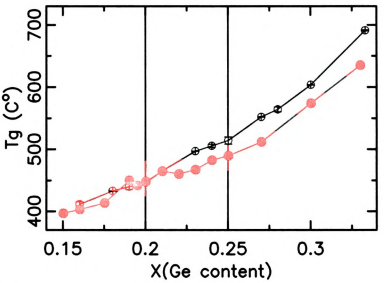

Figure 3.15: Comparison between T_g values of the studied samples (blue circles) and Sharma samples [7] (red circles). Images in this figure are presented in color.

with just one fitting protocol (even if that protocol fitted it perfectly) might bias the results.

Another valid reason of this discrepancy is due to the differences in the methodology of samples preparation. Despite that our samples and those of Sharma and Wang were prepared by conventional melt-quenching technique, any differences in the thermal history of the samples may affect the local structure and hence the intermediate range order deduced from the FSDP. The glass structure is extremely sensitive to the method of preparation. Figure 3.15 compares the glass transition temperature of our samples with those of Sharma. It is clear that there is some discrepancy between the two values which might be due to the differences in samples preparation.

However, great care was taken in establishing the quality of our samples and characterizing the behavior through the non-reversing heat flow measurements. Multiple fitting protocols are also reported, that establish the reproducibility and uncertainty of the results. This is also the only study that combines PDF and EXAFS data to address this issue. The EXAFS and PDF data are in good agreement, which gives us confidence that the current results are reliable.

3.4 Summary and conclusions

A careful composition-dependent study of the structure of Ge_xSe_{1-x} glasses, through the composition range associated with the intermediate phase and using high energy X-ray total scattering studies coupled with EXAFS measurements at the Ge and Se edges, do not yield strong evidence for a structural origin for the IP. Structural parameters associated with strain in the sample (pair distribution function peak widths from the X-ray and EXAFS data) and intermediate range order (deduced from the first sharp diffraction peak in $S(Q)$) all evolve smoothly with composition and no discontinuities or breaks in slope are evidently associated with the boundaries of the IP.

Chapter 4

Structural modeling of Ge_xSe_{1-x} glasses around the IP

4.1 Introduction

In Chapter 3 we have seen that both PDF and XAFS can give information about the microscopic structure of amorphous Ge_xSe_{1-x} glasses. However, this information is limited almost entirely to the first two coordination shells; i.e., the bond lengths and angles of nearest neighbor atoms comprising the basic structural units (such as $GeSe_4$ tetrahedra in $GeSe_2$) can be determined but the relative disposition of such units cannot be ascertained with certainty. For the case of PDFs derived from scattering experiments on mono-atomic systems, for example, the problem lies in the fact that peaks other than the first and second cannot be uniquely associated with a particular interatomic correlation, but are made up from a variety of contributions from higher-lying shells (see Figure 2.1). Matters are complicated considerably for multicomponent materials, especially when the constituent atoms are close in their scattering factors as in Ge_xSe_{1-x} glasses where Ge and Se have atomic numbers of 32 and 34, respectively. In this case, a single diffraction experiment does not identify the origin of any peak in the PDF in terms of specific atomic pair correlations.

One solution of these difficulties is the construction of models which simulate the structure. Structural parameters such as the PDF, density, etc. may be computed for the structural model, and the theoretical predictions compared with experiment. The importance of structural modeling lies in the fact that a detailed quantitative analysis of the structure may thereby be gained. For instance, the structural origin of features in the computed PDF may readily be ascertained with the use of a model, information often impossible to ascertain in any other way. Despite the fact that in a glass, the structure is very complex in comparison with crystalline materials, a lot of work has been done towards modeling the structure of glasses [92, 122, 123, 124].

In this chapter, we present the work done towards modeling the structure of Ge_xSe_{1-x} glasses around the IP. Much emphasis has been done on modeling the structure of $GeSe_2$ glass as its structure plays an essential role in the Ge_xSe_{1-x} system as a prototypical glass.

4.2 Structural insight from crystalline analogs

One key point about the network evolution as a function of Ge content is the evolution of corner and edge sharing tetrahedra. a-Se has a chain structure where each Se atom is 2-fold coordinated, adding Ge (cross linking element) to the Se chains brings about the $Ge(Se_{1/2})_4$ tetrahedra that are the basic building block in Ge_xSe_{1-x} glasses. For low Ge content, these tetrahedra are immersed in a floppy Se matrix, adding more and more Ge atoms results in linking these tetrahedra through their corners and edges. In the following sections we discuss refining the glassy structure of $GeSe_2$ using the relaxed crystalline analogues in order to examine the existence of corner and edge sharing tetrahedra in the structure.

In order to quantify the PDF data, we made a structural comparison of the stoichiometric g-$GeSe_2$ with the known structure of c-$GeSe_2$, in its low temperature (α-$GeSe_2$) and high temperature (β-$GeSe_2$) forms.

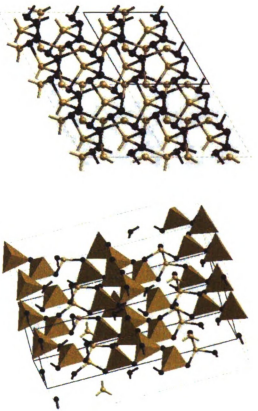

Figure 4.1: The crystal structure of the low temperature α-$GeSe_2$. Ball and stick representation (upper figure) and polyhedral representation (lower figure). Images in this figure are presented in color.

The structure of the LT α-$GeSe_2$ is described to form two-dimensional layers composed of $Ge(Se_{1/2})_4$ tetrahedra being connected through their corners. This is shown in Figure 4.1, which shows the unit cell of α-$GeSe_2$. On the other hand, the structure of the high temperature β-$GeSe_2$ phase is composed of $Ge(Se_{1/2})_4$ tetrahedra being connected through their corners and edges forming a three-dimensional network, as shown in Figure 4.2. From the crystalline models, we can calculate total PDFs to compare with the glassy data, but also partial PDFs which help us to assign meaning to features in the glassy PDFs. Figure 4.3 shows a comparison between the LT and HT crystalline phases in their calculated total and partial PDFs. In the background of each panel in Figure 4.3, the experimental total PDF of g-$GeSe_2$

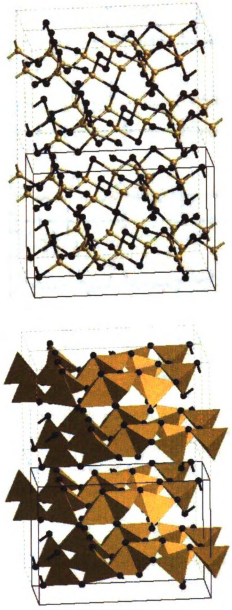

Figure 4.2: The crystal structure of the high temperature β-$GeSe_2$. Ball and stick representation (upper figure) and polyhedral representation (lower figure). Images in this figure are presented in color.

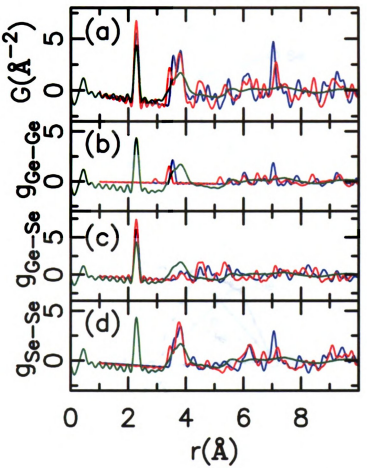

Figure 4.3: Comparison between the calculated PDFs for both LT (blue curves) and HT (red curves) phases of crystalline $GeSe_2$. In the background of each panel, the experimental total PDF of g-$GeSe_2$ (green) is plotted for comparison. (a) Total PDFs, (b) Ge-Ge correlations, (c) Ge-Se correlations, and (d) Se-Se correlations. Images in this figure are presented in color.

is shown for comparison. The excellent match between the first PDF peak in both crystalline and glassy data is evident, which proves that the basic structural unit in the glass is the same as in the crystalline phases which is the $Ge(Se_{1/2})_4$ tetrahedra. The partial PDFs, Ge-Ge (panel b) and Se-Se (panel d) have almost zero probability at the location of the first PDF peak, which proves that the crystalline phases have no homo-polar (wrong) bonds. The relatively broad distribution of the second PDF peak in the glass is consistent with the fact that the crystalline analogs contain multiple peaks in this region. Both LT and HT phases contain Ge-Ge, Ge-Se and

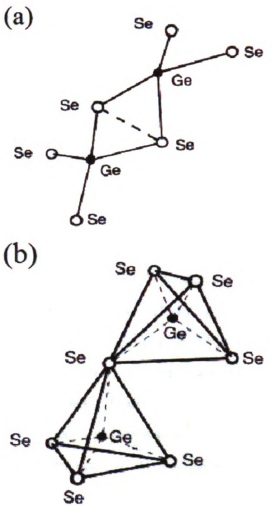

Figure 4.4: (a) Illustration of edge-sharing tetrahedra (EST) and (b) illustration of corner-sharing tetrahedra (CST).

Se-Se correlations in this region. However, from their relative intensity, the second PDF peak is mostly due to the Se-Se correlations, and the shoulder in the leading edge of this peak is mostly due to Ge-Ge correlations.

Existence of edge-sharing tetrahedra (EST) (see Figure 4.4(a)) and their percentage relative to the corner-sharing tetrahedra (CST) (see Figure 4.4(b)) in Ge_xSe_{1-x} glasses plays an important role in determining the intermediate range order (IRO) and rigidity of the networks. In order to determine if the glassy data have EST or not, together with determining the extent to which the crystalline models result in

Table 4.1: Refined fit parameters for α and β phases of c-$GeSe_2$.

Refined parameter ($Å^2$)	phase α	phase β
U_{11}	0.006	0.035
U_{22}	0.032	0.022
U_{33}	0.011	0.013
R_w	0.125	0.062

PDFs that are similar to the glassy data, we have fitted the glassy data of $GeSe_2$ using PDFgui [94] (a full-profile real-space local-structure refinement program). This is possible because the α crystalline form of $GeSe_2$ has purely corner-shared tetrahedra, whereas the β form has half of the tetrahedra in edge-shared and half in corner-shared configurations. PDFs were calculated from both the α and β crystalline models using structural parameters from Refs. [65, 54] and [65, 55], respectively. Starting from a given structural model and given a set of parameters to be refined, PDFgui program searches for the best structure that is consistent with the experimental PDF data. The residual function (R_w; defined in Equation 2.6) is used to quantify the agreement of the calculated PDF from model to the experimental data. The protocol we used in this approach was fixing the unit cell dimensions and angles to the values of the crystalline structure, but increasing the thermal parameters (U_{ij}) to account for the glass structure.

The PDF peaks were broadened by increasing the atomic displacement parameters (ADP) in the model; whilst keeping the first PDF peak sharp. The model PDFs were convoluted with a Sinc function to account for the finite Q-cutoff of the image plate data. The calculated model PDFs in comparison with the experimental data are shown in Figure 4.5. Table 4.1 lists the resulting refined parameters when using both the α and β phases together with the agreement factor (R_w).

Comparing Figure 4.5(a) and (b) we see that the β structural model does a significantly better job of reproducing the glass data. Thus, a structure consisting of a

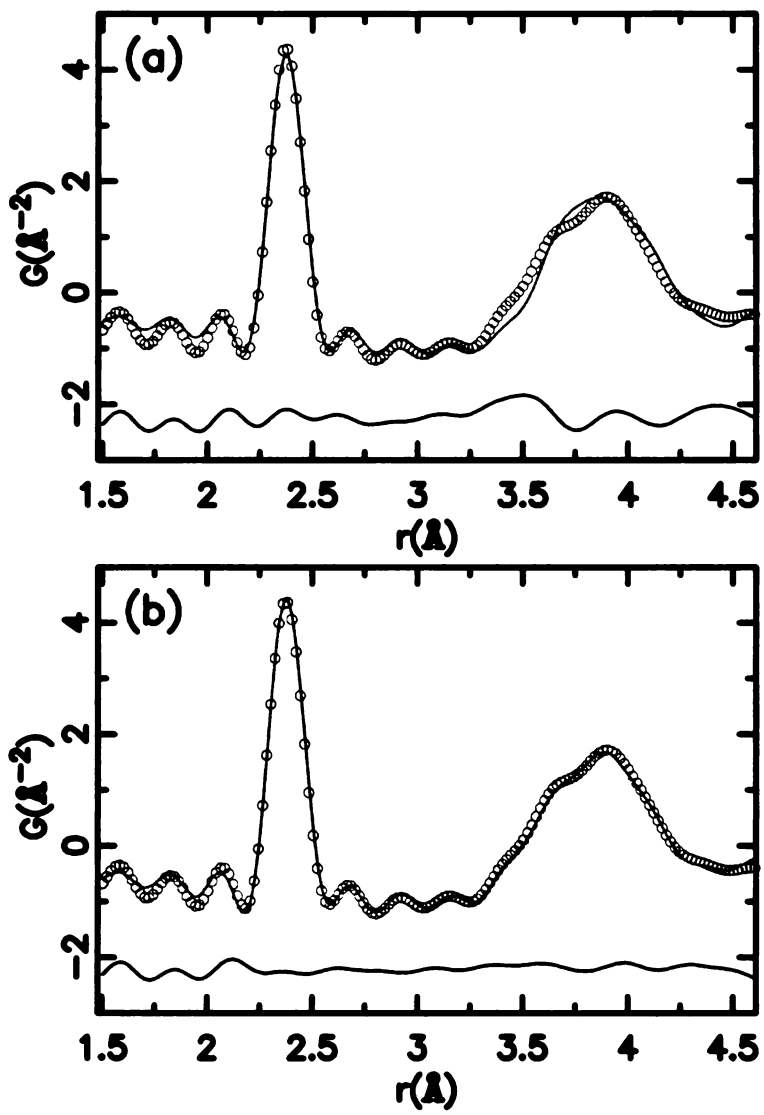

Figure 4.5: The calculated model PDFs (red curve) compared with the experimental data (blue circles) with the difference (green curve) offset below. (a) Fit to LT α-$GeSe_2$ and (b) fit to HTβ-$GeSe_2$. Images in this figure are presented in color.

mixture of edge and corner-shared tetrahedra is consistent with the g-$GeSe_2$ PDF and the shoulder on the leading edge of the second-neighbor peak in the glassy PDF data is an indicator for the existence of edge sharing of the tetrahedra. The purely corner-shared structure of α-$GeSe_2$ results in a second peak that has the wrong shape and is significantly shifted compared to the data from the glass. This is strong evidence for the existence of a mixture of edge- and corner-shared tetrahedra in g-$GeSe_2$.

As the structures of both LT and HT phases are dramatically different in terms of tetrahedral connectivity, and since the main difference in their calculated PDFs is in the region of the shoulder in the second PDF peak, it is interesting to investigate the behavior of this shoulder across the series of the studied samples. Figure 3.11 shows the development of this shoulder, which is the main difference in the PDFs, when going from low Ge to high Ge content. This supports the suspicion that the origin of this shoulder is edge-shared tetrahedra that are becoming more frequent with increasing Ge content.

Structural information about the network connectivity as a function of doping, percentages of EST and CST, bond-angle distribution, and the ring structure can not be determined directly from the data, as there are no crystalline analogs at every concentration, x, to be refined similar to the case of g-$GeSe_2$. The accuracy of the obtained information depends entirely on the accuracy of the obtained models. Following is a description of the efforts done towards modeling the structure of Ge_xSe_{1-x} glasses around the rigidity percolation threshold.

4.3 First principles molecular dynamics simulations on Ge_xSe_{1-x} system

In collaboration with Professor David Drabold's research group at the University of Ohio, we have obtained a set of structural models for Ge_xSe_{1-x} glasses using first

principles molecular dynamics simulations with compositions that span the region of the IP. Following is a description of how the models were generated, the statistical analysis of these models and an assessment of the quality of these models.

4.3.1 Model generation

This work was carried out by F. Inam and D. A. Drabold. The procedure is summarized here for completeness. The *ab initio* density functional code, FIREBALL, developed by Sankey and co-workers [125, 126] was used to generate the structural models. This method has been used very successfully for a variety of covalently bonded systems, and especially glassy germanium selenide [76, 127, 124]. A set of 500-atom models for Ge_xSe_{1-x} glasses were generated with $x = 0.10, 0.15, 0.18, 0.22, 0.23, 0.25$ *and* 0.33 using quench from melt technique.

Atoms were randomly placed in a cubic cell with a suitable and fixed volume. The temperature of the cells in the MD simulation is then set to 4200 K, and then equilibrated at 1500 K for about 3.5 ps. Following this, they were quenched to 400 K over about 4.5 ps, using velocity re-scaling. Finally, the cells were steepest descent quenched to 0 K. These model configurations were compared to a series of models that have been proposed earlier ($GeSe_4$ (x = 0.20), $GeSe_9$ (x = 0.10) [124] and $GeSe_2$ (x = 0.33) by Cobb *et al.* [76]. All these models have similar densities. A qualitative view of one of the generated models is shown in Figure 4.6.

4.3.2 Assessment of the MD models

These models were generated using interatomic potentials that are presumed to be appropriate, and using MD methods that are presumed to find the equilibrium structure. To validate the quality of the models we would like to compare them to our high-quality PDF data. Figure 4.7 shows a comparison between the experimental and calculated PDFs from the models. From this we see a very good agreement in

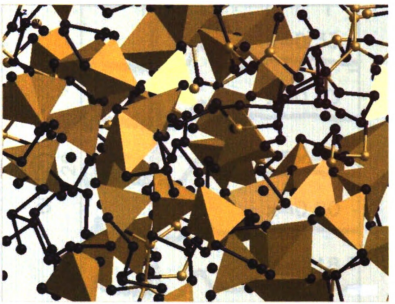

Figure 4.6: Representative plot of the structure of $Ge_{0.20}Se_{0.80}$ as obtained from the molecular dynamics simulations. Black and gold circles represent Ge and Se atoms, respectively. Some of the basic structural units $(Ge(Se_{1/2})_4$ tetrahedra) are also shown. Images in this figure are presented in color.

the region of the first shell, but a relatively poor agreement in the second shell. The relatively large difference between the experimental and calculated PDFs at about 3.5 Å is clear.

This indicated that the produced models were able to generate the basic structural unit($Ge(Se_{1/2})_4$ tetrahedra), but were not fully able to reproduce the region between 3 and 4 Å. This region, as we showed earlier in this chapter, is of particular interest as it has important information about the way these tetrahedra are linked to each other.

In order to test if the MD models are tracking the fine changes that occur in the experimental data, we have plotted the difference curves between successive values of x (Ge content) for both MD models and the data. Figure 4.8 shows these difference curves. Despite the fact that the difference curves in the MD data are noisy and do not depict the fine details, their absolute values are comparable with those in the experimental data.

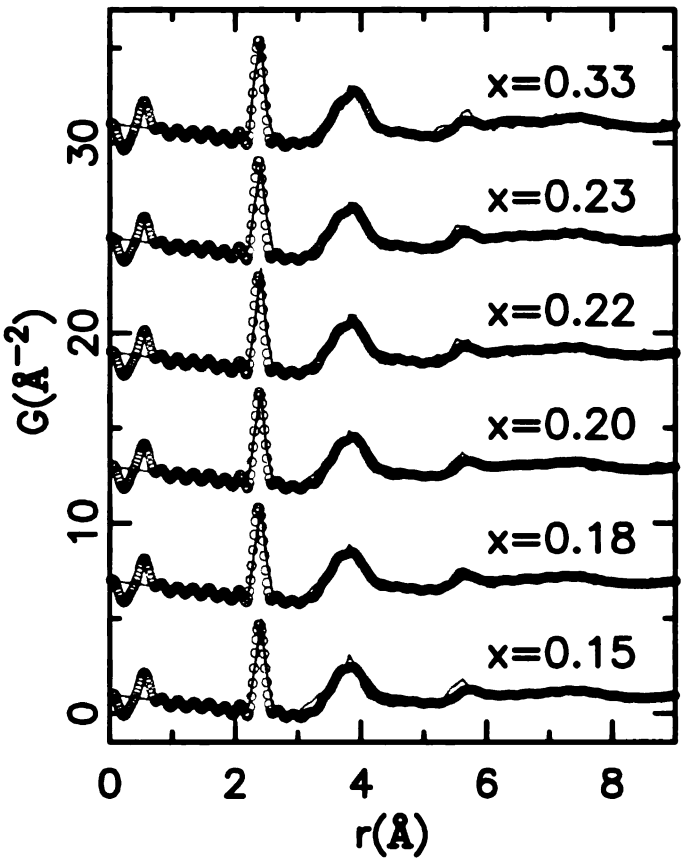

Figure 4.7: Comparison between calculated PDFs obtained from the MD structural models (red curves) with the experimental data (blue circles). Images in this figure are presented in color.

As the general agreement between the models and the experimental data is reasonable, the experimentally constrained molecular relaxation (ECMR) technique [123] will be used in subsequent work to tune the structure of these glasses by using the X-ray diffraction data as a constraint in the model formation process. The starting point for these calculations will be the set of models that are reported here. Following is a statistical analysis of the produced MD models.

4.3.3 Models analysis: Coordination, rings and constraints

In the Ge_xSe_{1-x} system, tetravalent (4-fold) Ge and divalent (2-fold) Se are the fundamental building blocks for the network. For x small enough, 2-fold Se exist in the

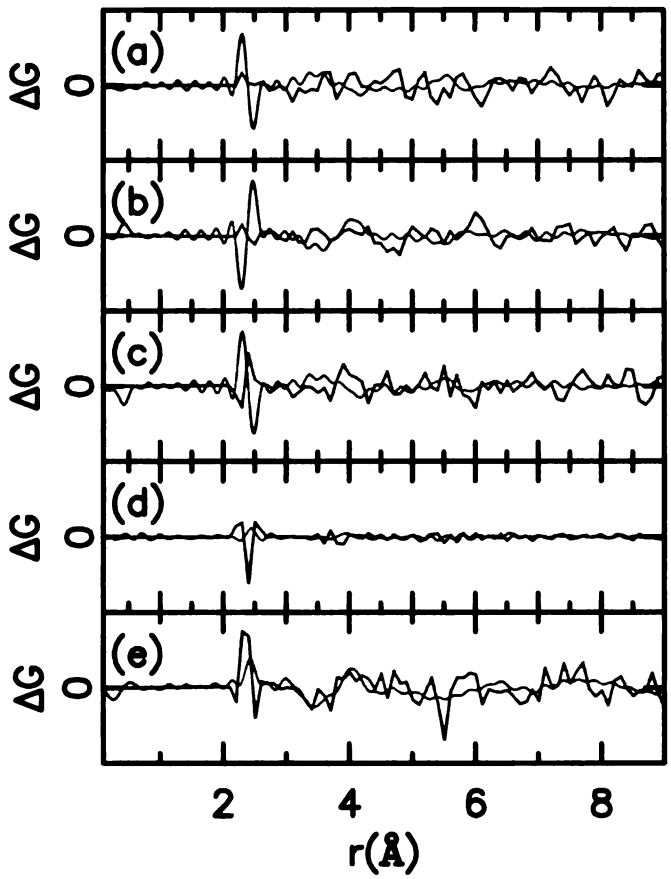

Figure 4.8: Difference curves between successive values of x (Ge content) in the experimental data (red curves) and MD models (blue curves). The difference curves (ΔG (Å^{-}2)) are (a) $\Delta G = G(0.18) - G(0.15)$, (b) $\Delta G = G(0.20) - G(0.18)$ (c) $\Delta G = G(0.22) - G(0.20)$ (d) $\Delta G = G(0.23) - G(0.22)$, and (e) $\Delta G = G(0.33) - G(0.23)$, where here the arguments indicate the composition. Images in this figure are presented in color.

form of long chains, while 4-fold tetrahedral Ge connect these chains to each other and form closed rings. Adding Ge atoms in a Se-rich environment increases the mean coordination per atom. The mean coordination number was defined in Equation 1.2 and can be simplified as in Equation 4.1:

$$\bar{r} = \frac{\sum_r r n_r}{\sum_r n_r} \tag{4.1}$$

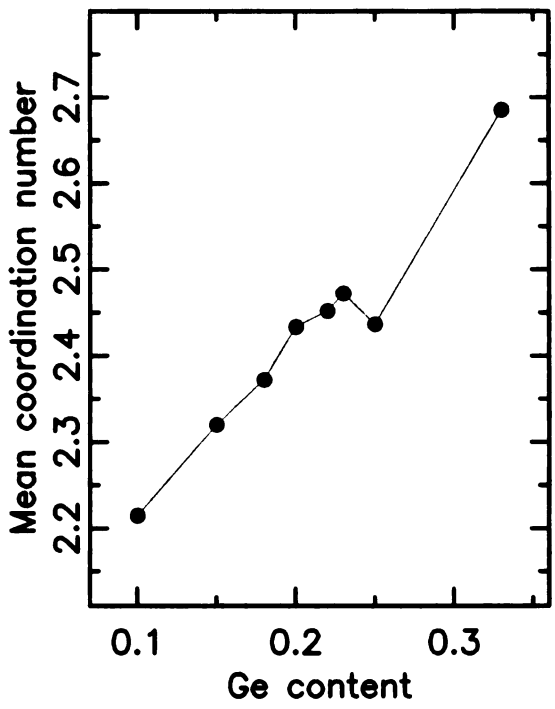

Figure 4.9: Mean coordination number as obtained from MD simulations. The line between the points is just guide to the eye. Images in this figure are presented in color.

where r runs over all the coordinations present in the system, and n_r is the number of atoms with coordination r. Mean coordination, $\bar{r}$, is an important parameter to describe the network.

Figure 4.9 shows the increase in $\bar{r}$ with Ge concentration, as obtained from the MD simulation. It is interesting to note that the increase is not linear, as it is in the simple-minded modeling that neglects self-organization that was discussed in Chapter 3. Between $x = 0.20$ and $x = 0.25$, $\bar{r}$ briefly saturates suggesting a kind of "resistance" the system offers to further increase in the number of bonds per atom. This result depends on a small number of points and needs to be confirmed in greater detail. As described later, the signature of this behavior is present in the overall evolution of the network.

Figure 4.10 shows the variation in the coordination of both Ge and Se atoms as a function of Ge concentration. From $x = 0.10$ to $x = 0.18$ the concentration of

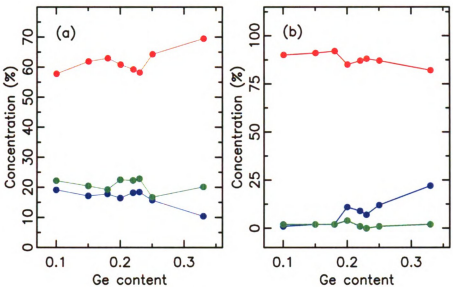

Figure 4.10: (a) The concentration of 1 (blue), 2 (red) and 3 (green) fold Se in the produced MD models and (b) the concentration of 3 (blue), 4 (red) and 5 (green) fold Ge in the produced MD models. The lines between the points are just guides to the eye. Images in this figure are presented in color.

2-fold Se increases linearly from 58 to 63%. Between $x = 0.18$ and $x = 0.25$ the concentration first decreases, and then abruptly increases to 72%. These simulations suggest that a significant proportion of Se is not 2-fold coordinated, contrary to the assumptions used in Chapter 3.

With increasing Ge concentration, the system gradually eliminates homopolar Se bonds and forms chemically preferred Se-Ge bonds. A consequence is the transition which occurs in the neighbors of 2-fold Se (Figure 4.11(b)), that is, a gradual replacement of Se neighbors with Ge neighbors. At lower Ge content, 2-fold Se have more Se neighbors as compared to Ge neighbors. Increase in Ge content starts to replace Se with Ge atoms as the neighbors of 2-fold Se. At $x = 0.20$, concentration of 2-fold Se with neighbors Se_1Ge_1 assumes a higher value compared to 2-fold Se with Se_2Ge_0 and Se_0Ge_2 neighbors as shown in Figure 4.11(b).

The increase in Se_1Ge_1 units at $x = 0.20$ affects the evolution of corner sharing tetrahedra (CST) and the ring structure as shown in Figure 4.12. Due to the high

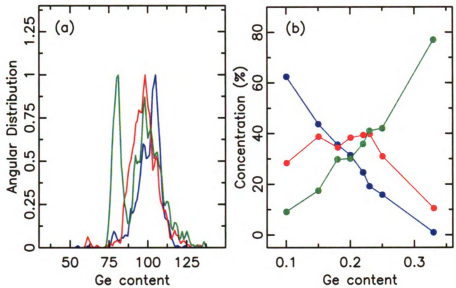

Figure 4.11: (a) Bond angle distribution of 2-fold Se units and (b) variation of concentration of types of neighbors of 2-fold Se: Ge_0Se_2 (blue), Ge_1Se_1 (red) and Ge_2Se_0 (green). Lines are guide to the eye. Note the "flattening" of Se_1Ge_1 concentration near the IP window. Images in this figure are presented in color.

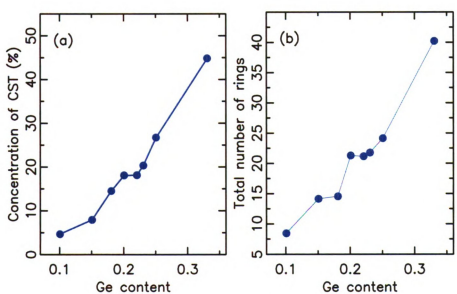

Figure 4.12: (a) Concentration of corner-sharing tetrahedra and (b) total number of rings, as obtained from MD simulations to Ge_xSe_{1-x} glasses. Images in this figure are presented in color.

concentration of Se_1Ge_1 units in the range $x = 0.20$ to 0.25, concentration of CST and total number of rings tend to saturates in this range (Figure 4.12(a) and (b)). It is clear that the transition from all Se neighbors around Se sites to Ge neighbors, occurs roughly through a range $x \in$ (0.20 to 0.25) which may be a signature of the sought-after "self organization". Below $x = 0.18$, 4-fold tetrahedral units reveal a slight increase while it is fluctuating between $x = 0.20$ and $x = 0.25$. At $x = 0.20$, 3-fold Ge increases to a considerable concentration of 10% of Ge content (Figure 4.10(b)).

Figure 4.11(a) shows the angle distribution for 2-fold Se units averaged over all x. Interesting feature is the lower angle peak (around 80°) for Se_0Ge_2 units which is due to the formation of 4-fold rings (edge sharing tetrahedra units). Se_1Ge_1 shows a broad shoulder around 90° of the main peak centered at about 97°. This shoulder also comes from 4-fold rings consisting of mainly 3 Se and 1 Ge atoms. Se_2Ge_0 units show a high peak around 105° due to open chain like structures or larger size rings consisting of mainly Se atoms.

Based on the statistical analyses done on the previous molecular dynamics models for Ge_xSe_{1-x} glasses, it is clear that some structural anomalies appear to correlate with the predicted IP. In particular, the network evolves from a-Se_2 to $GeSe_2$ through a range of Ge composition which roughly coincides with the IP, by keeping a relatively high concentration of isostatic 2-fold Se units having one Se and one Ge neighbor in this range. This behavior resists the overall structural evolution of the network, probably due to the minimization of free energy, $F = U - TS$, in the IP window. Increase in the concentration of 2-fold Se bonded with one Ge in the IP range, which are isostatic in nature, could be the origin of lowering of stress in IP proposed by Thorpe *et al.* [1]. This theoretical signature of the IP makes it reasonable to fully assess the quality of the generated MD models, especially in the region between 3 to 4 Å, where dramatic changes occur in the structure in terms of tetrahedral connectivity. To test the behavior of the MD models in this region (3 - 4 Å), we

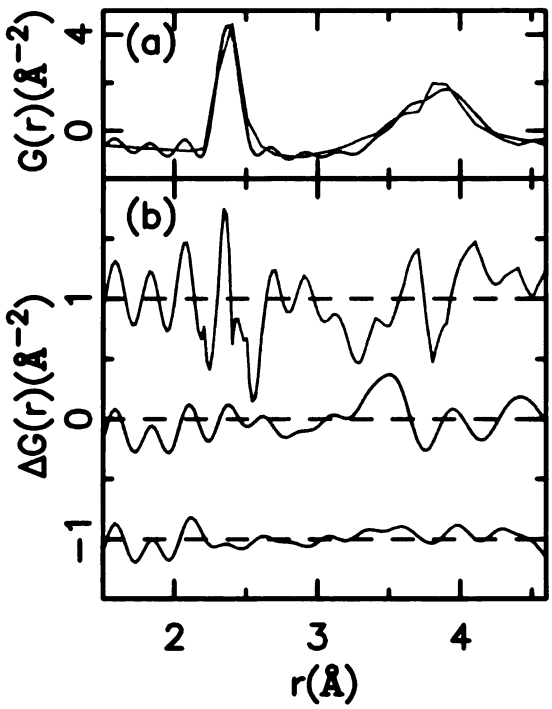

Figure 4.13: (a) Comparison between the MD model calculated PDF and the experimental data for the $GeSe_2$ glass. (b) The difference curves between experimental PDF and the calculated PDF from MD models (red curve), LT α phase (green curve) and the HT β phase (blue curve). Images in this figure are presented in color.

have plotted the calculated PDF from the MD model of $GeSe_2$ glass against the experimental one. Figure 4.13 shows that the MD model is not reproducing the exact shape of the second PDF peak (see Figure 4.13(a)). In Figure 4.13(b) we show the difference curves between the experimental PDF of $GeSe_2$ glass and the calculated one from the MD model as well as from the LT and HT phases of $GeSe_2$ glass. It is clear that the difference curve is large in case of the MD model, with agreement factor (R_w) of 0.243, compared with 0.125 and 0.062 in case of the LT and HT models, respectively. From these difference curves, it is clear that even the LT phase (which has the wrong structure) fitted the data much better than the MD model. This brings about the importance of validating the quality of the MD models, and shows that these models are not perfect, and need more improvements in the region between 3 to 4 Å.

4.4 Conclusions

As we saw from the above discussion, the basic building block in the glass is similar to that in the crystalline phase, which is the $Ge(Se_{1/2})_4$ tetrahedra. The difference is in how these tetrahedra are linked to each other. Through the structural refinement using both α and β phases of $GeSe_2$ we have proven that the glassy data have both corner- and edge-sharing tetrahedra.

The connectivity of the tetrahedra affects the average coordination number, and hence the number of constraints per atom. Edge-sharing tetrahedra (EST) are more strained than the corner-sharing (CST) ones, and hence, the percentage of EST to CST plays an essential role in determining strain in the glass. This percentage can easily be determined from the areas of the peaks responsible for EST and CST. Unfortunately, these peaks are largely overlapped in Ge_xSe_{1-x} glasses which makes it impossible to get their areas for certainty.

Through the analysis of the MD models, we have seen that these models were able to reproduce the basic structural unit ($Ge(Se_{1/2})_4$ tetrahedra), but were unable to fully reproduce the medium range order. On the other hand, as Ge and Se have to be 4- and 2-fold coordinated, respectively, any deviation from this (as shown in Figures ??(b) and (c), where there are a relatively large percentage of 1-fold and 3-fold Se as well as 3- and 5-fold Ge) is considered as defects in the structure. This draws into question the validity of the MD models, and shows that even the theoretical signature of the IP (as these models suggest) is probably unrealistic, and the value of these models is over estimated.

Chapter 5

Summary and conclusions

5.1 Summary and conclusions

Self-organization in network glasses, where the structure can incorporate non-random features to minimize the free energy at the temperature of formation, has been proposed by Thorpe *et al.* [1]. Their prediction came from studying a self-organized model of a network in which configurations that are stressed are avoided where possible. They found that this avoidance leads to two phase transitions and an intermediate phase that is rigid but stress-free (unstressed, where all bond lengths and bond angles have their optimal values).

Chalcogenide glasses exhibit some signs of a first-order transition when the composition is varied, as observed by Raman scattering [3, 46], and also some evidence for the intermediate phase was found using differential scanning calorimetry [3, 46].

Boolchand *et al.* [3, 34] using Raman scattering studies on Ge_xX_{1-x} glasses (X=S or Se) showed a jump in the composition dependence of the frequency of the mode corresponding to symmetric stretch of $Ge(X_{1/2})_4$ tetrahedra. For both S and Se, this change occurs around the composition $x = 0.225$, which corresponds to a mean coordination $< r > = 2.45$, and may correspond to the transition to the stressed state. On the other hand, their modulated differential scanning calorimetry (MDSC)

measurements on a variety of glasses [4, 40, 41, 38, 42, 43, 44] showed a universal feature of having the non-reversing heat flow (ΔH_{nr}) vanish in a finite composition range. They called the composition range for these thermally reversing transitions the intermediate phase (IP) or reversibility windows.

However, the experimental positions of the IP, as found by Boolchand *et al.* [3] (from $< r > = 2.40$ to 2.45) do not coincide with the theoretical prediction (from $< r > = 2.375$ to 2.392), which may be due to the simplicity of the theoretical models. On the other hand, the theory predicts that the IP is about three times narrower than the experimental finding of Boolchand's *et al.* [1, 3]. These two discrepancies between theory and experiment about the IP casts doubt on the equivalence of the two.

In this study, a search for a structural response to the intermediate phase (IP) and a signature for its predicted self-organization [1, 2] has been performed. Based on the large number of published papers [2, 46, 48] on the so-called IP and the fact that many of these papers considered that the existence of the IP had been really well established from experiments, we were motivated to search for a structural response to this phase.

High-resolution atomic pair distribution functions, derived from high-energy synchrotron radiation, coupled with high-resolution X-ray absorption fine structure (XAFS) measurements on 18 compositions of well-prepared Ge_xSe_{1-x} glasses that span the range of the IP have been performed to elucidate aspects of rigidity percolation and the IP. These data are the most complete and highest-resolution study of this system to date.

Analysis of the evolution with composition of the structure functions (in reciprocal space) and the PDFs (in real space), as well as the XAFS data at both Ge and Se edges, show no discernable correlations with the IP. Structural parameters evolve smoothly without any discontinuity or break in slope that might be linked to the IP. The results obtained in this study contradict previously published works [6, 7] that

claim experimental evidence of the existence of the IP.

According to the IP hypothesis, samples in this phase should be in a stress-free state. Both PDF and XAFS are local structural probes that can detect changes in the stress state of the network. Analysis of the first PDF peak position (which is sensitive to homogenous strain) and the first PDF peak width (which is sensitive to inhomogeneous strain) show no correlation with the IP boundaries. Debye-Waller factors obtained form the XAFS data for both Ge-Se and Se-Se bonds also indicate no correlations with the IP. The data show no detected bond strain evident until approximately $x \geq 0.30$ as evident from the first PDF peak positions and widths, surprising given the IP model.

The IP was explained to be in a stress-free state due to self-organization. If the network is in a self-organized state, one expects this to be reflected in the network's medium-range order (MRO). A signature of the MRO is the so-called first sharp diffraction peak (FSDP). Despite the fact that this peak is a subject of debate in its structural origin, almost all of the glass community agree that it is a signature of MRO. Analysis of the different parameters of this peak show no correlation with the IP. We expect self-organization of the network in the IP to result in a maximum amplitude and minimum width of this peak for samples in the IP, which is not the case.

The FSDP changes systematically with Ge content, it develops smoothly from a relatively small background for low Ge-content to a well-defined and sharp peak at the stoichiometric composition ($GeSe_2$). Its position shifts towards lower Q-values when the Ge content is increased. The height of this peak reaches its maximum at the stoichiometric composition ($x = 0.33$) after which it starts to decrease. This is interpreted as being due to the change in the role of Ge atoms in the network. For $x <$ 0.33, the Ge atoms work as network formers, so adding Ge will result in a progressive increase in the correlations contributing to this peak [119]. On the contrary, for $x >$

0.33, Ge atoms work as network modifiers [119]. This will weaken the ordering of the correlations responsible for the FSDP and hence decrease its intensity.

Consistency of the PDF and XAFS data was examined by simulating the first PDF peak using the XAFS data based on the chemically ordered network (CON) model. The parameters derived from the simulated peak agree well with the experimental ones, which proves the consistency among the data, and shows that the CON model is reasonable for describing the structure of Ge_xSe_{1-x} glasses.

The basic structural unit in the Ge_xSe_{1-x} glasses is the $Ge(Se_{1/2})_4$ tetrahedron [80], where each Ge atoms is tetrahedrally bonded to 4 Se atoms. These tetrahedra are, for low Ge contents, immersed in a floppy Se-matrix. Adding more Ge results in a progressive linking of each other through their corners and edges. Results obtained from the analysis of the first PDF peak are consistent with the CON model, where Ge and Se atoms maintain the four- and two-fold coordination respectively, consistent with the '8-N' rule. In the composition range of the studied samples, and according to the CON model, the first PDF peak is mainly due to Ge-Se bonds, but the Se-Se and Ge-Ge homopolar bonds are exist in the low Ge and high Ge regions, respectively.

Real-space structure refinement of g-$GeSe_2$ using the two crystalline forms of $GeSe_2$ was performed. The LT-α phase is made up of completely corner-sharing tetrahedra, while the HT-β phase is made up of both corner- and edge-sharing of the tetrahedra. The HT-β phase fit the data perfectly and showed that the basic structural unit in the glass is similar to that in the crystalline analog and suggests that the glassy data contains both corner- and edge-sharing of the tetrahedra.

Statistical analysis of structural parameters of a set of structural models of Ge_xSe_{1-x} glasses obtained using *ab initio* molecular dynamics simulations was performed. Though the analysis showed some structural features that might be linked to the proposed IP, the MD models have a relatively large number of structural defects (existence of 1- and 3-fold Se as well as 3- and 5-fold Ge). The MD models did not reproduce the

PDF data well enough, nor the composition dependence of changes in the PDF, to give confidence that they represent the structure of the real glasses.

In summary, our high-resolution PDF and XAFS data do not provide any conclusive evidence to support a structural origin for the region of low non-reversing heat-flow, and no direct evidence for an IP as envisaged theoretically. This could be due to two reasons: either any structural changes due to the IP are below the sensitivity of PDF and XAFS methods, or there is no such phase.

5.2 Future work

Through the analysis of the PDF data, it was difficult to identify the structural origins of the peaks in the MRO with certainty due to the highly overlapped shells. In this study, we have used the XAFS method to extract the differential PDFs and identify the origin of the different peaks in the PDF at the short range order (SRO) scale.

However, peaks in the PDF data extend up to about 10 Å, and identifying their origin can not be achieved through XAFS technique, since XAFS is a SRO probe. A structural probe that is element specific and is able to identify peaks at the medium range order (MRO) is required to gain full insight about the evolution of the network and to fully identify the structural origin of the peaks in the PDF.

We propose measuring this set of samples using X-ray anomalous scattering and/or neutron isotope substitution. These two techniques can fully identify the structural origins of the different peaks in the PDF, and hence sub-peak parameters can be analyzed and their evolution versus Ge-doping can be obtained.

The rigidity transition can be expected to manifest directly in the elastic response of a network. Thus elastic constants probed by ultrasonic echoes [128, 129, 130, 131, 132, 133, 134], Brillouin scattering and Raman scattering [3, 46, 69, 135] appear to be some of the most direct methods to probe the transition.

It is interesting to look to the behavior of the Boson peak [136] as a function of

composition in this set of glasses. This may help both interpret the structural origin of the Boson peak as well as look for any structural responses to the IP on this peak.

On the other hand, it would be interesting to measure these samples at a relatively high temperature to suppress non-covalent bonds. This may narrow the gap between the theoretical prediction of the IP and the experimentally found IP through MDSC measurement.

For the modeling part, we plan on doing a co-refinement using the PDF and XAFS data. This is expected to improve the structural models and hence provide better understanding of the structure of Ge_xSe_{1-x} networks.

Bibliography

[1] M. F. Thorpe, D. J. Jacobs, M. V. Chubynsky, and J. C. Phillips, **Self-organization in network glasses**, J. Non-Cryst. Solids **266**, 859–866 (2000).

[2] P. Boolchand, D. G. Georgiev, and B. Goodman, **Discovery of the intermediate phase in chalcogenide glasses**, J. Optoelectron. Adv. M. **3**, 703–720 (2001).

[3] X. W. Feng, W. J. Bresser, and P. Boolchand, **Direct evidence for stiffness threshold in chalcogenide glasses**, Phys. Rev. Lett. **78**, 4422–4425 (1997).

[4] D. Selvanathan, W. J. Bresser, and P. Boolchand, **Stiffness transitions in Si_xSe_{1-x} glasses from Raman scattering and temperature-modulated differential scanning calorimetry**, Phys. Rev. B **61**, 15061–15076 (2000).

[5] M. F. Thorpe, **Continuous deformations in random networks**, J. Non-Cryst. Solids **57**, 355–370 (1983).

[6] Y. Wang, E. Ohata, S. Hosokawa, M. Sakurai, and E. Matsubara, **Intermediate-range order in glassy Ge_xSe_{1-x} around the stiffness transition composition**, J. Non-Cryst. Solids **337**, 54–61 (2004).

[7] D. Sharma, S. Sampath, N. P. Lalla, and A. M. Awasthi, **Mesoscopic organization and structural phases in network-forming Ge_xSe_{1-x} glasses**, Physica B **357**, 290–298 (2005).

[8] W. H. Zachariasen, **The atomic arrangement in glass**, J. Am. Chem. Soc. **54**, 3841–3851 (1932).

[9] S. R. Elliott, *Physics of amorphous materials*, Longman, London and New York, 1st edition, 1984.

[10] R. M. Almeida, L. F. Santos, A. Simens, A. Ganjoo, and H. Jain, **Structural heterogeneity in chalcogenide glass films prepared by thermal evaporation**, J. Non-Cryst. Solids **353**, 2066–2068 (2007).

[11] G. Abbas, P. Papakonstantinou, G. R. Iyer, I. W. Kirkman, and L. C. Chen, **Substitutional nitrogen incorporation through rf glow discharge treatment and subsequent oxygen uptake on vertically aligned carbon nanotubes**, Phys. Rev. B **75**, 195429 (2007).

[12] X. X. Xi et al., **MgB_2 thin films by hybrid physical-chemical vapor deposition**, Physica C **456**, 22–37 (2007).

[13] D. Carta, D. M. Pickup, J. C. Knowles, I. Ahmed, M. E. Smith, and R. J. Newport, **A structural study of sol-gel and melt-quenched phosphate-based glasses**, J. Non-Cryst. Solids **353**, 1759–1765 (2007).

[14] K. Minami, F. Mizuno, A. Hayashi, and M. Tatsumisago, **Lithium ion conductivity of the Li_2S-P_2S_5 glass-based electrolytes prepared by the melt quenching method**, Solid State Ionics **178**, 837–841 (2007).

[15] S. Uemiya, T. Endo, R. Yoshiie, W. Katoh, and T. Kojima, **Fabrication of thin palladium-silver alloy film by using electroplating technique**, Mater. Trans. **48**, 1119–1123 (2007).

[16] Y. Ashkenazy and R. S. Averback, **Shock induced amorphization as the onset of spall**, Appl. Phys. Lett. **86**, 051907 (2005).

[17] D. Guerard, R. Janot, J. Ghanbaja, and P. Delcroix, **Ball-milling with a fluid: A powerful means for new syntheses**, J. Alloy. Compd. **434**, 410–414 (2007).

[18] J. C. Phillips, **Topology of covalent non-crystalline solids 1. Short-range order in chalcogenide alloys**, J. Non-Cryst. Solids **34**, 153–181 (1979).

[19] F. Betts, A. Bienenstock, and S. R. Ovshinsky, **Radial distribution studies of amorphous Ge_xTe_{1-x} alloys**, J. Non-Cryst. Solids **54**, 554–563 (1970).

[20] D. Shechtman, I. Blech, D. Gratias, and J. W. Cahn, **Metallic phase with long-range orientational order and no translational symmetry**, Phys. Rev. Lett. **53**, 1951–1953 (1984).

[21] T. Egami and S. J. L. Billinge, *Underneath the Bragg peaks: structural analysis of complex materials*, Pergamon Press, Elsevier, Oxford, England, 2003.

[22] J. L. Lagrange, *Mecanique analytique*, Paris, 1788.

[23] J. C. Maxwell, **On the calculation of the equilibrium and stiffness of frames**, Philos. Mag. **27**, 294–299 (1864).

[24] J. C. Phillips, **Topology of covalent non-crystalline solids 2. Medium-range order in chalcogenide alloys and a-Si(Ge)**, J. Non-Cryst. Solids **43**, 37–77 (1981).

[25] R. Keller, W. B. Holzapfel, and H. Schulz, **Effect of pressure on atom positions in Se and Te**, Phys. Rev. B **16**, 4404–4412 (1977).

[26] W. A. Kamitakahara, R. L. Cappelletti, P. Boolchand, B. Halfpap, F. Gompf, D. A. Neumann, and H. Mutka, **Vibrational densities of states and network rigidity in chalcogenide glasses**, Phys. Rev. B **44**, 94–100 (1991).

[27] U. Senapati and A. K. Varshneya, **Configurational arrangements in chalcogenide glasses - a new perspective on phillips constraint theory**, J. Non-Cryst. Solids **185**, 289–296 (1995).

[28] M. Tatsumisago, B. L. Halfpap, J. L. Green, S. M. Lindsay, and C. A. Angell, **Fragility of Ge-As-Se glass-forming liquids in relation to rigidity percolation, and the Kauzmann paradox**, Phys. Rev. Lett. **64**, 1549–1552 (1990).

[29] M. Stevens, J. Grothaus, P. Boolchand, and J. G. Hernandez, **Universal structural phase transition in network glasses**, Solid State Commun. **47**, 199–202 (1983).

[30] T. Wagner and S. Kasap, **Glass transformation, heat capacity and structure of As_xSe_{1-x} glasses studied by modulated temperature differential scanning calorimetry experiments**, Philos. Mag. B **74**, 667–680 (1996).

[31] D. J. Jacobs, A. J. Rader, L. Kuhn, M. Lei, and M. F. Thorpe, **Protein flexibility predictions using graph theory**, Proteins **44**, 150–165 (2001).

[32] R. Monasson, R. Zecchina, S. Kirkpatrick, B. Selman, and L. Troyansky, **Determining computational complexity from characteristic 'phase transitions'**, Nature **400**, 133–137 (1999).

[33] M. F. Thorpe and P. M. Duxbury, editors, *Rigidity theory and applications*, Plenum Press/Kluwer Academic, New York, 1st edition, 1999.

[34] P. Boolchand and W. J. Bresser, **The structural origin of broken chemical order in $GeSe_2$**, Philos. Mag. B **80**, 1757–1772 (2000).

[35] M. Micoulaut and J. C. Phillips, **Rings and rigidity transitions in network glasses**, Phys. Rev. B **67**, 104204 (2003).

[36] D. S. Franzblau and J. Tersoff, **Elastic properties of a network model of glasses**, Phys. Rev. Lett. **68**, 2172–2175 (1992).

[37] B. Wunderlich, Y. M. Jin, and A. Boller, **Mathematical-description of differential scanning calorimetry based on periodic temperature modulation**, Thermochim. Acta **238**, 277–293 (1994).

[38] P. Boolchand, D. G. Georgiev, and M. Micoulaut, **Nature of glass transition in chalcogenides**, J. Optoelectron. Adv. M. **4**, 823–836 (2002).

[39] P. Boolchand, P. Chen, M. Jin, B. Goodman, and W. J. Bresser, **^{129}I and ^{119}Sn Mossbauer spectroscopy, reversibility window and nanoscale phase separation in binary Ge_xSe_{1-x} glasses**, Physica B **389**, 18–28 (2007).

[40] D. G. Georgiev, M. Mitkova, P. Boolchand, G. Brunklaus, H. Eckert, and M. Micoulaut, **Molecular structure, glass transition temperature variation, agglomeration theory, and network connectivity of binary P-Se glasses**, Phys. Rev. B **6413**, 134204 (2001).

[41] S. Chakravarty, D. G. Georgiev, P. Boolchand, and M. Micoulaut, **Ageing, fragility and the reversibility window in bulk alloy glasses**, J. Phys.: Condens. Mat. **17**, L1–L7 (2005).

[42] M. S. Iovu, S. D. Shutov, P. Boolchand, D. G. Georgiev, and E. P. Colomeico, **The relaxation of photodarkening in Sn-doped amorphous As_2Se_3 films**, J. Optoelectron. Adv. M. **5**, 389–395 (2003).

[43] Y. Wang, M. Mitkova, D. G. Georgiev, S. Mamedov, and P. Boolchand, **Macroscopic phase separation of Se-rich (x < 1/3) ternary $Ag_y(Ge_xSe_{1-x})_{(1-y)}$ glasses**, J. Phys.: Condens. Mat. **15**, S1573–S1584 (2003).

[44] D. G. Georgiev, P. Boolchand, H. Eckert, M. Micoulaut, and K. Jackson, **The self-organized phase of bulk P_xSe_{1-x} glasses**, Europhys. Lett. **62**, 49–55 (2003).

[45] Y. Wang, P. Boolchand, and M. Micoulaut, **Glass structure, rigidity transitions and the intermediate phase in the Ge-As-Se ternary**, Europhys. Lett. **52**, 633–639 (2000).

[46] D. Selvanathan, W. J. Bresser, P. Boolchand, and B. Goodman, **Thermally reversing window and stiffness transitions in chalcogenide glasses**, Solid State Commun. **111**, 619–624 (1999).

[47] F. Wang, S. Mamedov, P. Boolchand, B. Goodman, and M. Chandrasekhar, **Pressure Raman effects and internal stress in network glasses**, Phys. Rev. B **71**, 174201 (2005).

[48] P. Boolchand, X. Feng, and W. J. Bresser, **Rigidity transitions in binary Ge-Se glasses and the intermediate phase**, J. Non-Cryst. Solids **293**, 348–356 (2001).

[49] H. He and M. F. Thorpe, **Elastic properties of glasses**, Phys. Rev. Lett. **54**, 2107–2110 (1985).

[50] L. Ross and M. Bourgon, **Germanium-selenium phase diagram**, Can. J. Chemistry **47**, 2555–2559 (1969).

[51] P. Quenez, R. Ceolin, and P. Khodadad, **Complementary study of Ge - Se diagram and a new interpretation**, Bulletin de la Societe Chimique de France **1**, 117– (1972).

[52] M. M. Hafiz, F. H. Hammad, and N. A. Elkabany, **Short-range and medium-range order in Se-Ge glassy systems 1. Effect of composition**, Physica B **183**, 392–398 (1993).

[53] P. Tronc, A. Brenac, and C. Sebenne, **Optical-absorption edge and Raman-scattering in Ge_xSe_{1-x} glasses**, Phys. Rev. B **8**, 5947–5956 (1973).

[54] G. Dittmar and H. Schafer, **Crystal structure of low-temperature GeS_2**, Acta Crystallogr. B **32**, 1188–1192 (1976).

[55] G. Dittmar and H. Schafer, **Crystal structure of HT-GeS_2**, Acta Crystallogr. B **31**, 2060–2064 (1975).

[56] F. P. Bundy and J. S. Kasper, **A new dense form of solid germanium**, Science **139**, 340–341 (1963).

[57] P. Cherin and P. Unger, **Crystal structure of trigonal selenium**, Inorg. Chem. **6**, 1589–1591 (1967).

[58] P. Cherin and P. Unger, **Refinement of crystal-structure of alpha-monoclinic Se**, Acta Crystallogr. B **B 28**, 313–317 (1972).

[59] R. E. Marsh, L. Pauling, and J. D. Mccullough, **The crystal structure of beta-selenium**, Acta Crystallogr. **6**, 71–75 (1953).

[60] S. C. Moss, *Amorphous and liquid semiconductors*, Taylor and Francis, London, 1974.

[61] M. D. Rechtin and B. L. Averbach, **A Monte-Carlo model of sputtered vitreous selenium thin films**, Solid State Commun. **13**, 491–494 (1973).

[62] M. D. Rechtin, A. L. Renninge, and B. L. Averbach, **Monte-Carlo models of amorphous materials**, J. Non-Cryst. Solids **15**, 74–82 (1974).

[63] M. D. Rechtin, **Monte-Carlo models of molecular morphology of amorphous Se-As thin films**, Bull. Am. Phys. Soc. **19**, 316–316 (1974).

[64] A. I. Andrievskii, I. D. Nabitovich, and P. I. Kripiakevich, **Selenium structure in thin layers**, Doklady Akademii Nauk SSSR **124**, 321– (1959).

[65] G. Dittmar and H. Schafer, **Crystal structure of germanium diselenide**, Acta Crystallogr. B **32**, 2726–2728 (1976).

[66] S. Susman, K. J. Volin, D. G. Montague, and D. L. Price, **The structure of vitreous and liquid $GeSe_2$ - a neutron-diffraction study**, J. Non-Cryst. Solids **125**, 168–180 (1990).

[67] R. J. Nemanich, S. A. Solin, and G. Lucovsky, **First evidence for vibrational excitations of large atomic clusters in amorphous semiconductors**, Solid State Commun. **21**, 273–276 (1977).

[68] P. M. Bridenbaugh, G. P. Espinosa, J. E. Griffiths, J. C. Phillips, and J. P. Remeika, **Microscopic origin of the companion A_1 Raman line in glassy $Ge(S,Se)_2$**, Phys. Rev. B **20**, 4140–4144 (1979).

[69] K. Murase, T. Fukunaga, K. Yakushiji, T. Yoshimi, and I. Yunoki, **Investigation of stability of (Ge,Sn)-(S, or Se)$_{4/2}$ cluster by vibrational spectra**, J. Non-Cryst. Solids **59**, 883–886 (1983).

[70] S. Sugai, **Stochastic random network model in Ge and Si chalcogenide glasses**, Phys. Rev. B **35**, 1345–1361 (1987).

[71] R. J. Nemanich, F. L. Galeener, J. C. Mikkelsen, G. A. Connell, G. N. Etherington, A. C. Wright, and R. N. Sinclair, **Configurations of a chemically ordered continuous random network to describe the structure of $GeSe_2$ glass**, Physica B **117**, 959–961 (1983).

[72] W. J. Bresser, P. Boolchand, P. Suranyi, and J. P. Deneufville, **Direct evidence for intrinsically broken chemical ordering in melt-quenched glasses**, Phys. Rev. Lett. **46**, 1689–1692 (1981).

[73] P. Boolchand, W. J. Bresser, and M. Tenhover, **Direct evidence for intrinsically broken 8-N coordination rule in melt-quenched glasses by a novel method**, Phys. Rev. B **25**, 2971–2974 (1982).

[74] P. Vashishta, R. K. Kalia, and I. Ebbsjo, **Structural correlations and phonon density of states in $GeSe_2$ - A molecular-dynamics study of molten and amorphous states**, Phys. Rev. B **39**, 6034–6047 (1989).

[75] M. Cobb and D. A. Drabold, **Ab initio molecular-dynamics study of liquid $GeSe_2$**, Phys. Rev. B **56**, 3054–3065 (1997).

[76] M. Cobb, D. A. Drabold, and R. L. Cappelletti, **Ab initio molecular-dynamics study of the structural, vibrational, and electronic properties of glassy $GeSe_2$**, Phys. Rev. B **54**, 12162–12171 (1996).

[77] C. Massobrio, A. Pasquarello, and R. Car, **Microscopic structure of liquid $GeSe_2$: The problem of concentration fluctuations over intermediate range distances**, Phys. Rev. Lett. **80**, 2342–2345 (1998).

[78] I. T. Penfold and P. S. Salmon, **A neutron diffraction study on the structure of molten $GeSe_2$ - the Ge coordination environment**, J. Phys.: Condens. Mat. **2**, SA233–SA237 (1990).

[79] I. Petri, P. S. Salmon, and H. E. Fischer, **Defects in a disordered world: the structure of glassy $GeSe_2$**, Phys. Rev. Lett. **84**, 2413–2416 (2000).

[80] I. T. Penfold and P. S. Salmon, **Structure of covalently bonded glass-forming melts - a full partial-structure-factor analysis of liquid $GeSe_2$**, Phys. Rev. Lett. **67**, 97–100 (1991).

[81] W. J. Bresser, P. Boolchand, P. Suranyi, and J. G. Hernandez, **Molecular-phase separation and cluster size in $GeSe_2$ glass**, Hyperfine Interact. **27**, 389–392 (1986).

[82] J. E. Griffiths, J. C. Phillips, G. P. Espinosa, J. P. Remeika, and P. M. Bridenbaugh, **Assignment of the companion A_1^c line in $Ge_x(S,Se)_{1-x}$ glasses**, Phys. Status. Solidi. B **122**, K11–K15 (1984).

[83] D. L. Price, S. Susman, K. J. Volin, and R. J. Dejus, **Intermediate-range order in binary and ternary glasses**, Physica B **156**, 189–191 (1989).

[84] P. Armand, A. Ibanez, Q. Ma, D. Raoux, and E. Philippot, **Structural characterization of germanium selenide glasses by differential anomalous X-ray scattering**, J. Non-Cryst. Solids **167**, 37–49 (1994).

[85] J. C. Malaurent and J. Dixmier, **X-ray diffraction and local order modeling of Ge_xSe_{1-x} amorphous alloys**, J. Non-Cryst. Solids **35**, 1227–1232 (1980).

[86] F. Betts, A. Bienenstock, D. T. Keating, and J. P. de Neufville, **Neutron and X-ray diffraction radial distribution studies of amorphous $Ge_{0.17}Te_{0.83}$**, J. Non-Cryst. Solids **7**, 417–432 (1972).

[87] S. R. Elliott, **Origin of the first sharp diffraction peak in the structure factor of covalent glasses**, Phys. Rev. Lett. **67**, 711–714 (1991).

[88] R. W. Johnson, D. L. Price, S. Susman, M. Arai, T. I. Morrison, and G. K. Shenoy, **The structure of silicon selenium glasses 1. short-range order**, J. Non-Cryst. Solids **83**, 251–271 (1986).

[89] D. L. Price, M. Misawa, S. Susman, T. I. Morrison, G. K. Shenoy, and M. Grimsditch, **The structure of phosphorus-selenium glasses 1. concentration-dependence of the short-range and intermediate-range order**, J. Non-Cryst. Solids **66**, 443–465 (1984).

[90] J. K. Christie, S. N. Taraskin, and S. R. Elliott, **Structural characteristics of positionally disordered lattices: Relation to the first sharp diffraction peak in glasses**, Phys. Rev. B **70**, 134207 (2004).

[91] J. K. Christie, S. N. Thraskin, and S. R. Elliott, **Positional disorder in lattices: a model for the structural order responsible for the first sharp diffraction peak in glasses**, J. Phys.: Condens. Mat. **16**, S5109–S5120 (2004).

[92] P. Vashishta, R. K. Kalia, G. A. Antonio, and I. Ebbsjo, **Atomic correlations and intermediate range order in molten and amorphous $GeSe_2$**, Phys. Rev. Lett. **62**, 1651–1654 (1989).

[93] B. E. Warren, *X-ray diffraction*, Dover, New York, 1990.

[94] C. L. Farrow, P. Juhas, J. W. Liu, D. Bryndin, E. S. Božin, J. Bloch, T. Proffen, and S. J. L. Billinge, **PDFfit2 and PDFgui: Computer programs for studying nanostructure in crystals**, J. Phys: Condens. Matter **19**, 335219 (2007).

[95] R. L. Mcgreevy, M. A. Howe, D. A. Keen, and K. N. Clausen, **Reverse Monte-Carlo (RMC) simulation - modeling structural disorder in crystals, glasses and liquids from diffraction data**, Inst. Phys. Conf. Ser. **107**, 165–184 (1990).

[96] V. Petkov and S. J. L. Billinge, **Local structure of random $In_xGa_{1-x}As$ alloys by full-profile fitting of atomic pair distribution functions**, Physica B **305**, 83 (2001).

[97] S. J. L. Billinge, R. G. DiFrancesco, G. H. Kwei, J. J. Neumeier, and J. D. Thompson, **Direct observation of lattice polaron formation in the local structure of $La_{1-x}Ca_xMnO_3$**, Phys. Rev. Lett. **77**, 715–718 (1996).

[98] I.-K. Jeong, T. Proffen, F. Mohiuddin-Jacobs, and S. J. L. Billinge, **Measuring correlated atomic motion using X-ray diffraction**, J. Phys. Chem. A **103**, 921–924 (1999).

[99] Y. Waseda, *The structure of non-crystalline materials*, McGraw-Hill, New York, 1980.

[100] D. Louca and T. Egami, **Local lattice distortions in $La_{1-x}Sr_xMnO_3$ studied by pulsed neutron scattering.**, Phys. Rev. B **59**, 6193–6204 (1999).

[101] A. C. Larson and R. B. Von Dreele, **General Structure Analysis System**, Report No. LAUR-86-748, Los Alamos National Laboratory, Los Alamos, NM 87545, 2000.

[102] http://home.wxs.nl/rietv025.

[103] C. Farrow, **PDFFITING; an updated C++ implementation of the PDFFIT program**, unpublished, 2006.

[104] D. E. Sayers and E. A. Stern, **New technique for investigating noncrystalline structures: Fourier analysis of the extended X-ray-absorption fine structure**, Phys. Rev. Lett. **27**, 1204–1207 (1971).

[105] P. J. Chupas, X. Qiu, J. C. Hanson, P. L. Lee, C. P. Grey, and S. J. L. Billinge, **Rapid acquisition pair distribution function analysis (RA-PDF)**, J. Appl. Crystallogr. **36**, 1342–1347 (2003).

[106] S. D. Shastri, K. Fezzaa, A. Mashayekhhi, W.-K. Lee, P. B. Fernandez, and P. L. Lee, **Cryogenically cooled bent double-Laue monochromator for high-energy undulator X-rays (50-200 KeV)**, J. Synchrotron Radiat. **9**, 317–322 (2002).

[107] A. P. Hammersley, **FIT2D v9.129 reference manual v3.1**, ESRF Internal Report ESRF98HA01T, 1998.

[108] X. Qiu, J. W. Thompson, and S. J. L. Billinge, **PDFgetX2: a GUI driven program to obtain the pair distribution function from X-ray powder diffraction data**, J. Appl. Crystallogr. **37**, 678 (2004).

[109] M. Newville, **IFEFFIT: interactive XAFS analysis and FEFF fitting**, J. Synchrotron Radiat. **8**, 322–324 (2001).

[110] B. Ravel and M. Newville, **ATHENA, ARTEMIS, HEPHAESTUS: Data analysis for X-ray absorption spectroscopy using IFEFFIT**, J. Synchrotron Radiat. **12**, 537–541 (2005).

[111] M. Newville, P. Livins, Y. Yacoby, J. J. Rehr, and E. A. Stern, **Near-edge X-ray-absorption fine-structure of Pb - a comparison of theory and experiment**, Phys. Rev. B **47**, 14126–14131 (1993).

[112] V. Petkov, I. K. Jeong, J. S. Chung, M. F. Thorpe, S. Kycia, and S. J. L. Billinge, **High real-space resolution measurement of the local structure of $Ga_{1-x}In_xAs$ using X-ray diffraction**, Phys. Rev. Lett. **83**, 4089–4092 (1999).

[113] I.-K. Jeong, F. Mohiuddin-Jacobs, V. Petkov, S. J. L. Billinge, and S. Kycia, **Local structure study of $In_xGa_{1-x}As$ semiconductor alloys using high energy synchrotron X-ray diffraction**, Phys. Rev. B **63**, 205202 (2001).

[114] G. Lucovsky, F. L. Galeener, R. H. Geils, and R. C. Keezer, *The structure of non-crystalline materials*, Taylor and Francis, London, 1st edition, 1977.

[115] H. A. Davies and C. N. Wagner, **X-ray diffraction study of tensile deformation in a bulk polycrystalline alloys**, J. Mater. Sci. **7**, 105– (1972).

[116] S. C. Rowland, Bienenst.A, and Narasimh.S, **Radial distribution studies of glassy Ge_xS_{1-x} alloys**, J. Appl. Phys. **43**, 2741– (1972).

[117] G. Lucovsky, F. L. Galeener, R. C. Keezer, R. H. Geils, and H. A. Six, **Structural interpretation of infrared and Raman-spectra of glasses in alloy system $Ge_{1-x}S_x$**, Phys. Rev. B **10**, 5134–5146 (1974).

[118] I. T. Penfold and P. S. Salmon, **Structure of covalently bonded glass-forming melts: a full partial-structure-factor analysis of liquid $GeSe_2$**, Phys. Rev. B **67**, 97–100 (1991).

[119] E. Bychkov, C. J. Benmore, and D. L. Price, **Compositional changes of the first sharp diffraction peak in binary selenide glasses**, Phys. Rev. B **72**, 172107 (2005).

[120] M. Jergel and P. Mrafko, **The temperature-dependence of the pre-peak in the diffraction pattern of the amorphous $Ti_{61}Cu_{16}Ni_{23}$ and $Ti_{62.5}Cu_{12}Ni_{23}Si_{2.5}$ alloys**, Phys. Status. Solidi. A **83**, 113–121 (1984).

[121] T. Uchino, J. D. Harrop, S. N. Taraskin, and S. R. Elliott, **Real and reciprocal space structural correlations contributing to the first sharp diffraction peak in silica glass**, Phys. Rev. B **71**, 014202 (2005).

[122] D. A. Drabold, J. Li, and D. Tafen, **Simulations of arsenic selenide glasses**, J. Phys.: Condens. Mat. **15**, S1529–S1536 (2003).

[123] P. Biswas, D. Tafen, and D. A. Drabold, **Experimentally constrained molecular relaxation: The case of glassy $GeSe_2$**, Phys. Rev. B **71**, 054204 (2005).

[124] D. Tafen, D. A. Drabold, and M. Mitkova, **Silver transport in Ge_xSe_{1-x} : Ag materials: Ab initio simulation of a solid electrolyte**, Phys. Rev. B **72**, 054206 (2005).

[125] A. A. Demkov, J. Ortega, O. F. Sankey, and M. P. Grumbach, **Electronic-structure approach for complex silicas**, Phys. Rev. B **52**, 1618–1630 (1995).

[126] O. F. Sankey, D. A. Drabold, and A. Gibson, **Projected random vectors and the recursion method in the electronic-structure problem**, Phys. Rev. B **50**, 1376–1381 (1994).

[127] X. D. Zhang and D. A. Drabold, **Structural and electronic properties of glassy $GeSe_2$ surfaces**, Phys. Rev. B **62**, 15695–15701 (2000).

[128] S. S. Yun, H. Li, R. L. Cappelletti, R. N. Enzweiler, and P. Boolchand, **Onset of rigidity in $Se_{1-x}Ge_x$ glasses - ultrasonic elastic-moduli**, Phys. Rev. B **39**, 8702–8706 (1989).

[129] J. Y. Duquesne and G. Bellessa, **Internal-friction peak in amorphous selenium at low-temperature**, J. Phys. C Solid State **13**, L215–L219 (1980).

[130] J. Y. Duquesne and G. Bellessa, **Ultrasonic properties of Se - Ge glasses, between 1-k and 100-k**, J. Phys.-Paris **46**, 445–448 (1985).

[131] J. Y. Duquesne and G. Bellessa, **Ultrasonic study of tunnelling defects in amorphous Se, Ge and Se-Ge compounds**, Philos. Mag. B **52**, 821–842 (1985).

[132] J. Y. Duquesne and G. Bellessa, **Ultrasonic study of tunneling defects in selenium-germanium glasses**, J. Phys.-Paris **46**, 449–452 (1985).

[133] R. Ota, T. Yamate, N. Soga, and M. Kunugi, **Elastic properties of Ge-Se glass under pressure**, J. Non-Cryst. Solids **29**, 67–76 (1978).

[134] A. N. Sreeram, A. K. Varshneya, and D. R. Swiler, **Microhardness and indentation toughness versus average coordination-number in isostructural chalcogenide glass systems**, J. Non-Cryst. Solids **130**, 225–235 (1991).

[135] K. Murase and T. Fukunaga, **Pressure-induced structural-change of clusters in chalcogenide glasses**, AIP Conf. Proc. **120**, 449–456 (1984).

[136] M. J. Harris, M. T. Dove, and J. M. Parker, **Floppy modes and the boson peak in crystalline and amorphous silicates: an inelastic neutron scattering study**, Mineralogical Magazine **64**, 435–440 (2000).